Study of Excited-State and Carrier Dynamics on Organic Thin Films of Weak Charge-Transfer Complexes and TIPS-Pentacene Using Electron Spin Probes

（電子スピンをプローブとして用いた弱い有機電荷移動錯体薄膜とTIPS－ペンタセン薄膜の励起状態とキャリアダイナミクスの研究）

理学研究科
物質分子系専攻

March 2021

Ken Kato

（加藤　賢）

Abstract

An unpaired electron spin in organic semiconductors can be used to probe the inside of the device. Using the unpaired spin as the probe (spin-probe) to measure the change in physical properties caused by an applied magnetic field or ESR transition is a useful approach to evaluate the excited state and carrier dynamics in a non-destructive and selective manner. In this dissertation, a methodology to evaluate the mechanism of photocurrent generation in organic thin films has been established. Two weak charge transfer complexes, pyrene/dimethylpyromellitdiimide (Py/DMPI) and pyrene/pyromellitic-dianhydride (Py/PMDA), were chosen as target compounds to establish this methodology. The excited-state and carrier dynamics related to photocurrent generation were clarified using a combination of several measurements using the spin probe. The photocurrent and the magnetoconductance (MC) were measured in the vacuum vapour deposition (VVD) films of Py/DMPI and Py/PMDA. The MC behaviour was reasonably explained by assuming two types of collision mechanisms: Doublet–doublet (DD) pair and triplet–doublet (TD) pair mechanisms, which occur between the geminate electron–hole pair and between the trapped triplet-species (exciton or charge-separated state) and carrier. Weakly interacting spin pairs (DD or TD pairs) are expected to be generated during their collisions. The carrier generation process via their weakly interacting spin pairs was clarified by measuring the MC of the photocurrent and the temperature dependence of the photocurrent, time-resolved ESR, and electrically detected magnetic resonance (EDMR) with the aid of quantum mechanical simulations of the MC. It has been demonstrated that the combination of spin-probe measurements (MC effect, TRESR, and EDMR) and quantum mechanical simulations is a powerful approach to clarify the excited-state and carrier dynamics leading to photocurrent generation. The methodology (a combination of the temperature dependence of the photocurrent, EDMR measurement, and quantum mechanical simulations of the excited state dynamics) has been applied to the VVD film of TIPS-pentacene. The photocurrent generation mechanism and excited state dynamics were clarified using a similar approach established during the study of the CT complex described above.

Table of Contents

List of Abbreviations

CCD	charged coupled device
CH_2Cl_2	dichloromethane
CT	charge transfer
CV	cyclic voltammogram
D	D value of fine structure tensor
DD	doublet-doublet
DFT	density functional theory
DMPI	dimethylpyromellitdiimide
EDMR	electrically detected magnetic resonance
E	energy or E value of fine structure tensor
e–h	electron-hole
ESR	electron spin resonance
Ex	exciton
ex–c	exciton-carrier
Fc	ferrocene
Fc^+	ferrocenium
FET	field-effect transistors
h	Plank constant
$\hbar$	Dirac constant; $\hbar = h/(2\pi)$
$\mathcal{H}$	Hamiltonian
HFC	hyperfine coupling
HOMO	highest occupied molecular orbital
ISC	intersystem crossing
J	magnetic exchange parameter
k	rate constant
k_B	Boltzmann constant
K	Kelvin
$\boldsymbol{L}$	Liouvillian

LC	level crossing
LUMO	lowest occupied molecular orbital
MC	magneto-conductance
MFE	magnetic field effect
MEL	magneto-electroluminescence
MO	molecular orbital
ODMR	optically detected magnetic resonance
OFET	organic FET
OLED	organic light emitting diode
OMAR	organic magnetoresistance
OSC	organic solar cell
Py	pyrene
PMDA	pyromellitic dianhydride
RB3LYP	restricted Becke 3-parameter Lee Yang Parr
RYDMR	reaction yield detected magnetic resonance
SF	singlet fission
SOMO	singly occupied molecular orbital
TD	triplet-doublet
TIPS-Pn	6,13-bis(triisopropylsilylethynyl)pentacene
TF	triplet fusion
TRESR	time resolved ESR
TT	triplet- triplet
UV	ultraviolet
UB3LYP	unrestricted Becke 3-parameter Lee Yang Parr
VVD	vacuum vapor deposition
ε	dielectric constant
λmax	wavelength of maximum electronic absorption
μ_{B}	Bohr magneton
Λ	projection operator
$\boldsymbol{\rho}$	density matrix

List of Figures, Tables and Schemes

Chapter 1

Introduction

1-1. Spin in Organic Semiconductor

Devices based on organic semiconductors have been investigated due to their advantages such as low weight, flexibility, and environmental friendliness. To date, a variety of studies have been carried out to further develop these devices. Recently, organic semiconductors can be formulated into ink-jet processed using solution-based printing processes. This allows for large-area and high-throughput of organic device, enabling not only a reduction in cost but also the fabrication to flexible circuitry the use of plastic substrates.[1, 2] A lot of effort has been made to synthesize compounds with higher mobility in order to control the band gap (HOMO and LUMO levels) and develop cheaper and large-scale synthetic methods.[3] The properties of organic semiconductor devices can be evaluated not only using current measurements of the input voltage, but also various techniques, such as spectroscopy (UV-visible, infrared, and X-ray diffraction, etc.), surface observations using electron microscopy, and theoretical calculations.[4]

Mobile electrons and holes, which are the charge carriers in organic devices, have a spin of $S = 1/2$. This property can be used to probe the inside and working mechanism of organic semiconductors. Field-effect transistors (FETs) have been actively studied for application in organic semiconductors. In organic FETs (OFETs), the spins of the charge carriers injected using an electrical field can be successfully observed using the conventional ESR technique.[5] In the OFET device, the transport mechanism of electrical field injected carriers, orientation of the molecules, and spin density distribution of the carriers can be investigated using ESR. Since the electron spins injected in a single crystal and polymer film have long relaxation times[6] and a long spin diffusion length,[7] they have been studied for application in spintronics and quantum information technology.[8]

Organic solar cells (OSCs) and organic light-emitting diodes (OLEDs) are also being actively studied in the field of organic semiconductors. OSCs and OLEDs have the ability to convert between light energy and electric energy and therefore, been the focus of a lot of research attention. A schematic diagram of photocurrent generation in an organic semiconductor is shown in **Fig. 1-1**. Excited states (molecular exciton or charge-transfer excited state) are generated upon photoexcitation and mobile electron and hole carriers are then generated via an weakly interacting electron-hole pair (e–h pair) intermediate. In OLEDs, reverse processes occur in which the mobile electrons and holes collide with each other and form an e–h pair. ESR studies on OSCs and OLEDs have revealed the degradation mechanism in their devices by observing the carrier accumulation.[9–11] Time-resolved ESR (TRESR) has been used to study the excited triplet states of phosphorescent OLED materials and the charge-separated states in the OSC of bulk hetero-junctions.[12–14] Compared to the transient absorption, the TRESR method can only measure at the time range longer than the nanosecond order, but it can selectively measure of paramagnetic species and provide information about spin interactions and spin dynamics.

A weakly interacting e–h pair is a doublet–doublet pair (DD pair) because each of the electron and hole has doublet spin states; it is also called a radical pair or ion pair in photochemistry and a bipolaron in condensed matter physics. The weakly interacting e–h pair is characterized as a singlet state or triplet state.[15] The vector model for singlet and triplet states is shown in **Fig. 1-2**. When a magnetic field is applied to the radical pair, each radical spin in the e–h pair undergoes a Larmor precession at the angular frequency $\omega = g\mu_B B$, where g, μ_B, and B are the g-value, Bohr magneton, and applied external magnetic field, respectively. When an external magnetic field is applied to the electron spins, the energy changes ($E = g\mu_B \boldsymbol{S}\cdot\boldsymbol{B}$) due to the Zeeman effect. When the angular frequency in the Larmor precession differs between two spins in the e–h pair, the singlet and triplet states are converted into each other under the magnetic field (Δg mechanism).[16, 17]

This phenomenon is known as magnetic field-dependent intersystem crossing (denoted by B-dependent ISC in this thesis), which is sometimes called radical pair ISC.[18] The B-dependent ISC between the S and T_0 states is also known as S-T_0 mixing.[19] This is also caused by Fermi contact interaction with the nucleus hyperfine coupling mechanism (HFC mechanism),[20] as shown **Fig. 1-3**. The B-dependent ISC due to the HFC mechanism only occurs under low magnetic fields ($B \sim$ HFC) because the hyperfine coupling of organic materials is very small. When an exchange interaction (J) exists between the unpaired electron in the e–h pair, the singlet e–h pair (^{1}(e–h)) and triplet e–h pair (^{3}(e–h)) have an energy difference of $\Delta E = 2J$. When the magnitude of J matches the Zeeman splitting induced by the external magnetic field, the energy levels of the spin states (S and T_+ or T_-) in the e–h pair cross each other and then, the B-dependent ISC due to S-$T_\pm$ mixing occurs, as shown **Fig. 1-4**. This process is known as the level-crossing mechanism (LC mechanism). [21, 22]

Based on the spin selection rule, the singlet e–h [^{1}(e–h)] and triplet e–h [^{3}(e–h)] pairs have different kinetic (reaction) rates. Therefore, the subsequent generation rate of the transient product changes by the B-dependent ISC between the ^{1}(e–h) pair and ^{3}(e–h) pair. The changes in the physical quantity induced by the external magnetic field are generally known as the magnetic field effect (MFE). The study of MFE on kinetic processes involving intermediate paramagnetic radical pairs has been established for both solid and liquid phases over many years.[15] Several studies on the MFE in the liquid phase have been reported to change the yields of intermediates or products in photochemical reactions.[22] In the solid phase, the photoconductivity or delayed fluorescence sometimes varies due to the MFE in organic semiconductors. Recently, in the field of biochemistry, it has been reported that migratory birds have a compass sensing the earth's magnetic field based on an MFE in their eyes.[23] In organic semiconductor devices, magneto-electroluminescence (MEL) and magneto-conductance (MC) exceeding 1000% under ~300 mT at room temperature was demonstrated under the device operating conditions. [24] [25] This tremendously large MFE is named organic magnetoresistance (OMAR) in OLEDs. The OMAR is observed even at very low magnetic fields, such as the earth's magnetic field. It has been reported that an OLED device using OMAR can detect local geomagnetic fields with magnitudes of ~50 μT.[26] Today, the MFE of the organic semiconductors has become a renewed topic of interest as a result of these demonstrations.

The weakly interacting paramagnetic species responsible for the MFE in organic semiconductors are not only e–h pairs, but also exciton–carrier (ex–c) pairs consisting of an electron or hole and triplet state of the excitons in the crystal. This pair is also known as a triplet–doublet (TD) pair or trion.[27] There may also be a triplet–triplet (TT) pair consisting of two triplet species. Based on the TD pair mechanism, studies on ex–c dynamics have also been conducted, including charge recombination at the interface between the donor and acceptor layers of solar cells and carrier trapping/detrapping processes by triplet excitons in both layers.[28]

These weakly interacting paramagnetic intermediate pairs are difficult to detect using conventional ESR because of their low concentration and short lifetime. Advanced ESR spectroscopy described later makes the detection of low concentrations of short-lived intermediate pairs possible. The spin state of the pair species can be changed by not only an external magnetic field, but also a resonant microwave transition between the spin sub-levels of the pair. In this case, microwave absorption affects the reaction yield of the pair species. Thus, the photocurrent, emission, and chemical product are influenced by the microwave resonant absorption, that is, the ESR transition. In particular, the method used to detect changes in emission due to ESR transitions is optically detected magnetic resonance (ODMR), [29, 30] while the method used to monitor the current change due to ESR transitions is electrically detected magnetic resonance (EDMR). [31] These two advanced ESR techniques have very high sensitivity because microwave absorption (low energy) is converted into luminescence or electric current (high energy). In addition, in the conventional ESR method used to monitor microwave absorption and emission, all types of electron spins in the system contribute to the obtained spectrum. In contrast, EDMR and ODMR do not detect isolated organic radicals or spins trapped by defects, which do not affect the current and emission via ESR transitions between their spin sub-levels. A number of ODMR and EDMR studies of weakly interacting spin pairs in organic solids have been reported by Frankevich *et al.* since the 1970s.[32] They called the ODMR and EDMR detection attributed to the change in the reaction yield induced by ESR transition, reaction yield detected magnetic resonance (RYDMR). Frankevich *et al.* successfully detected not only the e–h pair, but also the ex–c pair and TT pair in aromatic hydrocarbons and crystals of weak charge-transfer (CT) complexes using the RYDMR method. [33–35]

Recently, EDMR and ODMR studies on organic thin-film devices under various operating conditions have been carried out to elucidate the mechanism of OLEDs and OSCs in order to develop more efficient devices.[36] In OLEDs, the characteristics of the photogenerated e–h pairs have been studied using EDMR and ODMR under photoexcitation.[37, 38] The bias dependence of the EDMR and ODMR signals suggested that the e–h pair was dissociated under an applied bias using an electric field.[39–41] It has been reported that the intensity of the EDMR for OSCs and OLEDs varies under an ambient atmospheric and the degradation mechanism for their devices due to atmospheric oxygen was elucidated.[41, 42] However, the influence of atmospheric conditions and temperature on the device performance or the semiconductor material used in their devices are still unclear.

In this thesis, 6,13-bis(triisopropylsilylethynyl) pentacene (TIPS-Pn) will be treated as one of the target materials to clarify the excited state and carrier dynamics. It is well known that pentacene derivatives are rare compounds to show "singlet fission" (SF) phenomenon. SF is a process in which a pair of singlet excited states and the singlet ground state splits into two triplet excited states. This process has been established with a theory involving electron spin interactions by Merrifield.[43] Triplet fusion (TF) is the inverse process of SF, in which the excited and ground singlet states are generated from the collision of two triplet excited states.[44] The delayed fluorescence from the excited singlet state, which is generated from the TF, changes the emission intensity due to the MFE of the TT pair.[45]

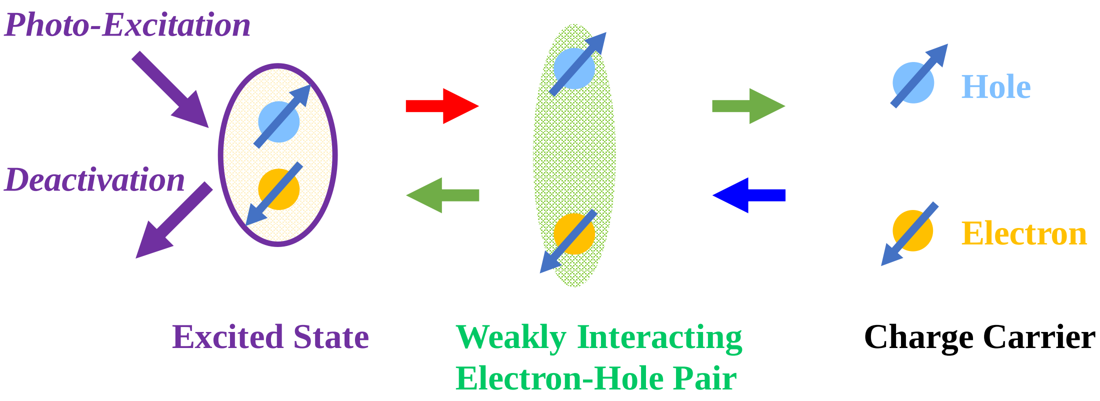

Fig. 1-1. Schematic diagram of the photocurrent generation mechanism.

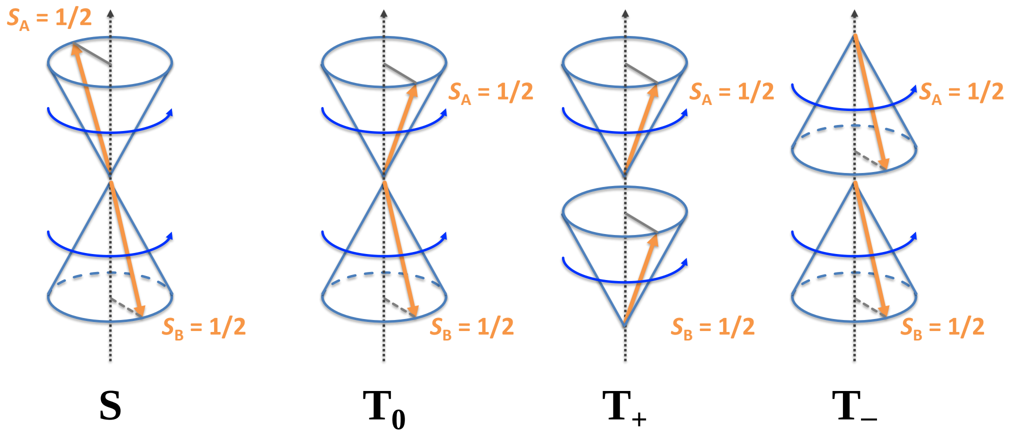

Fig. 1-2. Vector model of the singlet and triplet states.

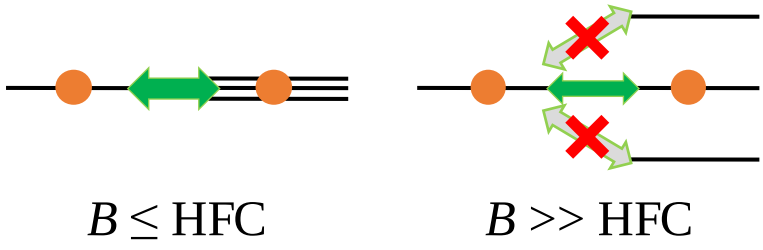

Fig. 1-3. *B*-dependent ISC mechanism due to hyperfine coupling mechanism.

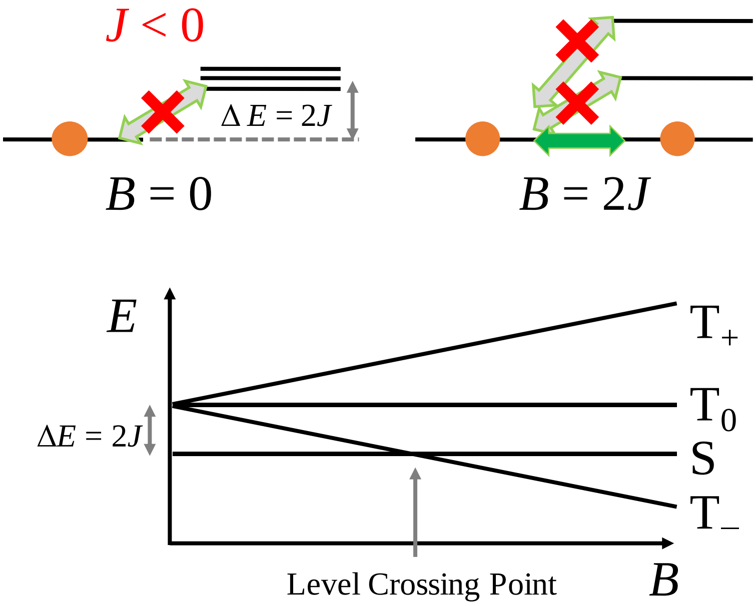

Fig. 1-4. *B*-dependent ISC mechanism due to level crossing mechanism.

1-2. Scope and Outline of This Thesis

The purpose of this study is to establish a protocol to evaluate the mechanism of photocurrent generation in organic thin films in detail. The molecular structures used in this study are shown in **Fig. 1-5**. To date, the MFE has been explained using the $\varDelta g$, HFC, and LC mechanisms of the e–h pair. The photocurrent generation process involves not only e–h pairs, but also ex–c pairs. Although the fine structure interaction due to the magnetic dipolar-dipolar interactions between the unpaired electrons are averaged to zero by the molecular motion in solution, the interaction remains and contributes to the MFE in the solid phase. Nowadays, numerical calculations of the MFE, which take many interactions into account, can be performed by the improved computer performance. Hence, a simulation method for the MFE can be developed to numerically solve the Liouville equation that incorporates all possible interactions in the DD-pair and TD-pair mechanisms.

In this work, a simulation method is developed. Weak CT complexes whose properties are well known were chosen. These CT complexes allowed us to obtain physical parameters to simulate the MFE on the photocurrent and to make it easy to establish a method to evaluate several mechanisms. 1:1 complexes of pyrene (Py) and dimethylpyromellitdiimide (DMPI),[46] and Py and pyromellitic dianhydride (PMDA)[47] were used in our experiments. In the simulation, all interactions (Zeeman, hyperfine coupling, fine structure, and exchange interaction) which were used to determine the Δg, HFC, and LC mechanisms were considered. The e–h pair character clarified by EDMR measurements of the Py/DMPI photocurrents was used to elucidate the mechanism of carrier formation. This approach has been applied to 6,13-bis(triisopropylsilylethynyl) pentacene (TIPS-Pn),[48] which has been extensively studied as an organic semiconductor with high hole mobility. The temperature-dependent EDMR measurements of TIPS-Pn were used to evaluate the photo-carrier generation process.

The present dissertation is constructed using 6 chapters. **Chapter 1** is an introduction of the weak interacting spin pairs and MFE observed in organic semiconductors, and the motivation of this thesis. The experimental details are described in **Chapter 2**. The MFE effect of the photocurrent in two CT complexes is reported in

Chapter 3. The CT characteristics of Py/DMPI and Py/PMDA were investigated using UV-visible absorption and emission spectroscopy and molecular orbital (MO) calculations. The MFE of the photocurrent (MC) was measured using a VVD film deposited on a commercially available interdigitate Pt electrode. The MC behaviour can be reasonably explained assuming two types of collision mechanisms (DD and TD pair mechanisms), which occur between the geminate e–h pair; and between the trapped triplet-species and carrier. A simulation method that considers all the interactions in the DD pair and TD pair mechanisms has been established. The temperature dependence measurement of the CT complex of Py/DMPI is described in **Chapter 4**. TRESR, photocurrent, and EDMR measurements were carried out and their temperature dependence was carefully examined. The trap depth of the triplet excitons was determined using the temperature dependence of TRESR, and the trapping of the majority of triplet excitons was proven, which was assumed in **Chapter 3**. The activation energy for carrier generation from the excited state was determined using the temperature variation of the photocurrent. The e–h pair was directly detected using EDMR and the activation energy for the production of charge carriers from the e–h pairs evaluated based on their temperature variation measurements. Based on the combination approach using the photocurrent, EDMR study, and theoretical simulations established in **Chapter 2-4**, the carrier generation process of TIPS-Pn has been clarified in **Chapter 5**. The temperature dependence of the photocurrent and EDMR was carefully examined. The spectral intensity of the EDMR increased from 80 to 200 K and then decreased from 200 to 310 K. The temperature dependence of the EDMR has been simulated using quantum mechanical simulations of the excited state and carrier dynamics of the e–h pair as well as the analytical solution used for the kinetic rate equation. This analysis method of EDMR will lead to a clarification of the mechanism of carrier generation from the excited state via an e–h pair in an organic semiconductor. A summary of my doctoral work is provided in **Chapter 6**.

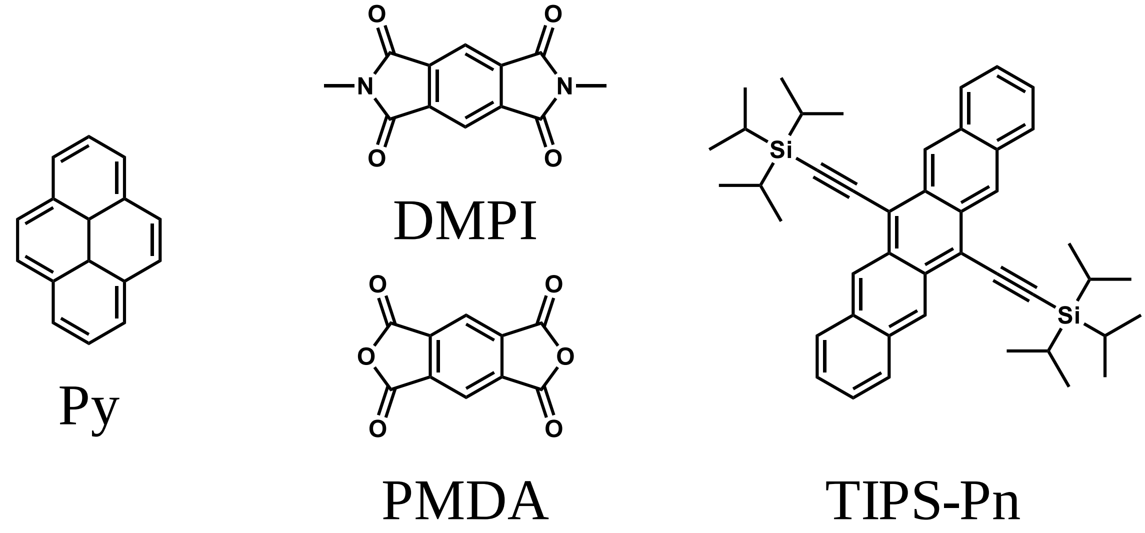

Fig. 1-5. Molecules studied in this thesis.

Chapter 2

Methods

2-1. Sample Preparation

DMPI was synthesised from PMDA (≥99%, HPLC grade, Wako Chemical Japan) using a one-pot reaction with methylamine in a 40% (w/w) aqueous solution. Pyrene (≥98%, HPLC grade, Wako Chemical, and ≥ 98%, GC grade, Kanto Chemical) and DMPI were purified upon repeated sublimation twice. Single crystals of the Py/DMPI and Py/PMDA CT complexes were grown via the diffusion method in acetonitrile purified by distillation. TIPS-Pn crystals (≥99%, HPLC grade, Sigma-Aldrich Japan) were used without further purification.

Vacuum vapor deposition (VVD) is a method of forming thin films upon evaporating a material and attaching it to the surface of a substrate. In this study, CT complexes and TIPS-pentacene thin films were fabricated using the VVD method.

VVD films of Py/DMPI, Py/PMDA, and TIPS-Pn were fabricated on a commercially available interdigitated platinum electrode with 10 µm gaps (DropSens, G-IDEPT10) or a custom-made interdigitated Pt electrode (Tohnic Inc., substrate: quartz, 125 × 2 digits, digit length: 10 µm, gap: 10 µm, thickness: 150 ±15 nm Pt with 40 ±4 nm Ti) using a resistance–heating-type vacuum evaporation apparatus (Sanyu Electron SVC-700TM/ 700-2). Ground single crystals were used as the materials in the vapor deposition step.

Glass substrate
Dimensions: L 22.8 × W 7.6 × H 0.7 mm
Cell constant for 10 µm
Number of digits: 125 × 2
With a digit length: 6.76 mm

Quartz substrate
Dimensions: L 25.0 × W 3.3 × H 0.5 mm
Cell constant for 10 µm
Number of digits: 125 × 2
With a digit length: 3.00 mm

Fig. 2-1. Schematic diagram of interdigitated electrodes (a) DropSens, G-IDEPT10, (b) Tohnic Inc., custom-made interdigitated Pt electrode

2-2. Conventional Measurements

2-2-1. Absorption and Emission Spectroscopy

UV–visible absorption and emission spectroscopy provide information on the electronic states of the ground and excited states, respectively. UV–visible absorption spectrum of the organic solution and the transmission spectrum of the film were measured using a spectrometer (UV/Vis/NIR, Shimadzu UV-3600). The UV-visible diffuse reflectance spectrum of the ground powdered sample was obtained using a spectrophotometer (Hitachi U-3500). Emission spectrum measurements were carried out on a home-built set-up consisting of a Q-switched Nd:YAG LASER (Continuum Surelite II, 7 ns fwhm, and 10 Hz) as the excitation light source. An excitation light of $\lambda = 355$ nm was used for the measurement. The measurement apparatus was constracted by imaging spectrograph (Acton SpectroPro2300i), intensified CCD camera (Princeton Instruments PI-MAX). and digital delay pulse generator (Stanford Research Systems DG645) and Nd:YAG LASER. The emission light was detected using an intensified CCD camera detector, followed by an imaging spectrograph. CW emission spectra were observed by opening the detection gate.

2-2-2. Cyclic Voltammetry

Cyclic voltammetry (CV) is a method that involves cycling the potential of the working electrode and measuring the current of the solution sample. Information on the HOMO and LUMO energy levels of the molecule was obtained from the redox potential using CV.

The electrochemical properties were studied using CV. Dichloromethane was used as the solvent and 0.1 M tetra-*n*-butylammonium hexafluorophosphate ($TBAPF_6$; ≥97%, NT grade, Sigma-Aldrich), which was purified via recrystallisation from ethanol twice, was used as the supporting electrolyte. The observed potentials were corrected for the potential of Fc/Fc^+ using ferrocene as the standard.

2-3. Specific Property Measurements

2-3-1. Photocurrent Measurements

When the organic semiconductor is irradiated with light, the photoexcited electron and hole are produced on the conduction band (LUMO) and the valence band (HOMO), respectively, which generates an e–h pair. The e–h pair dissociates into charge carriers when a bias voltage is applied to the excited organic semiconductor.

The photocurrents were measured using a picoammeter (KEITHLEY Model6487, Picoammeter/Voltage Source) under illumination from a xenon lamp (USHIO, UI-501C), followed by a 5 cm pass-length water filter and UV-visible liquid optical light guide. Excitation light was irradiated on the back of the platinum electrode coated with the VVD film. Band-pass filters (Edmund Optics, CWL, 12.5 mm Dia. hard coated OD4 50 nm) were used for the wavelength dependence measurements. A bias voltage was applied to the electrodes in the conductivity measurements.

2-3-2. Magnetic Field Effect Measurement

Measuring the magnetic field effects on the photocurrent can provide information on the carrier dynamics in organic semiconductors resulting from spin dynamics because weakly interacting spin pairs (such as e–h pairs, pairs of triplet excitons and carriers) are sensitive to the magnetic field. Spin conversion within the weakly interacting pairs caused by the magnetic field in organic semiconductors changes the efficiency of photocurrent generation. A schematic diagram of the photocurrent measurement is shown in **Fig. 2-2**.

The magnetic field effect on the photocurrent was measured by repeatedly increasing and decreasing the applied magnetic field using an iron-core magnet (JEOL JES-TE300). In order to remove artifacts, the data obtained from 20 repeated field cycles were averaged. The system was stabilized for 2 h under irradiation prior to the measurement.

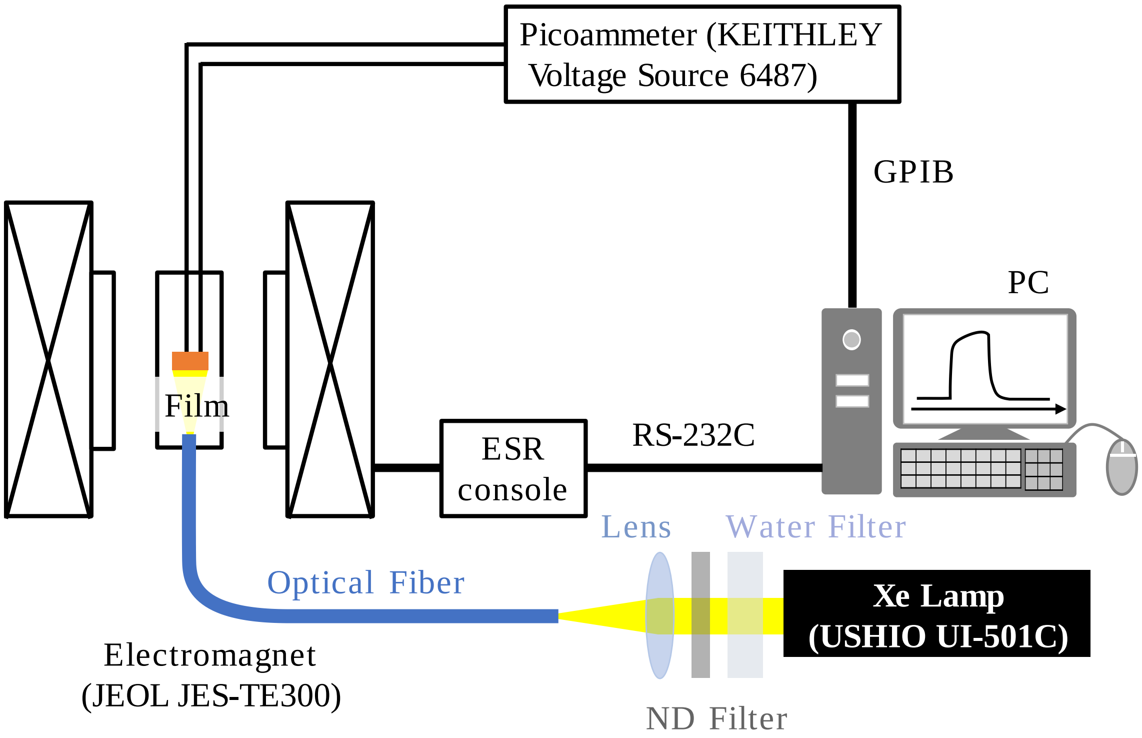

Fig. 2-2. Schematic diagram of the TRESR spectrometer.

2-3-3. Time-resolved Electron Spin Resonance

Time-resolved electron spin resonance (TREPR) spectroscopy is a powerful tool used to detect short-lived paramagnetic species, such as chemical reaction intermediates and excited states, which was pioneered by Kim and Weissman.[49] TREPR can detect the time evolution of the dynamic spin polarisation generated by chemical reactions or intersystem crossing after pulsed laser excitation, which is observed as the direct absorption or emission of the microwave for the samples on a high-speed oscilloscope after amplification using a wide-band preamplifier. The spectrum was obtained by stepwise sweeping of the magnetic field.

TRESR spectra were measured on a laboratory-built apparatus using an X-band ESR spectrometer (JEOL JES-TE300) without magnetic field modulation, wide-band preamplifier, high-speed digital oscilloscope (LeCroy 9350C), and Nd:YAG pulse laser (Continuum Surelite II, 7 ns fwhm, and 10 Hz). Excitation was carried out at 532 nm using the 2nd harmonic of the Nd:YAG LASER. A laser pulse of typically 4–7 mJ/pulse was used in the excitation. The sample temperature was controlled using a cooled He gas flow system (Oxford ESR910 Cryostat and Oxford, Mercury iTC 503). A schematic diagram of the TRESR measurement is shown in **Fig. 2-2**.

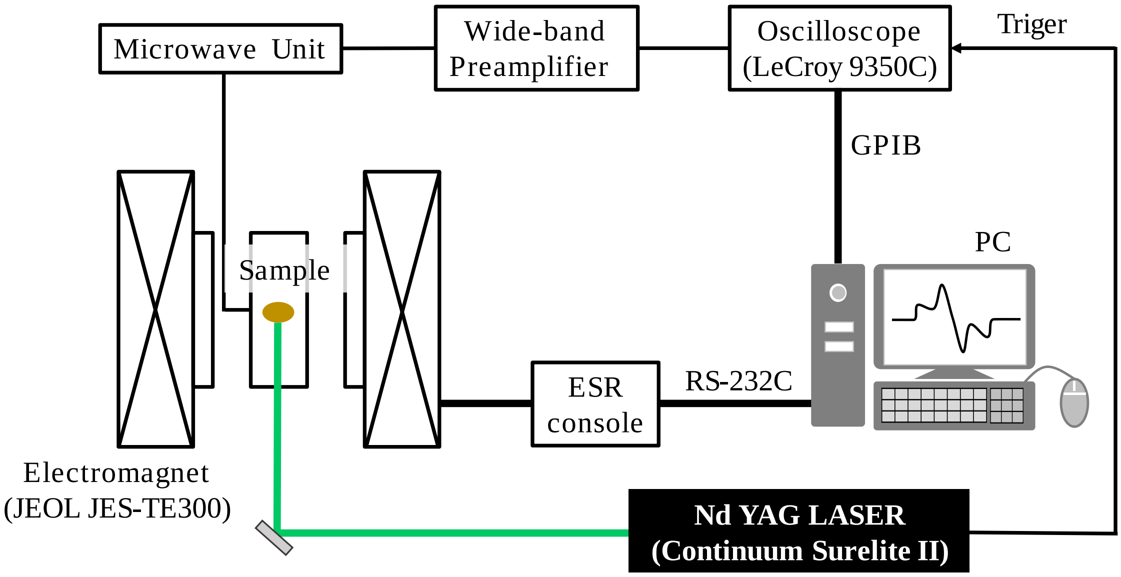

Fig. 2-3. Block diagram of the TRESR spectrometer.

2-3-4. Electrically Detected Magnetic Resonance

Electrically detected electron spin resonance (EDMR) spectroscopy is a method used to measure the change in the current or voltage associated with ESR in a material, and was first reported by Lepine.^{31} The advantage of EDMR spectroscopy is its significantly higher sensitivity than conventional ESR and provides direct insight into how weakly interacting spin pairs act in semiconductors.

A schematic diagram of the EDMR measurement system is shown in **Fig. 2-3**. EDMR measurements were performed on an X-band ESR spectrometer (JEOL, JES-TE300) and an external lock-in amplifier (Signal Recovery, model 7280) used to acquire the signal. A thin film wired to a coaxial cable was introduced into the ESR cavity (TE011 mode). A voltage was applied to the sample from an external power supply (MATSUSADA Voltage source, P4K-36) and the measured current was amplified using an operational amplifier in the custom-made interface circuit and converted into a voltage to feed the output signal into a lock-in amplifier. A square wave (TTL signal) was fed from a function generator (TEXIO, AFG-2012) into a p-intrinsic-n diode (PIN) modulator connected to the microwave oscillator in order to modulate the amplitude of the microwave. At the same time, a reference signal was fed into the lock-in amplifier and the EDMR signal was measured using a phase-sensitive detection technique. Direct detection of the change in the photocurrent induced by ESR (without amplitude modulation) was also performed using a picoammeter. All instruments used for the photocurrent and EDMR measurements were computer-controlled using a LabVIEW-based program made in our laboratory. The sample temperature in the photocurrent and EDMR measurements was controlled using a cooled N_2 gas flow system (Oxford ESR900 Cryostat and Oxford, Mercury iTC).

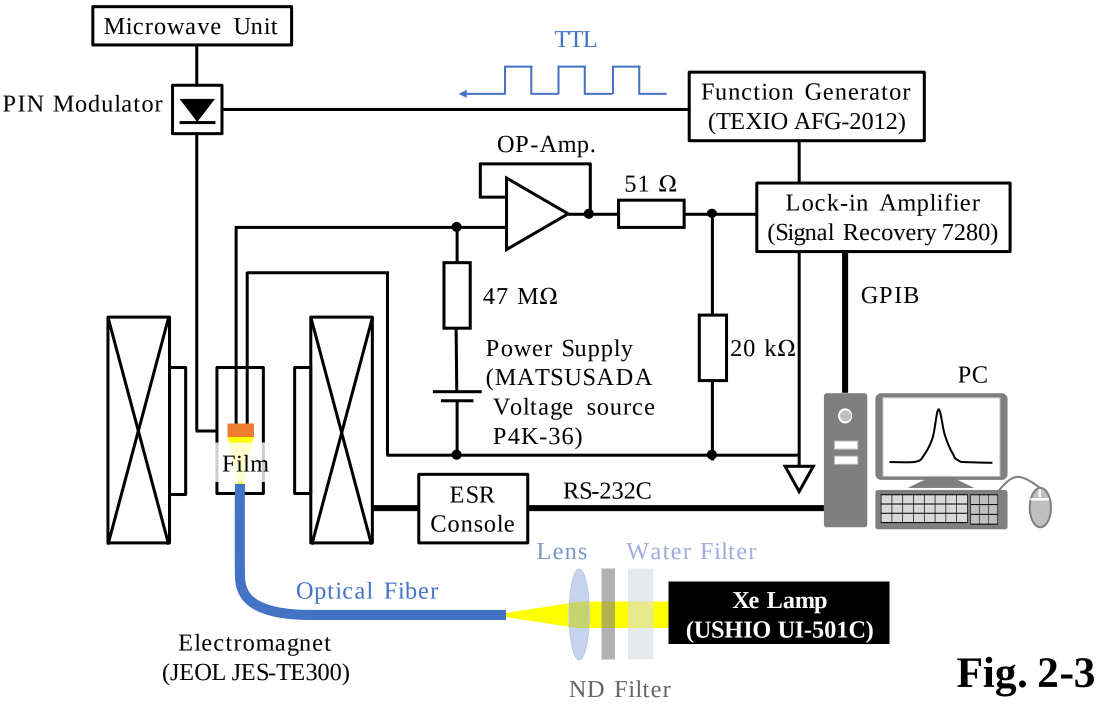

Fig. 2-4. Schematic diagram of the EDMR spectrometer.

2-4. DFT Calculations

Molecular orbital (MO) calculations were carried out using Gaussian 09W[50] and ORCA 4.0 program packages.[51] Density functional theory (DFT) was used to calculate the electronic structure and physical properties of the molecules and ions. MO calculations of the CT complex were performed using DFT with the RB3LYP level of theory for the molecular structures determined by crystallographic analysis. Optimization of the ground-state geometries of the radical ions for each component in the CT complex (Py and DMPI) was carried out using DFT with the UB3LYP level of theory. The 6-31G(d,p) basis set was chosen for all of the present calculations. Time-dependent (TD)-DFT calculations were also performed to estimate the energies and oscillator strengths of the transitions from the ground state to the three lowest-energy singlet states. The images of the molecular orbitals of the complexes were plotted using GaussView 5.0. The g and fine structure tensors were also calculated using DFT with the UKS B3LYP/G level of theory for the optimized structure of pyrene and for the X-ray structures determined for the CT complexes using the ORCA program package. The dipolar spin–spin contribution in the D tensor was directly carried out using the canonical orbitals obtained for the spin density (DIRECT method) and the spin–orbit contribution was calculated using the quasi-restricted orbital (QRO) method.

2-5. Spectral Simulation Using Stochastic Liouville Equation

The behaviour of the spins in the magnetic field was determined using the statistical expectation value of the spin operator at a given time. There are a large number of spins in the system concerned with the magnetic field effect. In order to treat them statistically, one can define the density operator ρ as follows:

$$\rho = \sum_{i,j} P_{ij} \, |\psi_i\rangle\langle\psi_j| \, , \tag{2.1}$$

where P_{ij} represents the statistical probability ($i = j$) and quantum coherence ($i \neq j$). The matrix representation of the density operator is called the density matrix. The statistical expectation value $\langle A \rangle$ of an observable A can be calculated using the density matrix as follows:

$$\langle A \rangle = \mathrm{Tr}\langle \rho A \rangle = \mathrm{Tr}\langle A \rho \rangle \, . \tag{2.2}$$

In order to discuss the magnetic field response of a statistical ensemble of spins, such as ESR and MFEs, it is necessary to solve the time evolution of the density matrix. Since the time evolution of the state ket $|\psi_i\rangle$ can be expressed by means of the Schrödinger equation, the time evolution of the density matrix is given by:

$$\begin{aligned}\frac{\hbar}{i}\frac{\mathrm{d}\rho}{\mathrm{d}t} &= -\sum_{i,j}\left[HP_{ij}|\psi_i\rangle\langle\psi_j| - P_{ij}|\psi_i\rangle\langle\psi_j|H\right] \\ &= -[\rho, H].\end{aligned} \tag{2.3}$$

This equation is known as the von Neumann equation.

The density matrix is an $n\times n$ matrix and the commutator exists in this equation. In addition, there is a type of reaction pathway for each species, such as dissociation to the carrier (e + h) from the e–h pair in the cases discussed in this study. The reaction can be expressed using the density matrix, $-k_{\mathrm{q}}\rho$. Then, there is a coexistence of the commutators $\rho H - H\rho$ and $-k_{\mathrm{q}}\rho$. To calculate this easily, a column vector $|\rho_{ij}\rangle$ for each component ρ_{ij} of the density matrix can be introduced. This process can be expressed as follows:

$$\begin{gathered}\underbrace{\begin{pmatrix} & \rho_{ij} & \end{pmatrix}}_{\mathrm{n}\times\mathrm{n}} \rightarrow \underbrace{\begin{pmatrix} \\ \rho_{ij} \\ \\ \end{pmatrix}}_{\mathrm{n}^2\times 1} \\ \langle i|\rho|j\rangle \rightarrow \langle ij|\rho_{ij}\rangle .\end{gathered} \tag{2.4}$$

The expanded space representation of the density matrix is called the Liouville space representation. As we convert the density matrix ρ_{ij} into a density ket $|\rho_{ij}\rangle$, the exchanger of the von Neumann equation is given by a super operator $\boldsymbol{L}_H$ on the density ket as follows:

$$[\rho, H] \rightarrow \boldsymbol{L}_H|\rho_{ij}\rangle = \frac{\hbar}{i}(H\otimes\boldsymbol{E} - \boldsymbol{E}\otimes H^*)|\rho_{ij}\rangle, \tag{2.5}$$

where $\boldsymbol{E}$ is the identity matrix and $\boldsymbol{L}$ is a superoperator acting on the density ket, which is called the Liouvillian. The Liouvillian operates simply on any element of the density ket from the left, so that spin relaxation and annihilation via recombination can be considered. Consequently, the equation for the time evolution of the density operator can be expressed in the Liouville space as follows:

$$\frac{d|\rho_{ij}\rangle}{dt} = -\frac{\hbar}{i}(H\otimes\boldsymbol{E} - \boldsymbol{E}\otimes H^{*})|\rho_{ij}\rangle - \boldsymbol{\Gamma}|\rho_{ij}\rangle = \boldsymbol{L}|\rho_{ij}\rangle\,. \tag{2.6}$$

By introducing relaxation matrix $\boldsymbol{\Gamma}$, the spin relaxation can be considered. The selective generation of the populations to a particular spin sub-level (p) with a kinetic rate k_p can be written using the projection operator Λ_p as follows:

$$k_p\Lambda_p \quad \text{(normal space)} \rightarrow k_p\langle|\boldsymbol{\Lambda_p}|\rangle \quad \text{(Liouville space)}. \tag{2.7}$$

where Λ_p is generally expressed as $\Lambda_p = |p\rangle\langle p|$. A reaction, such as a transition to a different state or dissociation of an e–h pair, can be expressed as follows:

$$-k_q\Lambda_q\rho \quad \text{(normal space)} \rightarrow -\frac{k_q}{2}\left(\boldsymbol{\Lambda}_q\otimes E + E\otimes\boldsymbol{\Lambda}_q\right)\boldsymbol{\rho^L} \quad \text{(Liouville space)}. \tag{2.8}$$

Thus, the general expression of the stochastic Liouville equation for the process shown in **Scheme 2-1** can be written as follows:

$$\begin{aligned}\frac{d\boldsymbol{\rho^L}}{dt} &= -\frac{\hbar}{i}(H\otimes\boldsymbol{E} - \boldsymbol{E}\otimes H^{*})\boldsymbol{\rho^L} + \sum_{\boldsymbol{p}} k_p\langle|\boldsymbol{\Lambda_p}|\rangle\delta(t) \\ &\quad - \sum_{\boldsymbol{q}}\frac{k_q}{2}\left(\boldsymbol{\Lambda}_q\otimes E + E\otimes\boldsymbol{\Lambda}_q\right)\boldsymbol{\rho^L} - \boldsymbol{\Gamma}\boldsymbol{\rho^L} = \sum_{\boldsymbol{p}} k_p\langle|\boldsymbol{\Lambda_p}|\rangle\delta(t) - \boldsymbol{L}\boldsymbol{\rho^L},\end{aligned} \tag{2.9}$$

where

$$\boldsymbol{L} = \frac{\hbar}{i}(H\otimes\boldsymbol{E} - \boldsymbol{E}\otimes H^{*}) + \sum_{\boldsymbol{q}}\frac{k_q}{2}\left(\boldsymbol{\Lambda}_q\otimes E + E\otimes\boldsymbol{\Lambda}_q\right) + \boldsymbol{\Gamma}\,. \tag{2.10}$$

The geminate spin pair generation to the "*r*" state (or spin sub-level) using continuous wave light excitation can be written as $k_r\langle|\boldsymbol{\Lambda}_r|\rangle$. Therefore,

$$\frac{d\boldsymbol{\rho^L}}{dt} = k_r\langle|\boldsymbol{\Lambda}_r|\rangle - \boldsymbol{L}\boldsymbol{\rho^L} \tag{2.11}$$

is obtained for the condition of the continuous light irradiation. This equation can be solved using the steady-state approximation where the time variation is zero as follows:

$$\frac{d\boldsymbol{\rho^L}}{dt} = 0. \tag{2.12}$$

The steady state solution of the density matrix can be easily solved as follows:

$$\boldsymbol{\rho}^{\boldsymbol{L}} = \boldsymbol{L}^{-1} k_r \langle | \boldsymbol{\Lambda}_r | \rangle. \tag{2.13}$$

The MFE behaviour and EDMR spectra were simulated numerically using this stochastic Liouville equation by a program written by MATLAB. The numerical calculations of the MFE and EDMR using the stochastic Liouville equation are explained in detail in **Chapter 3** and **5**, respectively.

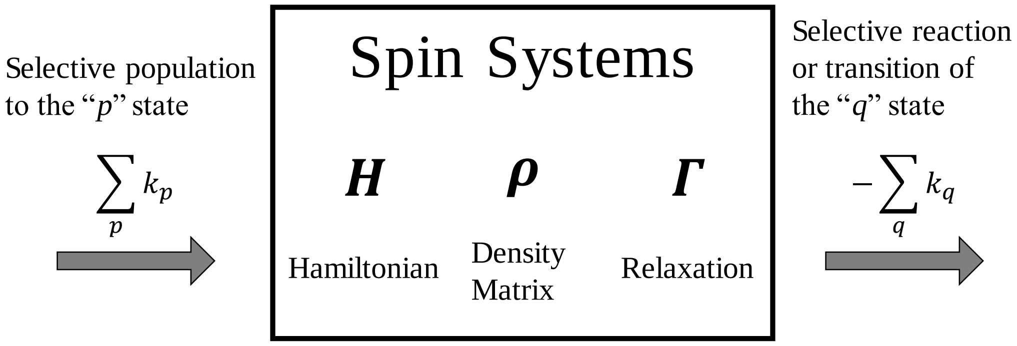

Scheme 2-1. Schematic diagram of spin dynamics in this spin systems.

Chapter 3.

Magnetic Field Effect of the Photocurrent on a Weak Charge Transfer Complex

3-1. Introduction

Recently, spin dynamics have been of great interest in the electricity and light conversion process in organic thin-film devices, such as organic light emitting diodes (OLEDs) and organic solar cells (OSCs). Magnetoconductance (MC) in organic semiconductors can be defined by the change in the current intensity (I) induced by an external magnetic field (B). MC effects are characteristic properties arising from the electron spin degree of freedom and the diffusion of polarized spin carriers. The effects of MC on the current and emission in organic thin-film devices, such as OLEDs and OSCs, have received considerable attention during the last decade.[52-55] The generation and recombination of carriers in organic devices have been studied using the MC effect. In particular, the MC effect in an OLED, which is known as organic magneto-resistance (OMAR), has been extensively investigated because its magnitude is tremendously large (> 1000%) in cases of the magneto-luminescence and magneto-conductance.[24, 25] Although some models (bipolaron model and polaron pair model,) have been proposed,[56] the mechanism of the OMAR is still controversial. In these situations, the photocurrent and its MC effect in the thin films of organic charge-transfer (CT) complexes are worth investigating.

In this study, the mechanisms of the photoconductivity and MC effect have been investigated using vacuum vapor deposition (VVD) films of weak organic CT complexes. A CT complex is an intermolecular compound formed by partial charge transfer between an electron donor (D), which is a molecule that transfers an electron easily to other molecules, and an electron acceptor (A), which is a molecule that easily accept an electron from other molecules. The donor is a molecule with a high HOMO level and an small ionisation potential (I_p), while the acceptor is a molecule with a low LUMO level and high electron affinity (E_a). In a weak CT complex, efficient charge separation is expected upon the photoexcitation of the CT band, leading to photoconductivity. In single crystals, the property of the weak CT complex has been well studied. In the past, the effect of MC on the photoconductivity due to the spin pairs (such as e–h, ex–c, and TT pairs) of organic CT complexes was studied in detail using single crystals. [22, 35, 57] However, single crystals are unsuitable for device fabrication. Thermal evaporation is much easier for device fabrication and therefore, a re-examination of the photocurrent behaviour of the VVD films of weak CT complexes is worthy of investigation. In this chapter, the photoconductivity and its MC effect on VVD films are reported for two kinds of weak CT complexes, pyrene/dimethylpyromellitdiimide (Py/DMPI) and pyrene/pyromellitic dianhydride (Py/PMDA). Time-resolved electron spin resonance (TRESR) measurements of both polycrystalline powders were carried out to obtain information on the photo-excited states. The spin-dependent carrier dynamics resulting in the MC effect have also been described using quantum-mechanical simulations utilising the spin Hamiltonian parameters determined from TRESR, and the effective hyperfine splitting estimated from the molecular orbital calculations.

3-2. X-ray Crystal Structure Analysis

Single crystals of Py/DMPI and Py/PMDA were grown via the diffusion method using acetonitrile purified by distillation under an argon atmosphere as the solvent. The obtained crystals of Py/DMPI and Py/PMDA were yellow and red, respectively, as shown in **Fig. 3-1a** and **3-2a**. X-ray crystallographic analyses[58] were carried out on a Rigaku AFC11 with a Saturn 724+ CCD diffractometer using graphite-monochromated Mo Ka radiation (λ = 0.710747 Å). X-ray structure analysis of these crystals was conducted by Dr. R. Tanaka (the Analytical Centre of Osaka City University). The crystal structure of Py/DMPI is monoclinic, containing four Py and DMPI molecules per unit cell and an alternating stacked structure with donor and acceptor molecules superimposed on each other with an inter-plane distance of 3.678 Å. The crystal structure of Py/PMDA is also monoclinic, containing two Py and PMDA molecules per unit cell and an alternating stacked structure with donor and acceptor molecules superimposed on each other with an inter-plane distance of 3.634 Å. The ORTEP diagrams are shown in **Fig. 3-1** and **3-2**. The details of the results obtained from the X-ray crystallographic analyses are described in **Table 3-1**.

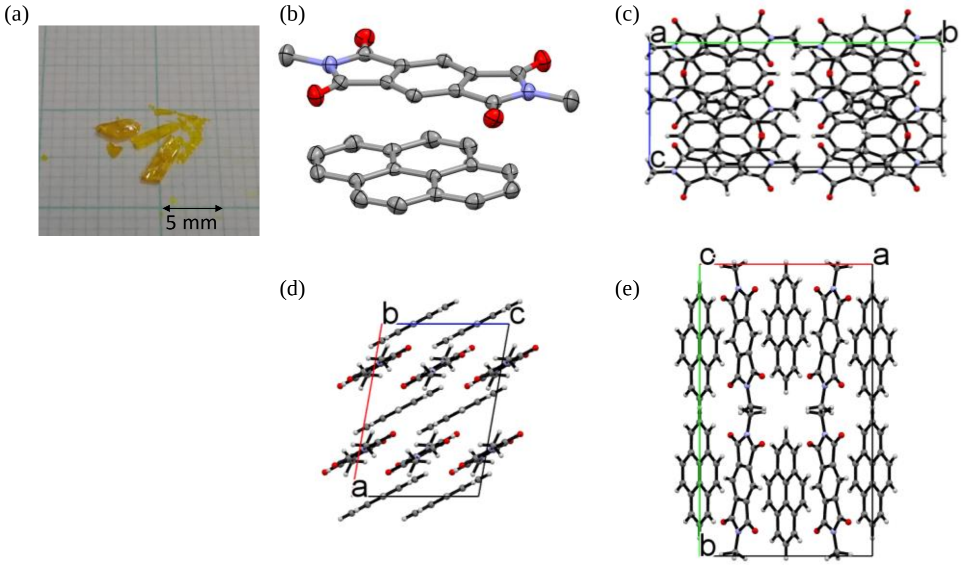

Fig. 3-1. (a) Photograph of the Py/DMPI crystals, (b) ORTEP diagrams (ellipsoids at the 50% probability level; hydrogen atoms are omitted for clarity), and (c) crystal structure viewed along the *a*-axis, (d) *b*-axis, and (e) *c*-axis.

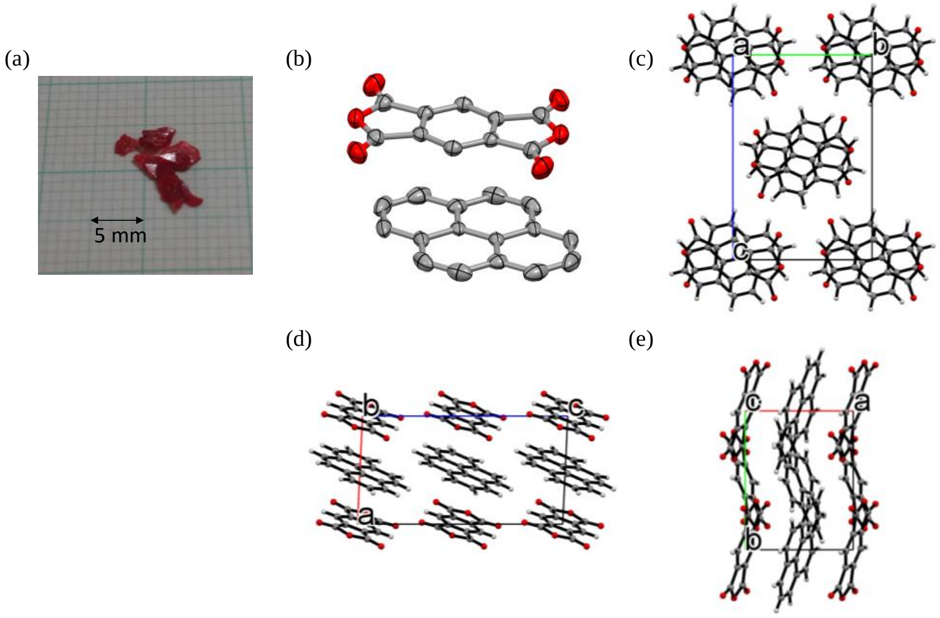

Fig. 3-2. (a) Photograph of the Py/PMDA crystals, (b) ORTEP diagrams (ellipsoids at the 50% probability level; hydrogen atoms are omitted for clarity), and (c) crystal structure viewed along the *a*-axis, (d) *b*-axis, and (e) *c*-axis.

Table 3-1. Crystallographic data for Py/DMPI and Py/PMDA.

Crystallographic data	**Py/DMPI**	**Py/PMDA**
Empirical formula	$C_{28}H_{18}N_2O_4$	$C_{26}H_{12}O_6$
Formula weight	446.44	420.36
Temperature	200(2) K	200(2) K
Wavelength	0.71075 Å	0.71075 Å
Crystal system	Monoclinic	Monoclinic
Space group	*C*2/*c*	*P*21/*c*
Unit cell dimensions		
a/Å	12.019(6)	7.268(6)
b/Å	20.022(9)	9.350(7)
c/Å	8.703(4)	13.757(11)
α/°	90	90
β/°	99.990(5)	92.710(11)
γ/°	90	90
Volume/ $Å^3$	2062.6(16)	933.8(12)
Z	4	2
Density (calculated)/g cm^3	1.438	1.495
Absorption coefficient/ mm^{-1}	0.097	0.107
Goodness-of-fit on F^2	1.099	1.119
Final *R* indices [$I > 2\sigma(I)$]	*R*1 = 0.0405, wR2 = 0.1070	*R*1 = 0.0491, *wR*2 = 0.1114
Crystal size/mm^3	0.200 × 0.150 × 0.100	0.130 × 0.120 × 0.090

3-3. Diffuse Reflection and Emission Spectra, and Molecular Orbital Calculations

Weakly interacting CT complexes have a small amount of charge transfer ($\delta \sim 0$) in the ground state, but in their excited state, almost complete transfer of the electrons from the donor to the acceptor occurs when the CT absorption band is excited.

$$\left(\mathrm{D}^{\delta+}\mathrm{A}^{\delta-}\right) \overset{h\nu}{\rightarrow} \left(\mathrm{D}^{(1-\delta)+}\mathrm{A}^{(1-\delta)-}\right) \qquad (\because \delta \sim 0). \tag{3.1}$$

The CT complexes show a new absorption and emission bands that differ from those of the donor and acceptor. The new bands shift to longer wavelengths with the increasing charge transfer interaction in the ground state. In order to evaluate the extent of CT interaction, the diffuse reflection absorption and emission spectra were measured, as shown in **Fig. 3-3**. The diffuse reflection spectra of Py/DMPI were compared with the absorption spectra of Py and DMPI, respectively. The fluorescence spectrum of Py/DMPI exhibits a maximum at 543 nm and it shifts to a lower energy by 0.35 eV when compared to the wavelength of 475 nm, as the intensity maximum of the Py emission spectrum. The fluorescence spectrum of Py/PMDA exhibits a maximum at 605 nm and it shifts by 0.56 eV when compared with the maximum wavelength of 475 nm observed in the Py emission spectrum. Py/PMDA shows a stronger CT interaction than Py/DMPI, which is consistent with the results predicted using molecular orbital calculations, as shown by the sticks in **Fig. 3-4**.

Since the intense and featureless CT bands observed in the UV–visible region for Py/DMPI and Py/PMDA, the detailed absorption characteristics of the CT complexes were studied based on MO calculations. The excited state transition energies and oscillator strengths of Py/DMPI and Py/PMDA calculated using TD-DFT are summarised in **Table 3-2** and **3-3**, respectively. The data clarify that the lowest-energy absorption transitions of Py/DMPI and Py/ PMDA can be attributed to the HOMO→ LUMO transitions. The one-electron molecular orbital energies are given in **Tables 3-2** and **3-3**. The molecular orbitals are shown in **Fig 3-4** and **Fig 3-5**. It is predicted that the HOMO in the CT complexes has weight on the π-orbital of pyrene and the LUMO has weight on the π-orbital of the accepter.

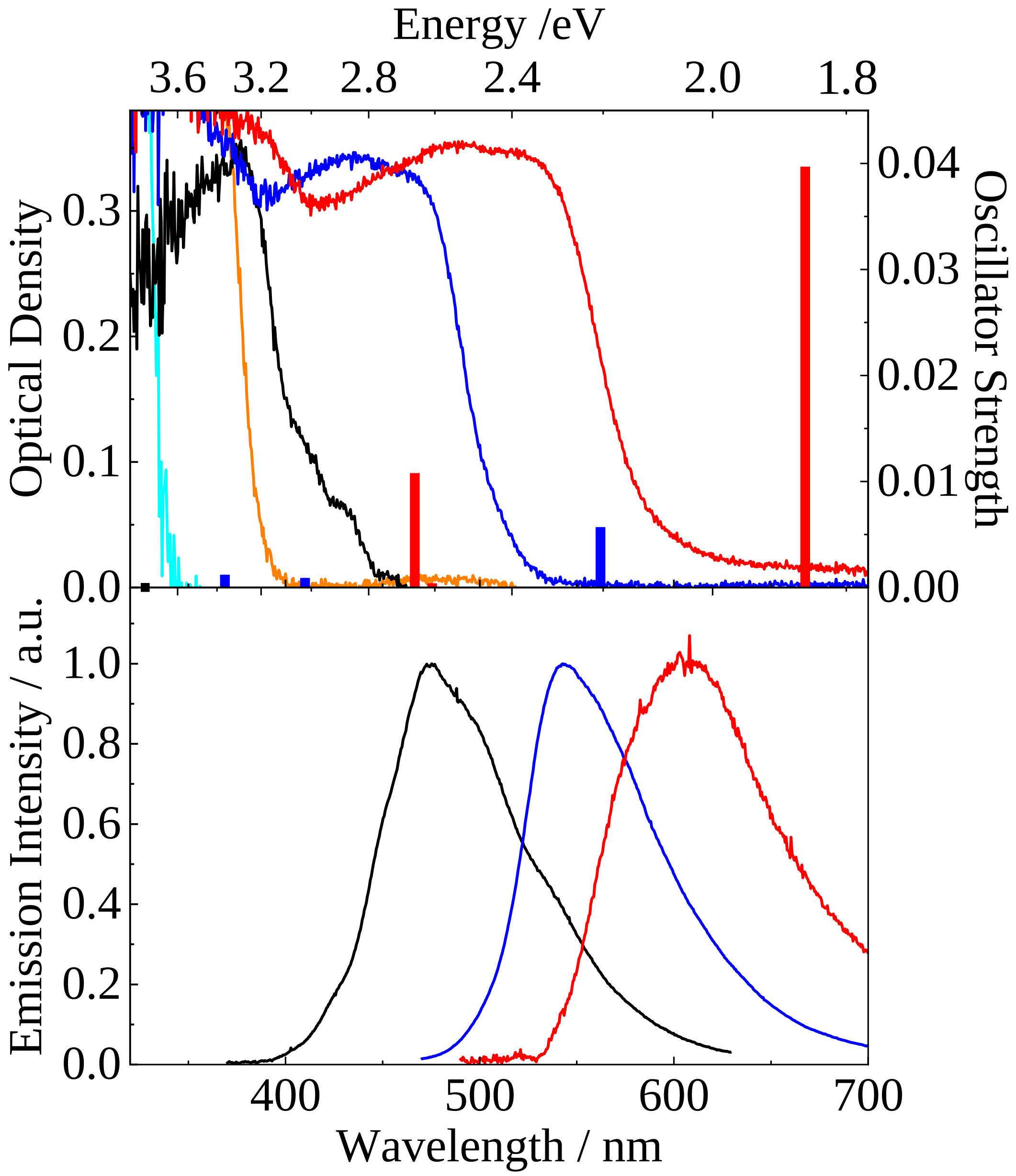

Fig. 3-3. The UV-visible diffuse reflectance and emission spectra obtained for PMDA (cyan), DMPI (orange), pyrene (black), Py/DMPI (blue) and Py/PMDA (red). The sticks are the optical transitions with CT character obtained using TDDFT calculations.

Table 3-2. Calculated excited state of Py/DMPI.

Excited state	Transition	Energy (Wavelength)	Oscillator strength
1	HOMO → LUMO	2.2055 eV (562.16 nm)	0.0057
2	HOMO−1 → LUMO	3.0239 eV (410.02 nm)	0.0009
3	HOMO → LUMO+1 (15%) HOMO → LUMO+2 (85%)	3.3618 eV (368.80 nm)	0.0012

Table 3-3. Calculated excited state of Py/PMDA.

Excited state	Transition	Energy (Wavelength)	Oscillator strength
1	HOMO → LUMO	1.8573 eV (667.57 nm)	0.0397
2	HOMO → LUMO+1	2.6074 eV (475.50 nm)	0.0004
3	HOMO−1 → LUMO	2.6571 eV (466.61 nm)	0.0108

Table 3-4. Molecular orbital energy of Py/DMPI.

Molecular orbital	Energy/Hartrees	Energy/eV
LUMO+2	−0.07310	−1.9892
LUMO+1	−0.09400	−2.5579
LUMO	−0.12546	−3.4139
HOMO	−0.21283	−5.7914
HOMO−1	−0.24572	−6.6863

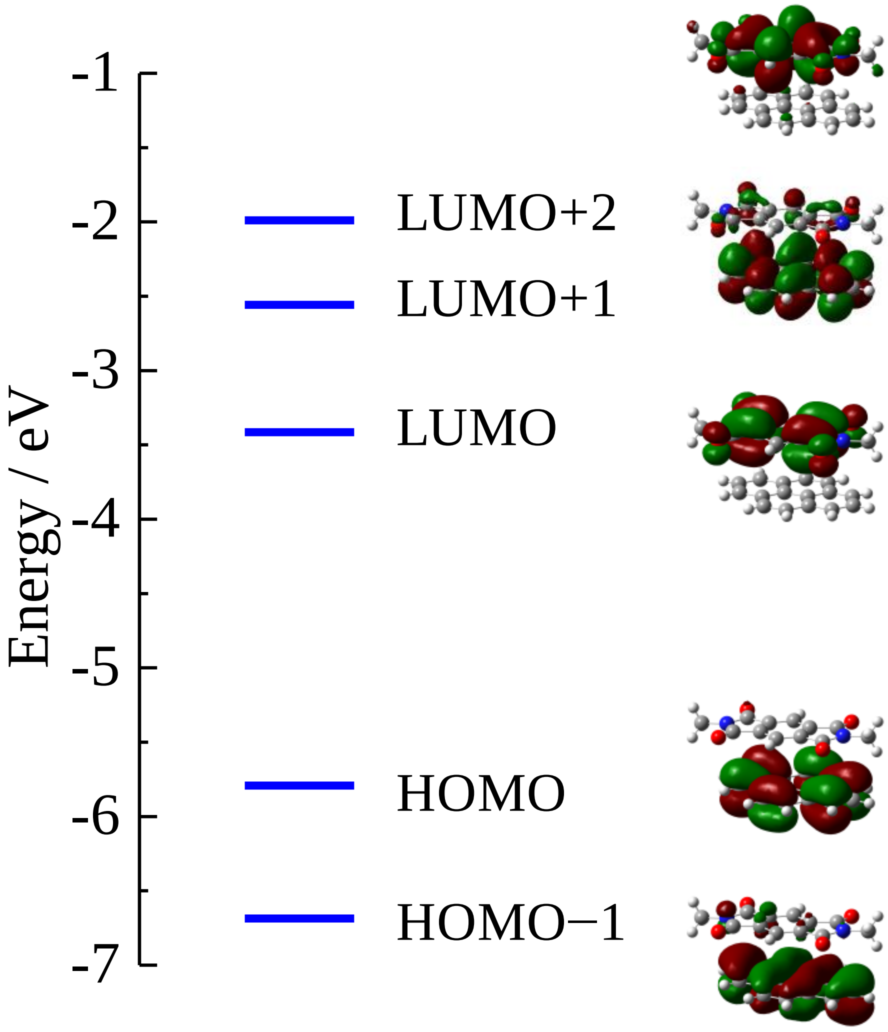

Fig. 3-4. Molecular orbitals and orbital energies of Py/DMPI.

Table 3-5. Molecular orbital energy of Py/PMDA.

Molecular Orbital	Energy/Hartrees	Energy/eV
LUMO+2	−0.05686	−1.5472
LUMO+1	−0.06224	−1.6936
LUMO	−0.10087	−2.7448
HOMO	−0.20399	−5.5509
HOMO−1	−0.23550	−6.4082

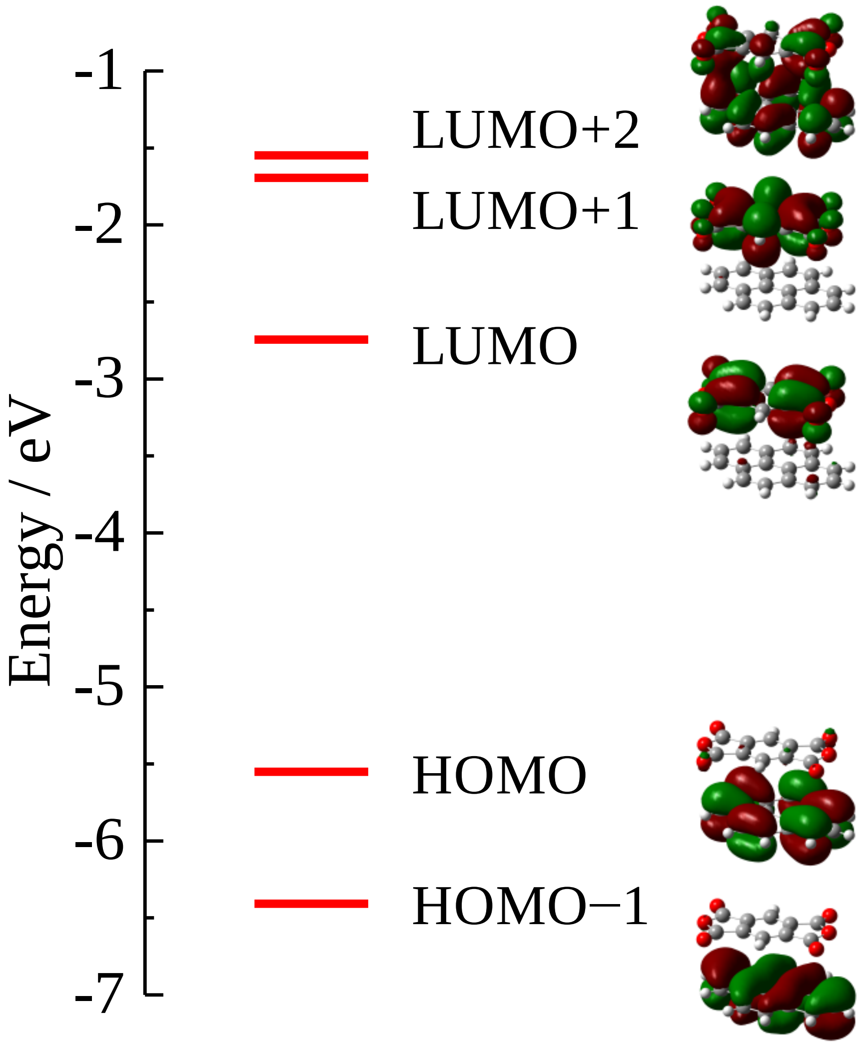

Fig. 3-5. Molecular orbitals and orbital energies of Py/PMDA.

3-4. TRESR Spectra of Weak CT Complexes

The CT character of the triplet excited states can be assessed using the zero-field splitting parameter (*D* and *E*), which depends on the spin distribution obtained from our TRESR measurements. **Figures 3-6** and **3-7** show the typical TRESR spectra obtained for Py/DMPI and Py/PMDA after photoexcitation, respectively, together with their spectral simulations using the spin Hamiltonian, expressed by **Eqn. 3.2**.

$$\widehat{\boldsymbol{H}}_T = \beta_e \boldsymbol{B} \cdot \boldsymbol{g}_T \cdot \boldsymbol{S_T} + \boldsymbol{S_T} \cdot \boldsymbol{D_T} \cdot \boldsymbol{S_T}. \qquad (3.2)$$

The first term is the Zeeman interaction and the second term is the fine structure interaction. *X*, *Y*, and *Z* in the spectral simulations means the transitions corresponding to the directions of the external magnetic field parallel to the *X*, *Y*, and *Z* principal axes of the fine structure tensor, respectively. From the spectral simulations, the spin Hamiltonian parameters of the triplet state were accurately determined to be g_T = 2.0050 (isotropic), |*D*| = 0.0830 cm^{-1}, and |*E*| = 0.0160 cm^{-1} for Py/DMPI, and g_T (isotropic) = 2.0040, |*D*| = 0.0141 cm^{-1}, and |*E*| = 0.0000 cm^{-1} for Py/PMDA. The magnitude of the *D* value of Py/DMPI was close to that of the localised triplet state of pyrene itself (D_{loc} = 0.0863 cm^{-1} and E_{loc} = 0.0167 cm^{-1} reported in the literature). The relative populations (dynamic electron spin polarisation, DESP) of each M_S sub-level were determined to be *P*x = 0.00, *P*y = 0.92, and *P*z = 0.08 for Py/DMPI and *P*x =1.00, *P*y = 0.00, and *P*z = 0.00 for Py/PMDA, when the signs of the *D* and *E* values were chosen to be positive. These signs will be described later. The TRESR signal of Py/PMDA was much weaker than that of Py/DMPI. This is reasonable because the charge-separated electron-hole pair detected in Py/PMDA was not the lowest excited state.

Usually, the excited triplet state of the CT complex can be described as a superposition of the CT states, where one electron is transferred from the donor to the acceptor and the locally excited triplet states of the donor or acceptor. The triplet wavefunction ($^3\Phi$) of the CT complex can be written in the first approximation as a linear combination as follows:[59]

$$^{3}\Phi_{exp} = C_1 \ ^{3}\Phi_{CS}(\mathrm{D^+A^-}) + (1 - C_1) \ ^{3}\Phi_{loc}(\mathrm{D^*A}), \tag{3.3}$$

where $^{3}\Phi_{exp}$ ($\mathrm{D^+A^-}$) and $^{3}\Phi_{loc}$ ($\mathrm{D^*A}$) are triplet wavefunction of charge separate state and locally excited state, respectively. Neglecting other terms that have been shown to be very small, the zero-field splitting parameter (D) can be written as follows:[60]

$$D_{exp} = C_1^2 D_{CS}(\mathrm{D^+A^-}) + (1 - C_1^2) D_{loc}(\mathrm{D^*A}). \tag{3.4}$$

Since $D_{CS}(\mathrm{D^+A^-})$ is much smaller than $D_{loc}(\mathrm{D^*A})$, the CT character, C_1^2, can therefore be determined from the D_{exp} value obtained in the TRESR experiment, according to the following formula:[61]

$$C_1^2 \cong \frac{D_{loc} - D_{exp}}{D_{loc}}. \tag{3.5}$$

The CT character is estimated to be ca. 4% for Py/DMPI using the observed data. In contrast, the result of the optically detected magnetic resonance experiment of Py/PMDA was cited in a review as unpublished work[61] as follows: The D value was 0.0555 $\mathrm{cm^{-1}}$ for the species caught in shallow traps at 1.2 K. The CT character of ca. 30% was estimated by the shallow trap triplet state of Py/PMDA. In this TRESR experiment, such species caught in the shallow trap could not be detected because the experiment was conducted at room temperature. The small D value of the observed species in Py/PMDA in the present experiment shows that the distance between two unpaired electrons was large. The distance between two localised electron spins was estimated from the D value using the point dipole approximation as follows:

$$D = -\frac{3\mu_0}{8\pi}\frac{(g\mu_{\mathrm{B}})^2}{\langle r^3 \rangle}, \tag{3.6}$$

where μ_0 is vacuum permeability. Using **Eqn. 3.6**, the average spin-spin distance r of the charge separate triplet state in Py/PMDA was estimated to be 5.70 Å from the D value observed in the TRESR spectrum. The spin-spin distance estimated from the D values was larger than the inter-plane distance (3.634 Å) between pyrene and PMDA estimated from X-ray crystallography. This is reasonable because the unpaired electron was delocalized over the whole molecule in both pyrene and PMDA. Therefore, the detected species was expected to be a charge-separated electron-hole pair, which is comprised of an excess electron in the PMDA acceptor (anion radical) and a hole in the pyrene donor (cation radical). For the charge-separated electron-hole pair, the sign of the D value was expected to be negative as in **Eqn. 3.6**. Therefore, the signs of the D value for Py/PMDA was assumed to be negative. Using the ORCA program package, the calculated values obtained for pyrene were D_{loc}(ORCA) = +0.0869 cm^{-1} and E_{loc}(ORCA) = +0.00456 cm^{-1}. These values agree well with the value (D = 0.0863 cm^{-1}) reported in the literature[62] and were also close to those of the experimentally determined values obtained for Py/DMPI. Therefore, the signs of D and E are expected to be positive for Py/DMPI. In contrast, the D value of Py/PMDA was much smaller than that of pyrene and Py/DMPI. The D and E values calculated using ORCA were close to those reported in the literature for the trapped species of Py/PMDA. A comparison of the results obtained using the different calculation methods are also shown in **Table 3-6**. **Table 3-6** shows the better values, which were close to the experimental data, were obtained when “DIRECT” was used for the spin-spin interaction term and “QRO” for the spin-orbit interaction term. The sign of the D value was positive for both pyrene and Py/DMPI.

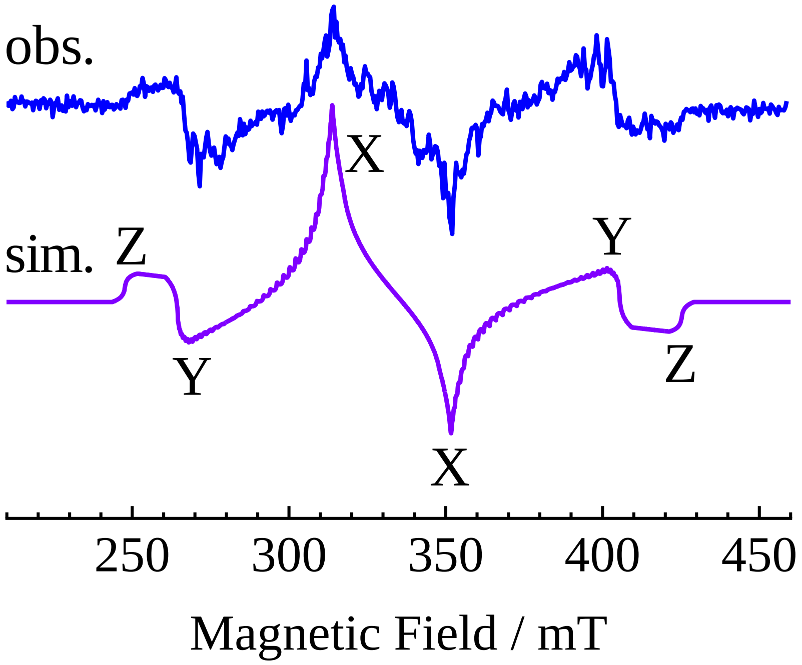

Fig. 3-6. The TRESR spectra obtained for Py/DMPI (blue) and the simulated spectra (violet) at room temperature.

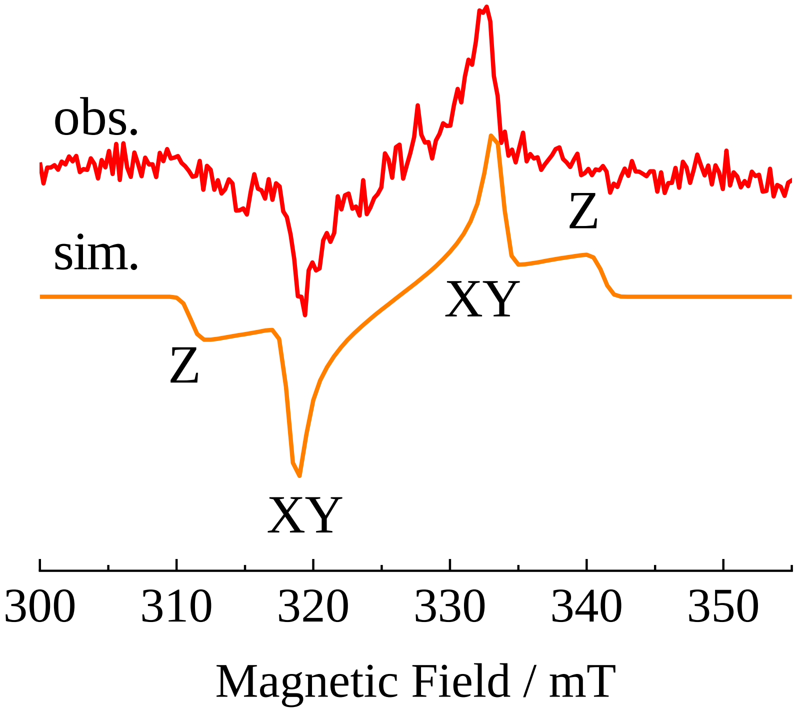

Fig. 3-7. The TRESR spectra obtained for Py/PMDA (red) and the simulation spectra (orange) at room temperature.

Table 3-6. The zero field splitting parameters computed using the ORCA program.

Pyrene	1	2	3	4	obs.[a]
DTensor DSS DSOC	SS DIRECT	SS UNO	SS + SO DIRECT QRO	SS + SO UNO QRO	
D/cm^{-1}	0.09186	−0.05338	0.086874	−0.06033	0.0863
E/cm^{-1}	0.01086	−0.00415	0.004556	−0.0098	0.0167

Py/PMDA	1	2	3	4	obs.	obs.[b]
DTensor DSS DSOC	SS DIRECT	SS UNO	SS + SO DIRECT QRO	SS + SO UNO QRO		
D/cm^{-1}	−0.05415	−0.02000	0.04456	−0.02955	−0.0141	0.0555
E/cm^{-1}	−0.01638	−0.002276	0.010279	−0.00571	0	0.00883

Py/DMPI	1	2	3	4	obs.
DTensor DSS DSOC	SS DIRECT	SS UNO	SS + SO DIRECT QRO	SS + SO UNO QRO	
D/cm^{-1}	0.068399	−0.036117	0.069092	−0.04585	0.0830
E/cm^{-1}	0.013349	−0.000674	0.007121	−0.00343	0.0160

[a] ref 61, [b] ref 60

3-5. Photocurrent and Magnetic Field Effect of Weak CT Complex Films

Figures 3-8a and **3-9a** show the photocurrent response at a voltage bias of 10 V obtained using 30 s ON/OFF illumination cycles with a xenon lamp. **Figures 3-8b** and **3-9b** show the applied bias dependence of the photocurrent intensity on the Py/DMPI and Py/PMDA thin films, respectively. These photocurrents increased linearly with the applied bias voltage. A much larger photocurrent was detected in Py/DMPI than in Py/PMDA. This is reasonable because weak charge transfer in the ground state leads to an almost complete charge transfer in the excited state. The excitation wavelength dependence of the photocurrent was studied using band-pass filters with full width at half maximum of 50 nm and centred wavelengths of 400, 450, 500, 550, 550, 600, 650, and 700 nm. **Figures 3-8c** and **3-9c** show a comparison of the diffuse reflectance and photocurrent action spectra, in which the photocurrent magnitude divided by the light intensity was plotted against the centre wavelength of the filters. The action spectra are in good agreement with the CT band observed in the diffuse reflectance spectra, indicating that the origin of the photocurrent can be attributed to charge separation via CT band excitation in each complex. To obtain an insight into the carrier dynamics, the MC effect observed in the photocurrent (magneto-photoconductance) was investigated. **Figures 3-8d** and **3-9d** show the MC behaviour observed for the photocurrent with Py/DMPI and Py/PMDA. Accurate measurements were not possible under 3 mT because of the residual magnetisation of the iron core magnet used in the measurement. The efficiency of the observed MC was calculated using the photocurrent (I) observed under a specific magnetic field (B) as follows:

$$MC(\%) = \frac{I(B) - I(3\ \mathrm{mT})}{I(B)} \times 100. \tag{3.7}$$

A positive MC effect (1.2% increase at the maximum) was observed upon increasing the magnetic field in the Py/DMPI and Py/PMDA VVD films, as shown in **Fig. 3-8d** and **3-9d**, respectively. The MC increased significantly at lower magnetic fields ($B \leq 50$ mT) and increased gradually at higher magnetic fields ($B \geq 50$ mT). These MCs were similar to those observed in organic solar cells reported in the literature.[28] The low field component of the MC below 10 mT is assigned to the effect explained by the doublet−doublet (DD) pair mechanism, which exhibits hyperfine interactions with nuclear spins.[63] The high field component with above10 mT is assigned to an effect by the triplet-doublet (TD) pair mechanism. A similar MC behaviour was also observed in the Py/PMDA film. The MC curves of Py/DMPI and Py/MPAD were approximately fitted using triple Gaussian functions (narrow, middle, and broad components). The magnetic field dependence of the MC effect can be fitted by the empirical multiple Gaussian functions. This function applies well to reproduce the functional form of OMAR and magnetoconductance of the OSC.[28 64] Although, the physics of the MFE is entirely different to the empirical functions. Therefore, in **Section 3-6**, the MC effect was reproduced numerically using the Liouville equation to understand the physics of the MC effect.

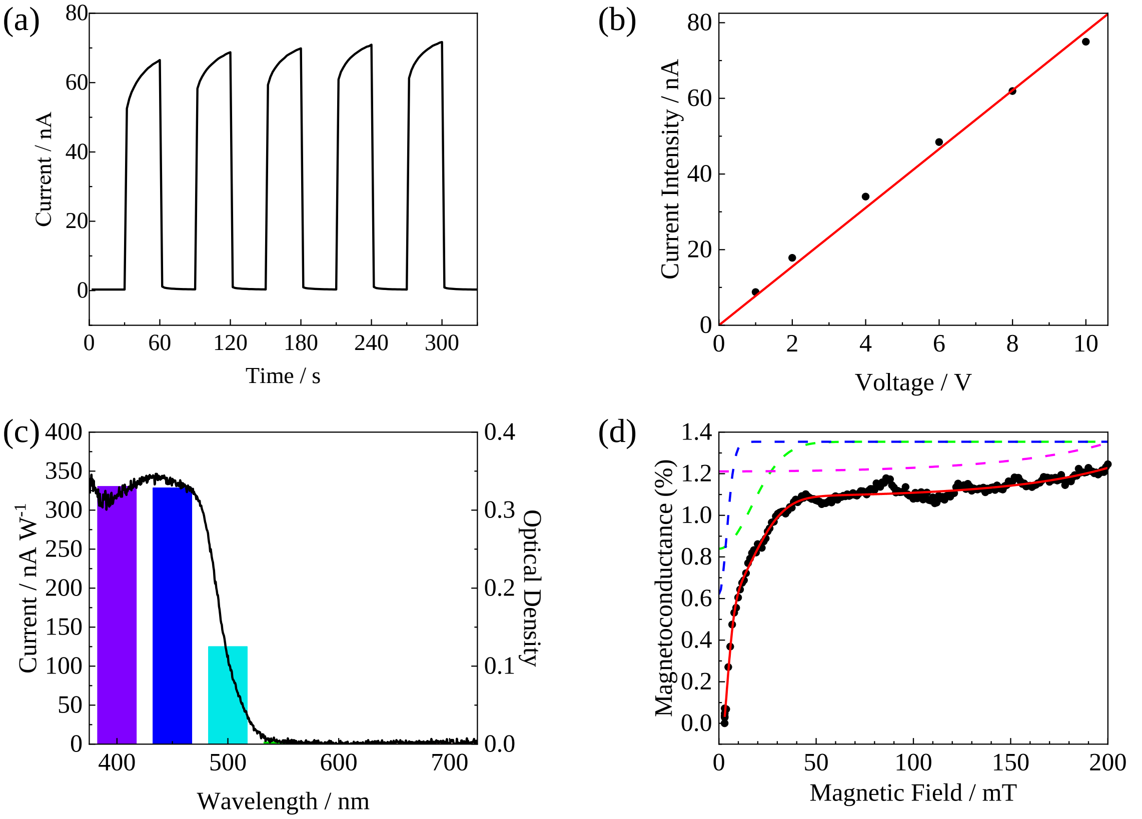

Fig. 3-8. Photocurrent properties of Py/DMPI: (a) Current response to the on/off cycles of light irradiation, (b) bias voltage dependence of the photocurrent intensity, (c) the maximum values of the photocurrent divided by the light power after each band-path filter, and (d) the MC effects observed in the photocurrent of Py/DMPI VVD film. The observed and fitted (red curve) curve were obtained using triple Gaussian functions (blue, green, and purple broken lines).

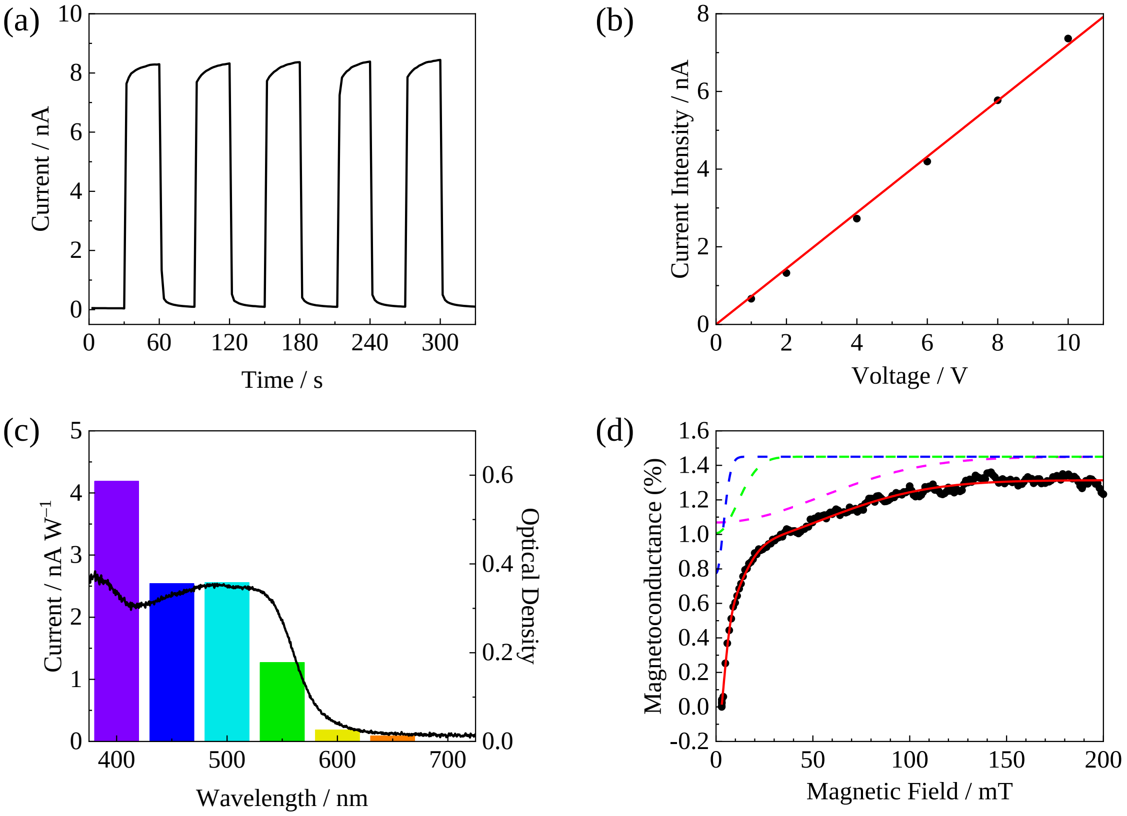

Fig. 3-9. Photocurrent properties of Py/PMDA: (a) Current response to the on/off cycles of light irradiation, (b) bias voltage dependence of the photocurrent intensity, (c) the maximum values of the photocurrent divided by the light power after each band-path filter, and (d) the MC effects observed in the photocurrent of Py/PMDA VVD film. The observed and fitted (red curve) curve were obtained using triple Gaussian functions (blue, green, and purple broken lines).

3-6. Simulation of Magnetic Field Effect on the Photocurrent

In the present system, spin doublet electrons (^{2}e) and spin doublet holes (^{2}h) generated upon photoexcitation become carriers and move among the acceptors or donors by hopping, respectively. The e–h pairs consisting of spin doublet electrons (^{2}e) and spin doublet holes (^{2}h) are ^{1}(e–h) or ^{3}(e–h) pairs. By applying an external magnetic field, the populations of singlet and triplet states are transferred between these two states via B-dependent ISC. When there is a difference in the rate constant of the singlet and triplet pairs, the population transfer via *B*-dependent ISC changes the efficiency of carrier generation. This MFE mechanism can be described using a doublet–doublet (DD) pair mechanism. The triplet exciton (^{3}ex) can also move in the microcrystalline phase of the films. The trapping or detrapping of the carriers or excitons occurs by collisions between them. The collision of a ^{3}ex and a doublet carrier (^{2}c; 2e or 2h) forms the TD pair (ex–c). The TD pairs have spin doublet state ^{2}(ex–c) or spin quartet state ^{4}(ex–c). Therefore, the MC effect is expected to be the *B*-dependent ISC between ^{2}(ex–c) and ^{4}(ex–c). The MFE mechanism can be described using a triplet–doublet (TD) pair mechanism. The excited dynamics, possible pathways, and relation to the DD and TD pair mechanisms are depicted in **Scheme 3-1**.

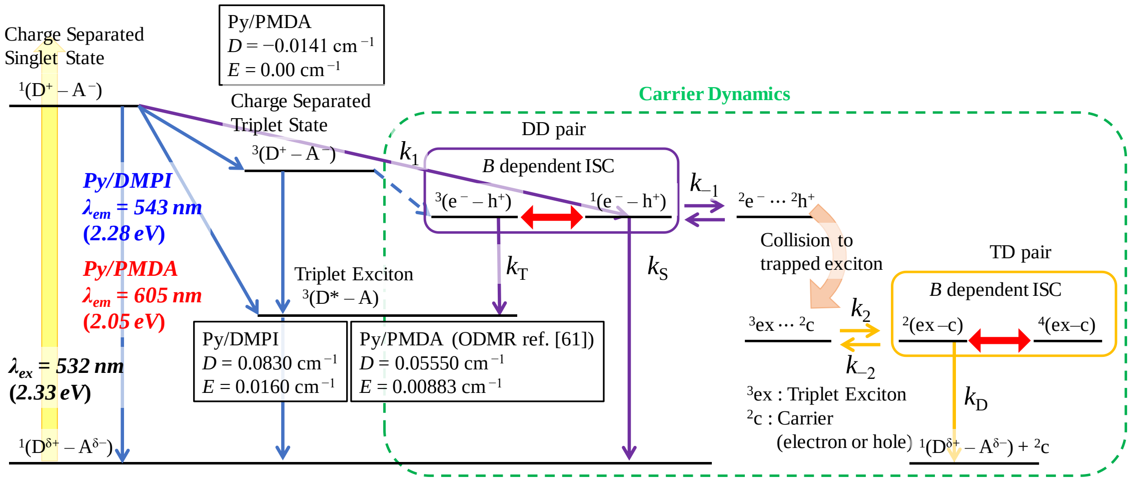

Scheme 3-1. Possible excited and carrier dynamics, and their relation to the DD and TD pair mechanisms.

3-6-1. Doublet–Doublet (DD) pair mechanism

The narrow components in the MC behaviour originate from the DD pair mechanism shown in **Scheme 3-2**. In the DD pair mechanism, *B*-dependent ISC between the ^{1}(e–h) and ^{3}(e–h) pairs arising from the collision of ^{2}e and ^{2}h are described. The DD pair mechanism can be induced by the hyperfine coupling mechanism of the nuclear spins in the low field region. The DD pair mechanism is formulated using the density matrix as shown in **Eqn. 3.8**.

$$\begin{aligned}\frac{\mathrm{d}\boldsymbol{\rho}_{\mathrm{DD}}(t)}{\mathrm{d}t} &= k_1\langle|\boldsymbol{\Lambda}_{\mathrm{S}}|\rangle - k_{-1}\boldsymbol{\rho}_{\mathrm{DD}}(t) - \frac{i}{\hbar}[\boldsymbol{H}_{\mathbf{DD}}, \boldsymbol{\rho}_{\mathrm{DD}}(t)] \\ &\quad - \frac{k_{\mathrm{S}}}{2}\left(\boldsymbol{\rho}_{\mathrm{DD}}(t)\boldsymbol{\Lambda}_S + \boldsymbol{\Lambda}_S\boldsymbol{\rho}_{\mathrm{DD}}(t)\right) - \frac{k_{\mathrm{T}}}{2}\left(\boldsymbol{\rho}_{\mathrm{DD}}(t)\boldsymbol{\Lambda}_T + \boldsymbol{\Lambda}_T\boldsymbol{\rho}_{\mathrm{DD}}(t)\right),\end{aligned} \tag{3.8}$$

where $\boldsymbol{\rho}_{\mathrm{DD}}$ is the density matrix of the e–h pair. The first term, $k_1\langle|\boldsymbol{\Lambda}_S|\rangle$, on the right-hand side represents the selective population of the ^{1}(e–h) pair formed from the singlet excited state upon continuous photoirradiation because the charge-separated singlet excited states (^{1}($\mathrm{D}^+ - \mathrm{A}^-$)) are effectively generated by the direct photoexcitation of the CT band in this type of weak CT complex. The k_1 and k_{-1} are the formative and dissociative diffusion rate constants of the ^{2}e–^{2}h pair. The k_{S} and k_{T} are the recombination rate constants of the pathway to the spin-singlet ground state of the CT complex, ^{1}($\mathrm{D}^{\delta+}$–$\mathrm{A}^{\delta-}$), [singlet channel], and the rate constant of the pathway to the triplet excited state of pyrene in the CT complex, ^{3}(D*–A) [triplet channel], respectively. The spin Hamiltonian of the DD pair mechanism in the third term is given by **Eqn. 3.9**.

$$\begin{aligned}\boldsymbol{H}_{\mathbf{DD}} &= g_{\mathrm{D1}}\mu_{\mathrm{B}}\boldsymbol{B}\cdot\boldsymbol{S}_{\mathbf{D1}} + g_{\mathrm{D2}}\mu_{\mathrm{B}}\boldsymbol{B}\cdot\boldsymbol{S}_{\mathbf{D2}} + \boldsymbol{S}^{\boldsymbol{T}}\cdot\boldsymbol{D}\cdot\boldsymbol{S}^{\boldsymbol{T}} \\ &\quad + \sum_i \boldsymbol{S}_{\mathbf{D1}}\cdot\boldsymbol{A}_{\boldsymbol{i}}\cdot\boldsymbol{I}_{\boldsymbol{D1i}} + \sum_j \boldsymbol{S}_{\mathbf{D2}}\cdot\boldsymbol{A}_{\boldsymbol{j}}\cdot\boldsymbol{I}_{\boldsymbol{D2j}} - 2J\boldsymbol{S}_{\mathbf{D1}}\cdot\boldsymbol{S}_{\mathbf{D2}}.\end{aligned} \tag{3.9}$$

The first and second terms on the right-hand side, $g_{\mathrm{D1}}\mu_{\mathrm{B}}\boldsymbol{B}\cdot\boldsymbol{S}_{\mathbf{D1}}$ and $g_{\mathrm{D2}}\mu_{\mathrm{B}}\boldsymbol{B}\cdot\boldsymbol{S}_{\mathbf{D2}}$ are the Zeeman interactions of hole and electron with the external magnetic field (***B***), respectively. The third term, $\boldsymbol{S}^{\boldsymbol{T}}\cdot\boldsymbol{D}\cdot\boldsymbol{S}^{\boldsymbol{T}}$, is the fine structure (spin–spin) interaction of the triplet state arising from the spin-exchange coupling between the electron and hole carriers (anion and cation radicals). The fourth and fifth terms, $\sum_i \boldsymbol{S}_{\mathbf{D1}}\cdot\boldsymbol{A}_{\boldsymbol{i}}\cdot\boldsymbol{I}_{\mathbf{D1}\boldsymbol{i}}$ and $\sum_j \boldsymbol{S}_{\mathbf{D2}}\cdot\boldsymbol{A}_{\boldsymbol{j}}\cdot\boldsymbol{I}_{\mathbf{D2}\boldsymbol{j}}$, are the sum of the hyperfine coupling interactions of the electron (acceptor anion) and hole (donor cation), respectively. The sixth term, $2J\boldsymbol{S}_{\mathbf{D1}}\cdot\boldsymbol{S}_{\mathbf{D2}}$, is the exchange interaction between the doublet species. $\boldsymbol{\rho_{DD}}(t)$ is the density matrix of the DD pair at time t. $\boldsymbol{\Lambda}_S$ and $\boldsymbol{\Lambda}_T$ are the projection operators to the singlet and triplet spin states of the DD pair, respectively, as follows:

$$\boldsymbol{\Lambda}_S = |S\rangle\langle S|, \tag{3.10}$$

$$\boldsymbol{\Lambda}_T = \sum_i |T_i\rangle\langle T_i|. \tag{3.11}$$

The weak coupled (WC) basis, which can be written as $|S_{\mathrm{D1}}, m_{\mathrm{D1}}\rangle\, |S_{\mathrm{D2}}, m_{\mathrm{D2}}\rangle$, was chosen in the calculation. The selective population of the ^{1}(e–h) pairs, $\langle|\boldsymbol{\Lambda}_S|\rangle$, is given by:

$$\langle|\boldsymbol{\Lambda}_S|\rangle = U_{S(S+1)\to\mathrm{WC}} \begin{pmatrix} 0 & 0 & 0 & 0 \\ 0 & 0 & 0 & 0 \\ 0 & 0 & 1 & 0 \\ 0 & 0 & 0 & 0 \end{pmatrix} U^{+}_{S(S+1)\to\mathrm{WC}} \tag{3.12}$$

where, $U_{S(S+1)\to\mathrm{WC}}$ is the unitary transformation matrix obtained from the eigenfunction basis of the $\boldsymbol{S}^2$ operator to the WC basis.

In the simulation of the DD pair mechanism, the estimated D value (–0.00782 cm^{-1}) of the second nearest contact between donor and acceptor for the third term spin-spin interaction of the spin Hamiltonian (H_{DD}) was used, and it was calculated using **Eqn. 3.6** with the distance (6.937 Å) obtained from the X-ray crystal structure. In this model, the carrier (electron or hole) hops from one molecular site to another, as shown in **Fig. 3-10**. The spin multiplicity is maintained during the stepwise carrier hopping process. The exchange interaction between the electrons and holes at the closest donor-accepter pair is too large to induce a magnetic field effect. The second, third, or fourth contact e–h pairs contribute to the MC effects, as discussed in the literature,[65, 66] but only the second contact pair was used in this simulation.

In the fourth and fifth terms of the spin Hamiltonian, $\boldsymbol{H}_{\mathbf{DD}}$, the summation of the hyperfine tensors in **Eqn. 3.7** was approximated using the averaged effective isotropic hyperfine couplings as follows:

$$\sum_i \boldsymbol{S}_{\mathbf{D1}}\cdot\boldsymbol{A}_i\cdot\boldsymbol{I}_{\mathbf{D1}i} \to a^{eff}_{\mathbf{D1}}\boldsymbol{S}_{\mathbf{D1}}\cdot\boldsymbol{I}_{\mathbf{D1}}\,, \quad \sum_j \boldsymbol{S}_{\mathbf{D2}}\cdot\boldsymbol{A}_j\cdot\boldsymbol{I}_{\mathbf{D2}j} \to a^{eff}_{\mathbf{D2}}\boldsymbol{S}_{\mathbf{D2}}\cdot\boldsymbol{I}_{\mathbf{D2}}\,. \tag{3.7}$$

The hyperfine couplings of the cation radical of pyrene (Py^{+}) and the anon radical of DMPI (DMPI^{-}) were calculated using Gaussian 09W. The calculations were performed using DFT with the UB3LYP level of theory and 6-31G(d,p) basis set to obtain the optimized molecular structures. The calculated isotropic Fermi contact couplings are listed in **Table 3-7**. The spectral hyperfine splitting patterns in the frequency region were calculated as shown in **Fig. 3-11**. The effective isotropic hyperfine couplings of the pyrene cations and DMPI anions were estimated to be $\boldsymbol{a}_{\mathbf{D1}}^{\boldsymbol{eff}} = -30.0$ MHz and $\boldsymbol{a}_{\mathbf{D2}}^{\boldsymbol{eff}} = -8.0$ MHz, respectively, using the weighted average of the split pairs based on their spectral patterns. The signs of $\boldsymbol{a}_{\mathbf{D1}}^{\boldsymbol{eff}}$ and $\boldsymbol{a}_{\mathbf{D2}}^{\boldsymbol{eff}}$ were chosen to be negative because the major isotropic hyperfine couplings of Py^{+} and DMPI^{-} are negative. The anisotropic terms were neglected because their magnitude was much smaller than that of the isotropic terms.

The rate equation in **Eqn. 3.8** was rewritten in the Liouville space as follows:

$$\frac{\mathrm{d}}{\mathrm{d}t}\boldsymbol{\rho}_{\mathrm{DD}}^{L}(t) = k_1\langle|\boldsymbol{\Lambda}_S|\rangle^{L} - \boldsymbol{L}_{\mathrm{DD}}\boldsymbol{\rho}_{\mathrm{DD}}^{L}(t), \tag{3.13}$$

where

$$\boldsymbol{\rho}_{\mathrm{DD}}^{L}(t) = \begin{pmatrix} \rho(t)_{11} \\ \rho(t)_{12} \\ \vdots \end{pmatrix}, \tag{3.14}$$

and

$$\boldsymbol{L}_{\mathrm{DD}}(t) = k_{-1}\boldsymbol{E}\otimes\boldsymbol{E} + \frac{i}{\hbar}(\boldsymbol{H}_{\mathrm{DD}}\otimes\boldsymbol{E} - \boldsymbol{E}\otimes\boldsymbol{H}_{\mathrm{DD}}^{*}) + \frac{k_{\mathrm{S}}}{2}(\boldsymbol{\Lambda}_S\otimes\boldsymbol{E} + \boldsymbol{E}\otimes\boldsymbol{\Lambda}_S^{*}). \tag{3.15}$$

where $\boldsymbol{E}$ is the unit matrix. In the steady-state approximation of $\mathrm{d}\boldsymbol{\rho}_{\mathrm{DD}}(t)/\mathrm{d}t = 0$, the equation to the density matrix can be easily solved as follows.

$$\boldsymbol{\rho}_{\mathrm{DD}}^{L} = k_1\boldsymbol{L}_{\mathrm{DD}}^{-\mathbf{1}}\boldsymbol{\rho}_{\mathrm{DD}}^{L}(0). \tag{3.16}$$

The efficiency of the charge separation, in which the external magnetic field is applied to the (θ, ϕ) direction to the principal axes (X, Y, Z) of the fine structure tensor, can be calculated as follows:

$$\emptyset_{\mathrm{DD}}(B,\theta,\phi) = \frac{k_{-1}}{k_1}Tr(\boldsymbol{\rho}_{\mathrm{TD}}\boldsymbol{E}) = \frac{k_{-1}}{k_1}Tr(\boldsymbol{\rho}_{\mathrm{TD}}). \tag{3.17}$$

Because the molecules are oriented randomly in the sample, the averaged MC effect is given by:

$$\langle \emptyset_{\mathrm{DD}}(B) \rangle = \frac{1}{4\pi} \int_0^{2\pi} \int_0^{\pi} \emptyset_{\mathrm{TD}}(B, \theta, \phi) \sin\theta \, \mathrm{d}\theta d\phi \tag{3.18}$$

The MC effect arising from the DD pair mechanism in the photocurrent is given by:

$$MC(\%) = \frac{\langle \emptyset_{\mathrm{DD}}(B) \rangle - \langle \emptyset_{\mathrm{DD}}(0) \rangle}{\langle \emptyset_{\mathrm{DD}}(0) \rangle} \times 100. \tag{3.19}$$

Simulations were performed by changing the rate constants and exchange interactions in the DD pair mechanism. The MC intensity in the DD-pair mechanism was found to be < 3% for each condition. **Figure 3-12** shows the magnetic field effects of a typical DD pair mechanism. The g values of electrons and holes were assumed to be equal. The fine structure interactions and hyperfine coupling interactions were used by estimatied values of Py/DMPI. **Figures 3-12a** and **3-12b** show the J dependence of the MC curve in the DD pair mechanism. There is no difference in the magnetic field effect when $J/h < |10^6|$ Hz. When the exchange interaction was comparable to the magnetic field energy, the dip appeared due to the level crossing mechanism. The MC curve was not observed when the exchange interaction was sufficiently large. **Figure 3-12c** shows the k_T dependence of the MC curve. The MC curve was not observed when $k_T = k_S$. **Figure 3-12d** shows the k_1 dependence of the MC curve. The MC curve was not observed when k_{-1} was sufficiently large. In contrast, a negative MC curve was observed when k_1 was sufficiently small.

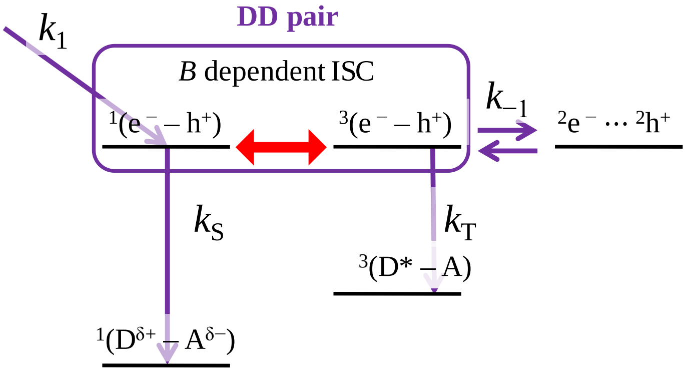

Scheme 3-2. The general scheme of the DD pair mechanism generating the MC effect observed in the photocurrent.

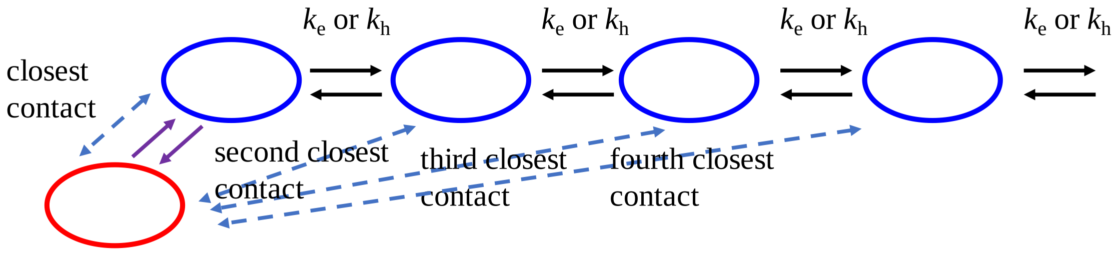

Fig. 3-10. The stepwise electron or hole hopping model.[65, 66]

Table 3-7 The calculated isotropic Fermi contact couplings obtained for the pyrene cation and DMPI anion.

pyrene cation	Isotropic Fermi contact couplings /MHz	DMPI anion	Isotropic Fermi contact couplings /MHz
H(1)	−16.74237	N(14)	−3.12385
H(1)	5.02858	N(14)	−3.12385
H(1)	−16.74386	H(1)	3.40856
H(1)	−6.29519	H(1)	3.40856
H(1)	−6.29312	H(1)	−0.211
H(1)	−6.29901	H(1)	−2.01744
H(1)	−6.2957	H(1)	−2.01743
H(1)	−16.74076	H(1)	−0.211
H(1)	5.02861	H(1)	−2.01744
H(1)	−16.7453	H(1)	−2.01743

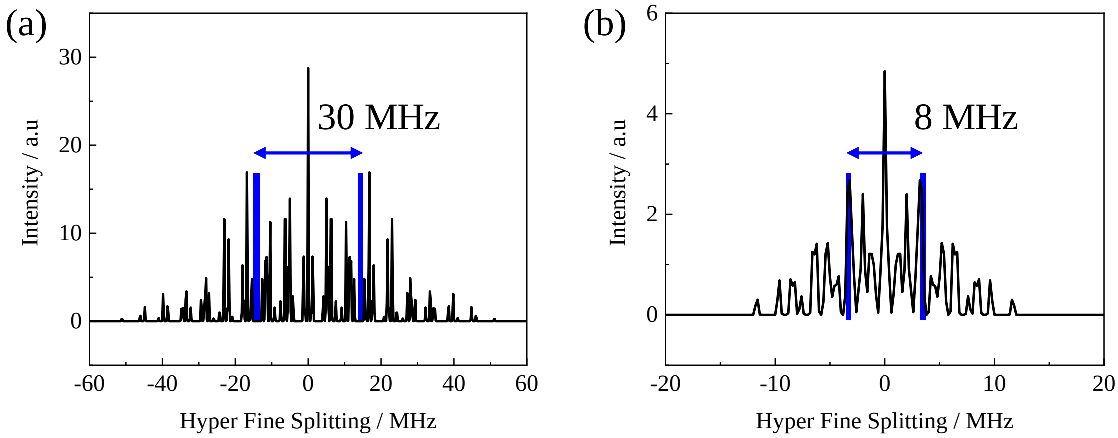

Fig. 3-11. The calculated hyperfine splitting pattern (black) and weight average (blue) obtained for the (a) pyrene cation and (b) DMPI anion, and their effective hyperfine coupling approximated using $\boldsymbol{a}_{\boldsymbol{D}}^{\boldsymbol{eff}}\boldsymbol{S}_{\boldsymbol{D}}\cdot\boldsymbol{I}_{\boldsymbol{D}}$ (S = 1/2 and I = 1/2).

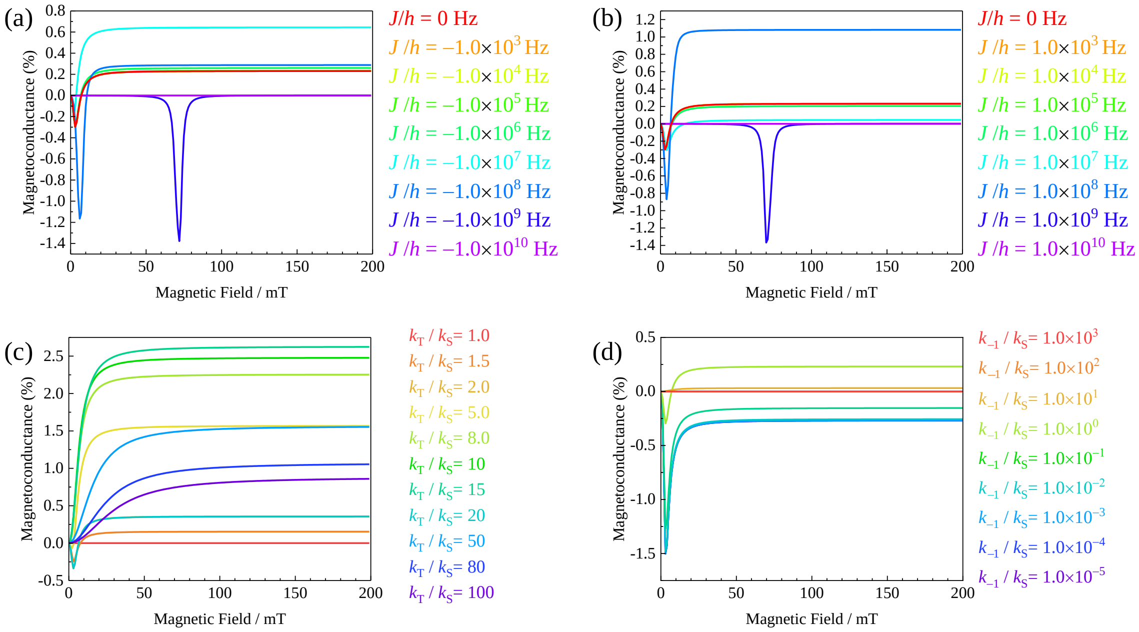

Fig. 3-12. Simulation of DD pair mechanism. The following parameters were used in all simulations: g_{D1} = 2.0030, g_{D2} = 2.0030, D = −0.00782 cm^{-1}, E = 0.0 cm^{-1}, $\boldsymbol{a}_{\boldsymbol{D1}}^{\boldsymbol{eff}}$ = −30.0 MHz, $\boldsymbol{a}_{\boldsymbol{D2}}^{\boldsymbol{eff}}$ = −8.0 MHz, $k_1 = k_{-1}$ and $k_S = 1.0\times10^8$ s^{-1}. (a) and (b) The J dependence of the MC curves ($k_1 = k_{-1}$ = 1.0 × 10^8 s^{-1} and k_T = 1.5 × 10^8 s^{-1}). (c) The k_T dependence of the MC curves ($k_1 = k_{-1}$ = 1.0 × 10^8 s^{-1} and J = 0 cm^{-1}). (d) The k_1 dependence of the MC curves (k_S = 1.0 × 10^8 s^{-1}, k_T = 1.5 × 10^8 s^{-1}, and J = 0 cm^{-1}).

3-6-2. Triplet–Doublet (TD) pair mechanism

The middle and broad components observed in the MC behaviour are expected to originate from the TD pair mechanism shown in **Scheme 3-3**. In this model, B-dependent ISC between the doublet ^{2}(ex–c) and quartet ^{4}(ex–c) pairs arising from the collision of triplet excitons (^{3}ex) and doublet carriers (^{2}c) is described. The TD pair mechanism can be induced by the fine structure interaction. Here, k_2, k_{-2}, and k_D are the formative and dissociative diffusion rate constants of the ^{3}ex–^{2}c pair and the recombination rate constant of the pathway to the ground state, $^1(D^{\delta+}–A^{\delta-})$ + ^{2}c [doublet channel]. This kinetic model is similar to that used for the analysis of the MC effects in a pentacene/C$_{60}$ bilayer solar cell reported by Ikoma *et al.*[65] The TD pair mechanism was expressed using the stochastic Liouville equation of the density matrices, given below:

$$\frac{\mathrm{d}\boldsymbol{\rho}_{\mathrm{TD}}(t)}{\mathrm{d}t} = k_2\boldsymbol{\rho}_{\mathrm{TD}}^{\boldsymbol{cont}} - k_{-2}\boldsymbol{\rho}_{\mathrm{TD}}(t) - \frac{i}{\hbar}[\boldsymbol{H_{TD}}, \boldsymbol{\rho}_{\mathrm{TD}}(t)] - \frac{k_D}{2}\left(\boldsymbol{\rho}_{\mathrm{TD}}(t)\boldsymbol{\Lambda}_D + \boldsymbol{\Lambda}_D\boldsymbol{\rho}_{\mathrm{TD}}(t)\right) \tag{3.20}$$

$$\boldsymbol{H}_{\mathrm{TD}} = g_D\mu_{\mathrm{B}}\boldsymbol{B}\cdot\boldsymbol{S}_D + g_T\mu_B\boldsymbol{B}\cdot\boldsymbol{S}_T + \boldsymbol{S}_T\cdot\boldsymbol{D}_T\cdot\boldsymbol{S}_T - 2J\boldsymbol{S}_D\cdot\boldsymbol{S}_T \tag{3.21}$$

and

$$\boldsymbol{\Lambda}_D = \sum_i |D_i\rangle\langle D_i| \tag{3.22}$$

where $\boldsymbol{\Lambda}_D$ is the projection operator to ^{2}(ex–c), $\boldsymbol{\rho}_{\mathrm{TD}}(t)$ is the density matrix of the TD pair at time t, and $\boldsymbol{\rho}_{\mathrm{TD}}^{\boldsymbol{cont}}$ is supplied by continuous photoexcitation. It was assumed that the dynamic electron spin polarisation observed in the TRESR experiment was maintained. In the calculation, the weak spin-coupled (WC) basis was chosen, which is written as $|S_D, m_D\rangle\,|S_T, m_T\rangle$. The initial density matrix, $\boldsymbol{\rho}_{\mathrm{TD}}$, is given by:

$$\rho_{\mathrm{TD}}^{cont} = \boldsymbol{\rho}_D\otimes\boldsymbol{\rho}_T \tag{3.23}$$

where

$$\boldsymbol{\rho}_D = \begin{pmatrix} 1/2 & 0 \\ 0 & 1/2 \end{pmatrix}, \qquad \boldsymbol{\rho}_T = U_{\mathrm{ZF}\to\mathrm{WC}} \begin{pmatrix} P_{\mathrm{X}} & 0 & 0 \\ 0 & P_{\mathrm{Y}} & 0 \\ 0 & 0 & P_{\mathrm{Z}} \end{pmatrix}_{\mathrm{ZF}} U^{+}_{\mathrm{ZF}\to\mathrm{WC}} \,. \tag{3.24}$$

Here, $U_{\mathrm{ZF}\to\mathrm{WC}}$ is the unitary transformation matrix from the zero-field eigenfunction basis to the WC basis, which is obtained by the diagonalization of $\boldsymbol{H}_{\mathbf{zf}}\, \boldsymbol{S}_T \cdot \boldsymbol{D} \cdot \boldsymbol{S}_T$. In the spin Hamiltonian of the TD model ($\boldsymbol{H}_{\mathrm{TD}}$), the first and second terms, $g_{\mathrm{D}}\mu_B \boldsymbol{B} \cdot \boldsymbol{S}_{\mathbf{D}}$ and $g_{\mathrm{T}}\mu_{\mathrm{B}} \boldsymbol{B} \cdot \boldsymbol{S}_T$, are the Zeeman interactions with the external magnetic field ($\boldsymbol{B}$) of the doublet and triplet species, respectively. The third term, $\boldsymbol{S}_T \cdot \boldsymbol{D} \cdot \boldsymbol{S}_T$, is the fine structure (spin-spin) interaction of the triplet state. The fourth term, $2J\boldsymbol{S}_{\boldsymbol{D}} \cdot \boldsymbol{S}_T$, is the exchange interaction between the doublet and triplet species. The rate equation (**Eqn. 3.20**) was rewritten in the Liouville space as follows:

$$\frac{\mathrm{d}}{\mathrm{d}t}\boldsymbol{\rho}^L_{\mathrm{TD}}(t) = k_2 \boldsymbol{\rho}^{\boldsymbol{cont},L}_{\mathrm{TD}} - \boldsymbol{L}_{\mathrm{TD}} \boldsymbol{\rho}^L_{\mathrm{TD}}(t) \tag{3.25}$$

where

$$\boldsymbol{\rho}^L_{\mathrm{TD}}(t) = \begin{pmatrix} \rho(t)_{11} \\ \rho(t)_{12} \\ \vdots \end{pmatrix} \tag{3.26}$$

and

$$\boldsymbol{L}_{\mathrm{TD}}(t) = k_{-2} \boldsymbol{E} \otimes \boldsymbol{E} + \frac{i}{\hbar}(\boldsymbol{H}_{\mathbf{TD}} \otimes \boldsymbol{E} - \boldsymbol{E} \otimes \boldsymbol{H}^*_{\mathbf{TD}}) + \frac{k_{\mathrm{D}}}{2}(\boldsymbol{\Lambda}_D \otimes \boldsymbol{E} + \boldsymbol{E} \otimes \boldsymbol{\Lambda}_D) \,. \tag{3.27}$$

Here, $\boldsymbol{E}$ is the unit matrix in the spin space of the TD pair. In the steady-state approximation of $\mathrm{d}\boldsymbol{\rho}_{\mathrm{TD}}(t)/\mathrm{d}t = 0$, the equation to the density matrix can be easily solved as follows.

$$\boldsymbol{\rho}^L_{\mathrm{TD}} = k_2 \boldsymbol{L}^{-\mathbf{1}}_{\mathrm{TD}} \boldsymbol{\rho}^{\boldsymbol{cont},L}_{\mathrm{TD}} \,. \tag{3.28}$$

A positive magnetoconductance of the photocurrent appears due to carrier detrapping from the ^{3}ex–^{2}c pair via the TD pair mechanism. The efficiency in the (θ, ϕ) direction of the external magnetic field to the principal axes (X, Y, Z) of the fine structure tensor, $\boldsymbol{D}$, is given by:

$$\emptyset_{\mathrm{TD}}(B, \theta, \phi) = (k_D/k_2) Tr(\boldsymbol{\rho}_{\mathrm{TD}} \boldsymbol{\Lambda}_D). \tag{3.29}$$

Because the molecules are randomly oriented in the sample, the averaged MC effect is given by:

$$\langle \emptyset_{\mathrm{TD}}(B) \rangle = \frac{1}{4\pi} \int_0^{2\pi} \int_0^{\pi} \emptyset_{TD}(B, \theta, \phi) \sin\theta \, \mathrm{d}\theta \mathrm{d}\phi. \tag{3.30}$$

The MC effect arising from the TD pair mechanism in the photocurrent is given as follows:

$$MC(\%) = \frac{\langle \emptyset_{\mathrm{TD}}(B) \rangle - \langle \emptyset_{\mathrm{TD}}(0) \rangle}{\langle \emptyset_{\mathrm{TD}}(0) \rangle} \times 100. \tag{3.31}$$

Simulations were performed by changing the rate constants and exchange interactions in the TD pair mechanism. **Figure 3-13** shows the magnetic field effects of a typical DD pair mechanism. The *g* values and fine structure interactions are used by estimation values of Py/DMPI. **Fig. 3-13a** and **3-13b** show the *J* dependence of the MC curve using the TD pair mechanism. There was no difference in the magnetic field effect when $J/h < |10^6|$ Hz. When only k_2 is changed and other parameters are fixed, no difference is observed, as shown in **Fig. 3-13c**. **Fig. 3-13d** shows the dependence of k_D on the MC curve. A very large MC effect (~500 %) is obtained when $k_\mathrm{D}/k_2 = 100$. This finding will provide insight into the OMAR mechanism. Although in this present approach, the observed MC effect is very small (a few percent), this is attributed to the small value of k_D/k_2. Furthermore, such a large MC effect can be simulated due to the TD pair mechanism and therefore, the origin of the OMAR may be a “trion” species.

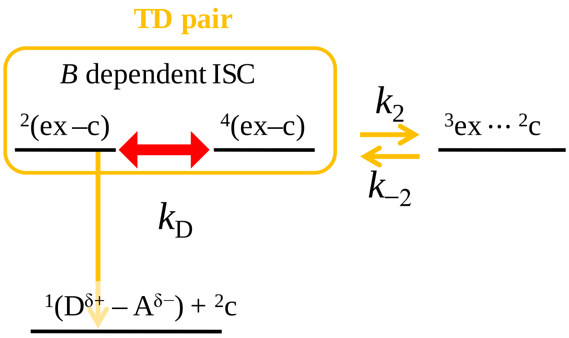

Scheme 3-3. The general scheme of the TD pair mechanism generating the MC effect observed in the photocurrent.

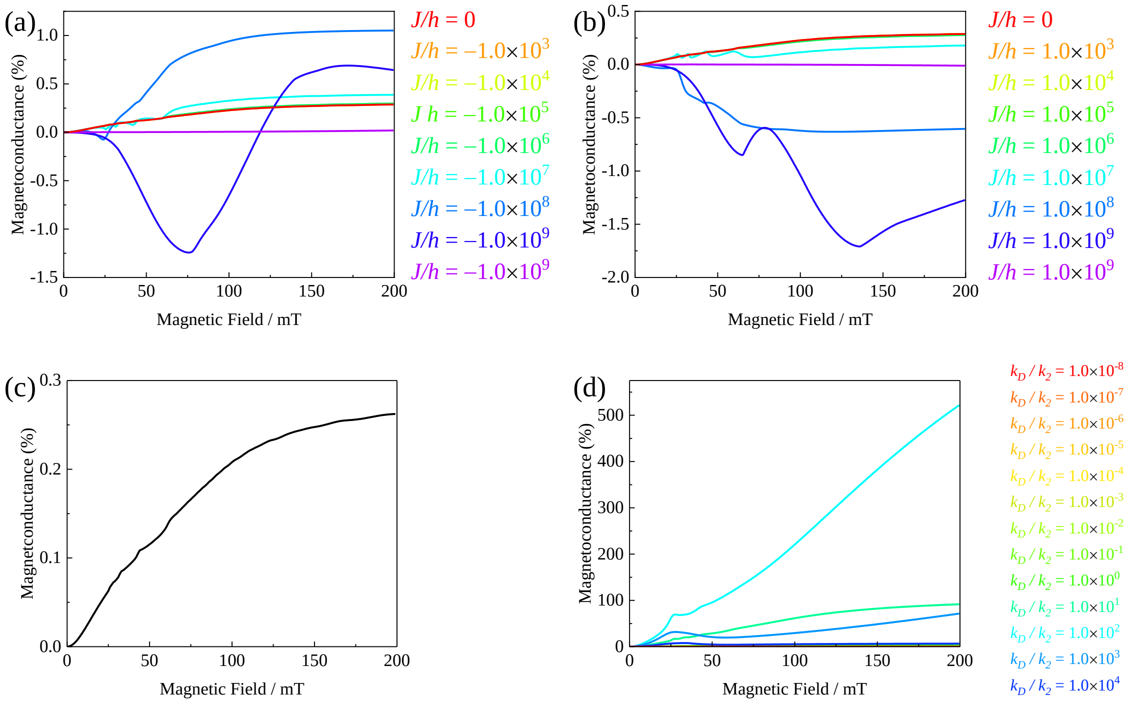

Fig. 3-13. Simulation of the TD pair mechanism. The following parameters were used in all the simulations: $g_T = 2.0050$, $g_D = 2.0023$, $|D| = 0.0830\ \mathrm{cm}^{-1}$, $|E| = 0.0160\ \mathrm{cm}^{-1}$ $P\mathrm{x} = 0.00$, $P\mathrm{y} = 0.92$, $P\mathrm{z} = 0.08$, and $k_2 = k_{-2}$. (a) and (b) The J dependence of the MC curves ($k_2 = k_{-2} = 1.0 \times 10^8\ \mathrm{s}^{-1}$ and $k_\mathrm{D} = 2.0 \times 10^8\ \mathrm{s}^{-1}$). (c) The k_2 dependence of the MC curves ($k_2 = k_{-2}$, $k_\mathrm{D} = 2.0 \times 10^8\ \mathrm{s}^{-1}$ and $J = 0\ \mathrm{cm}^{-1}$). (d) The k_D dependence of the MC curves. Inset is a logarithm scale for the vertical axis ($k_2 = k_{-2} = 1.0 \times 10^8\ \mathrm{s}^{-1}$, and $J = 0\ \mathrm{cm}^{-1}$).

3-6-3. Simulation of the Magnetoconductance on Py/DMPI VVD film

In the actual MC effect measurements, the lowest magnetic field was 3 mT because of the residual magnetisation of the iron core magnet used in the experiment. Therefore, $\langle \emptyset_{\mathrm{DD}}\,(3\ \mathrm{mT})\rangle$ was used in the simulation instead of $\langle \emptyset_{\mathrm{DD}}\,(0)\rangle$ as follows:

$$MC_{\mathrm{DD}} = \frac{\langle \emptyset_{\mathrm{DD}}(B)\rangle - \langle \emptyset_{\mathrm{DD}}(3\ \mathrm{mT})\rangle}{\langle \emptyset_{\mathrm{DD}}(3\ \mathrm{mT})\rangle} \times 100\,, \tag{3.32}$$

$$MC_{\mathrm{TD}} = \frac{\langle \emptyset_{\mathrm{TD}}(B)\rangle - \langle \emptyset_{\mathrm{TD}}(3\ \mathrm{mT})\rangle}{\langle \emptyset_{\mathrm{TD}}(3\ \mathrm{mT})\rangle} \times 100\,. \tag{3.33}$$

The observed MC behaviour was successfully reproduced as shown in **Fig. 3-14** (red solid curve) by solving the formula numerically. The red solid curve was obtained by the sum of the blue, green, and purple solid curves, where the blue curve is calculated using the DD pair mechanism; and green and purple curves obtained using the TD pair mechanism, respectively.

The low-field component (blue curves in **Fig. 3-14**) is reasonably described using the DD pair mechanism, that is the B-dependent ISC induced by the hyperfine coupling mechanism. In the DD pair mechanism, the Δg component can be neglected in the field range of the present study because of the small difference in the g values between the weak acceptor (DMPI anion) and donor (pyrene cation). The simulation reproduces the observed positive MC effects when the rate constants are chosen to be $k_1 = k_{-1} = k_{\mathrm{S}} = 1.0 \times 10^8\ \mathrm{s}^{-1}$ and $k_{\mathrm{T}} = 1.7 \times 10^8\ \mathrm{s}^{-1}$. Although there is some ambiguity in the choice of the rate constants because the experimental values are unclear, the relative ratio is meaningful because the shape of the simulation curve and the sign of the MC effect also depends on the relative ratio. The positive MC effect on the photocurrent in the low-field region is obtained when the kinetic constant of the triplet channel (k_{T}) is faster than that of the singlet channel (k_{S}), as shown in **Scheme 3-2.** The energy of the triplet excited state of pyrene (~2.1 eV) or the triplet CT exciton of pyrene/DMPI is located lower than that of the singlet charge-separated state, which can be estimated to be ~2.3 eV from the edge of the CT band. According to the energy gap law, [67, 68] the triplet channel (k_{T}) is faster than the singlet channel (k_{S}), which is reasonable because both channels are spin-allowed and the DD pair is located more closely to the triplet excited state (^{3}(D*–A)) than the singlet ground state (^{1}(D$^{\delta+}$–A$^{\delta-}$)).

In the TD pair mechanism, two patterns are expected: 1) Collisions between mobile triplet excitons (^{3}ex) and trapped carriers (^{2}c$_t$) and 2) collisions between trapped triplet excitons (^{3}ex$_t$) and mobile carriers (^{2}c). The former case leads to an increase in the mobile carrier as a result of detrapping upon collision (carrier detrapping). However, this carrier trapping leads to a negative MC effect on the photocurrent since the ISC due to the fine structure (not the Δ*g* mechanism) between ^{2}(ex–c) and ^{4}(ex–c) during the collision is depressed by the external magnetic field. Therefore, this is not consistent with the experimental results. The observed positive MC effect is expected in the collision between ^{3}ex$_t$ and ^{2}c (carrier trapping upon collision). The positive MC behaviour shows that the major trapped species are ^{3}ex$_t$ in the Py/DMPI VVD film. A positive MC effect in the photocurrent was also observed in the case of a pentacene/C_{60} bilayer solar cell, which indicates the major trapped species after photo-injection. Thus, it is expected that a large amount of ^{3}ex$_t$ is trapped in the VVD film as a result of the morphology (randomness) of the sample, although the mobile triplet exciton was observed in the single (or poly) crystal experiment. This prediction is proven by the temperature dependence of the TRESR shown in the next chapter. In the simulation of the purple solid curve in the TD pair mechanism, the *g*, *D*, and *E* values are $g_T = 2.0050$, $|D| = 0.0830$ cm^{-1}, and $|E| = 0.0160$ cm^{-1}, respectively, which are determined using the TRESR of Py/DMPI. Dynamic electron polarisation is also introduced to (Px = 0.00, Py = 0.92, and Pz = 0.08). The simulation reproduces the observed positive MC effects when the rate constants are chosen to be $k_2 = k_{-2} = 1.0 \times 10^8$ s^{-1} and $k_D = 2.0 \times 10^7$ s^{-1}. The purple simulation curve using the data determined from the TRESR experiment of Py/DMPI reproduces the MC effects observed in the high-field region (> 50 mT), which corresponds to one of the triple Gaussian components shown in **Fig. 3-8d** (purple one).

The green curve, which is one of the triple Gaussian components (middle component), can be explained by assuming the TD pair mechanism via detrapping upon collision between the trapped charge-separated triplet state and doublet carrier

(^{3}cs$_t$-^{2}e) pair. The triplet species observed using the TRESR of Py/PMDA may come from the triplet charge-separated electron-hole pair. The trapped charge-separated state with a similar magnitude to the D value is also expected in the VVD film of Py/DMPI because the distances between the donor and acceptor in Py/DMPI and Py/PMDA are similar. Although such a triplet species was not detected in the Py/DMPI polycrystalline samples using TRESR (see **Fig. 3-6**), the stronger TRESR signals arising from the triplet exciton can mask the weak spectrum of the triplet species. In the simulation of the green solid curve in the TD pair mechanism, the g, D, and E values are $g_T = 2.0040$, $|D| = 0.0141$ cm^{-1}, and $|E| = 0.0$ cm^{-1}, respectively and determined using the TRESR of Py/PMDA. Dynamic electron polarization is also considered (Px = 1.00, Py = 0.0, and Pz = 0.0). The simulation reproduces the observed positive MC effects when the rate constants are chosen to be $k_2 = k_{-2} = 1.0 \times 10^8$ s^{-1} and $k_D = 2.9 \times 10^7$ s^{-1}. This MC curve obtained using the TD pair mechanism from the ^{3}cs$_t$-^{2}e pair with the data determined by TRESR of Py/PMDA resembles the green curve, which is one of the triple Gaussian function components.

The red curve is the sum of the blue curve obtained using the DD pair mechanism and the purple and green curves obtained using the TD pair mechanism. This reproduces the observed MC effect. All parameters, except for the rate constant, were obtained from experiments and calculations. There is some ambiguity in the rate constants. However, the relative ratio of the rate constants is meaningful because it also depends on the shape of the simulation curve and the sign of the MC effect.

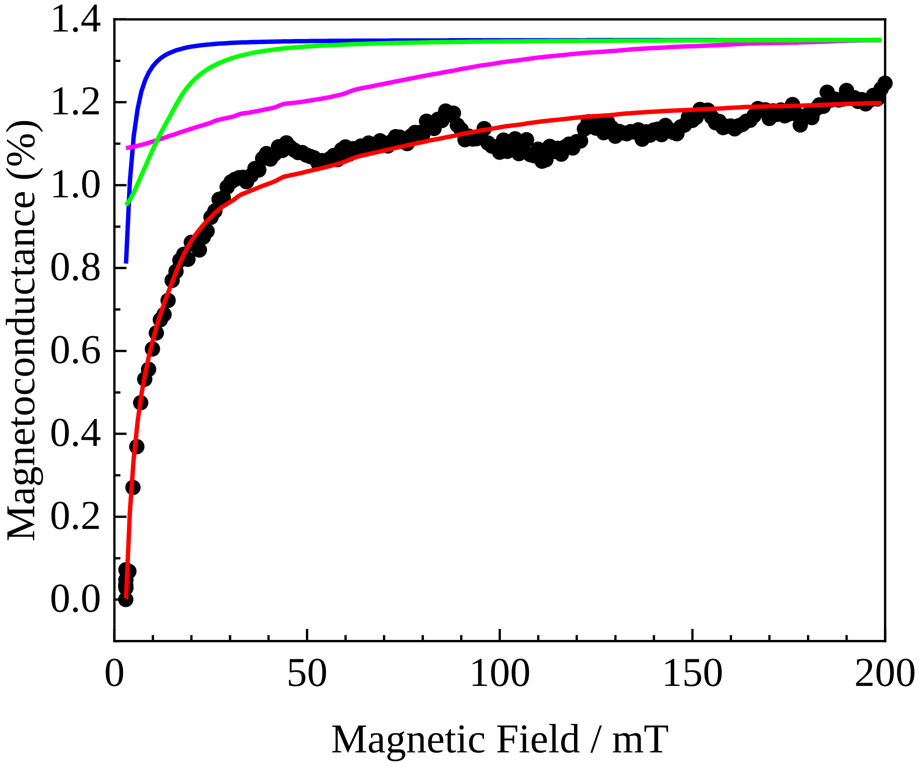

Fig. 3-14. Model calculation of the MC effects. The blue solid curve was obtained using the DD pair mechanism (g_{D1} = 2.0030, g_{D2} = 2.0030, D = −0.00782 cm^{-1}, E = 0.0 cm^{-1}, $\boldsymbol{a_{D1}^{eff}}$ = −30.0 MHz, $\boldsymbol{a_{D2}^{eff}}$ = −8.0 MHz, J = 0 cm^{-1}, $k_1 = k_{-1}$ = 1.0 × 10^8 s^{-1}, k_S = 1.0 × 10^8 s^{-1}, and k_T = 1.7 × 10^8 s^{-1}). The green (g_T = 2.0040, g_D = 2.0023, |D| = 0.0141 cm^{-1}, |E| = 0.0 cm^{-1} Px = 1.00, Py = 0.0, Pz = 0.0, $k_2 = k_{-2}$ = 1.0 × 10^8 s^{-1}, k_D = 2.9 × 10^7 s^{-1}, and J = 0 cm^{-1}) and purple (g_T = 2.0050, g_D = 2.0023, |D| = 0.0830 cm^{-1}, |E| = 0.0160 cm^{-1} Px = 0.00, Py = 0.92, Pz = 0.08, $k_2 = k_{-2}$ = 1.0 × 10^8 s^{-1}, k_D = 2.0 × 10^7 s^{-1},and J = 0 cm^{-1}) curves were simulated using the TD pair mechanism.

3-7. Summary

The CT character was investigated using the diffuse reflection and emission spectra, MO calculations, and TRESR measurements of two weak CT complexes (Py/DMPI and Py/PMDA). Triplet exciton and charge-separated triplet states were detected in Py/DMPI and Py/PMDA, respectively. The photocurrent and the MC effect were measured in the VVD films of Py/DMPI and Py/PMDA. The MC effect showed an increase of ~1.2% at 200 mT in the VVD films. The MC curve was approximately reproduced using a triple Gaussian fit. The MC behaviour was reasonably explained by assuming two types of collision mechanisms (DD and TD pair mechanisms), which occur between the geminate electron–hole pair (^{2}e–^{2}h) and between the trapped triplet species and carrier (^{3}ex$_t$–^{2}c or ^{3}cs$_t$–^{2}c). In the DD pair mechanism, the spin-spin interaction and the effective hyperfine coupling interaction were estimated from the second closest site and a molecular-orbital calculation of Py$^+$ and DMPI$^-$, respectively. In the TD pair mechanism, the spin–spin interaction was determined using the TRESR spectra. In the simulation of the DD pair mechanism, the MC effect is estimated to be < 3%, whereas in the simulation of the TD pair mechanism, the MC effect is estimated to be > 500% depending on the conditions. The MC effect was well reproduced using the DD pair mechanism and two types of TD pair mechanisms, such as trapped triplet exciton-carrier pair (^{3}ex$_t$–^{2}c) and trapped charge-separated triplet state-carrier pair (^{3}cs$_t$–^{2}c).

In addition, a very large MC effect can only be expected in the TD pair mechanism when k_D/k_2 ~100. This finding may provide some insight into the origin and mechanism of the OMAR phenomenon.

Chapter 4.

Temperature Dependence of Advanced ESR and Photocurrent Measurements of Weak Charge Transfer Complexes

4-1. Introduction

In **Chapter 3**, the absorption and emission spectra, and TRESR of weak CT complexes were discussed. Their CT characteristics were evaluated and the carrier dynamics in their VVD films were analysed from the MC effects observed in the photocurrent and quantum mechanical simulations. In the simulation based on the DD pair mechanism, weakly interacting e–h pairs were assumed, and in the simulation based on the TD pair mechanism, trapped triplet excitons were also assumed. In this chapter, the temperature dependence of the advanced ESR and photocurrent measurements were investigated on Py/DMPI to clarify the detailed carrier dynamics. The TRESR was first measured using a single crystal of Py/DMPI and the motional properties of the triplet exciton was examined on the basis of the spectra. The depth of the trap for the triplet exciton was estimated from the temperature dependence of the TRESR. The activation energy for carrier generation from the excited state was estimated from the temperature variation of the photocurrent. Finally, the direct detection of the e–h pairs was carried out using EDMR measurements and their temperature variation measurements were performed.

4-2. Temperature Dependence of the Single Crystal TRESR of Py/DMPI

The TRESR spectra of single crystals of Py/DMPI are shown in **Fig. 4-1**. Single-crystal ESR spectra have anisotropic, but the angle dependence is not measured in this study. In the single crystals, two sharp signals were observed. They were attributed to the following transitions: $|M_S = 0\rangle \leftrightarrow |M_S = -1\rangle$ and $|M_S = 0\rangle \leftrightarrow |M_S = +1\rangle$ in the triplet state, respectively. In order to evaluate the motility of the observed triplet excited states, the line shape of the transitions in the high field region was carefully examined. For the line shape analysis of the TRESR spectra, the Gaussian (**Eqn. 4.1**) and Lorentzian (**Eqn. 4.2**) functions were used for the least squares fitting.

$$g(B) = \frac{1}{\pi}\frac{1}{\Delta B_{1/2}}\exp\frac{1}{\pi}\left(\frac{1}{\Delta B_{1/2}}\right)^2 (B - B_0)^2 \tag{4.1}$$

$$g(B) = \frac{1}{\pi}\frac{1}{\Delta B_{1/2}}\frac{1}{1 + \left(1/\Delta B_{1/2}\right)^2 (B - B_0)^2} \tag{4.2}$$

where $\Delta B_{1/2}$ and B_0 are half width at half maximum and centre magnetic field, respectively. **Figure 4-1** shows the observed TRESR spectra (black), which are well fitted using the Lorentzian (blue) than the Gaussian (magenta). If the ESR transitions were only influenced by the uniform surrounding environment, the line shape is expected to be a Lorentzian and its linewidth is dominated by the Heisenberg uncertainty principle. Since the species (unpaired electron, hole, triplet state, etc.) are localized in condensed matter, they are exposed to inhomogeneous interactions from the local field, which broadens the linewidth and leads to a Gaussian line shape (inhomogeneous broadening). However, if the species with unpaired electrons move fast in the condensed matter, the interactions between the unpaired spins and their surroundings are averaged. As a result, their linewidth is reduced and the line shape is restored to a Lorentzian (motional narrowing).[69, 70] Therefore, the ESR spectra sharpened by motional narrowing allows one to estimate the lower limit of the lifetime (τ). The lower limit of lifetime of the mobile triplet exciton can be estimated from the relation of $\Delta B \sim h/g\beta\tau$. From the full width at half maximum of the obtained spectra, $\Delta B \sim 0.3$ mT, the lifetime of the triplet exciton was estimated to be $\tau = 2 \times 10^{-8}$ s.

The observed TRESR spectra are attributed to the mobile triplet species released thermally from the trap. The signal intensity decreases significantly with decreasing temperature. This was attributed to the capture of triplet excitons in the trap level at low temperature. Thus, the captured exciton is expected to have a much broader linewidth with a very low peak height as a result of inhomogeneous broadening, leading to the relatively negligible contribution in the resonance field of the mobile exciton. Using the temperature dependence of the signal intensity obtained from single crystal TRESR, the activation energy ($\Delta E/k_B$) of the trap level was estimated using the Arrhenius equation as follows:

$$I(T) = A \exp\frac{\Delta E}{k_B T} + I_0 \,. \tag{4.3}$$

Figure 4-2 shows the temperature dependence of the TRESR intensity of the single crystal of Py/DMPI, and **Fig. 4-3** shows the temperature variation of the TRESR spectra together with their Lorentzian fitting at each temperature. The trap depth was determined to be $\Delta E_{\mathrm{trap}}/k_B = +921 \pm 128$ K by least-squares fitting using **Eqn. 4.3**. This trap depth was much larger than that at room temperature (~300 K), indicating that many triplet excitons were captured in the trap levels even at room temperature. Although the observed data do not follow the single exponential Arrhenius equation well, suggesting the existence of multiple trapped sites with different depths, the trapping of the triplet exciton ($^3\mathrm{ex}_t$) was confirmed by their temperature variation measurements, which were assumed in the simulation using the TD pair mechanism.

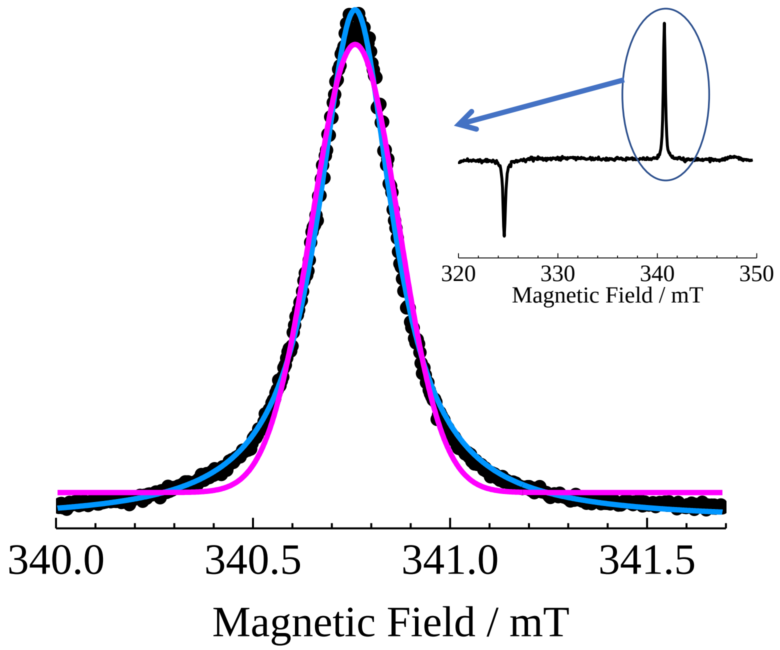

Fig. 4-1. TRESR spectra (black) and their Lorentz (blue) and Gaussian (magenda) fitting at room temperature. The microwave frequency and power are 9.44325 GHz and 1.00 mW, respectively.

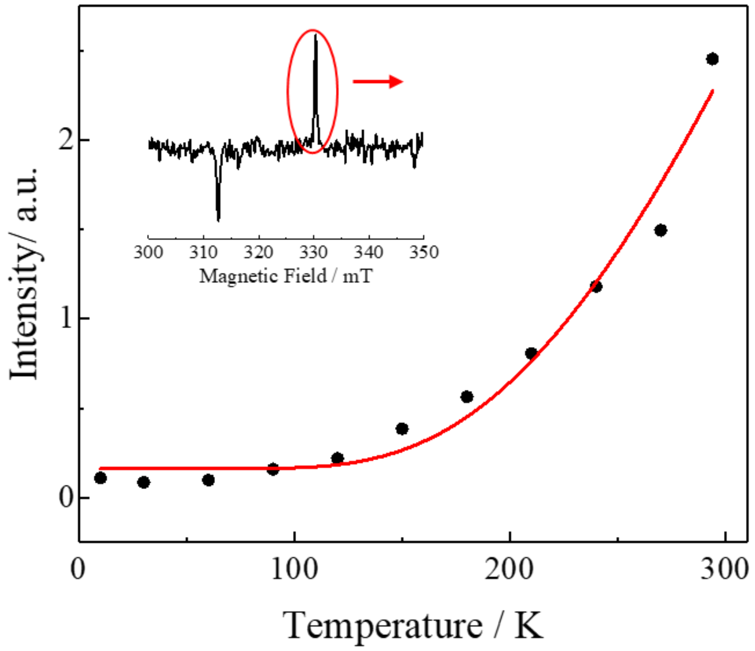

Fig. 4-2. The temperature dependence of the TRESR intensity (black) and fitting curve using **Eqn. 4.3** (red) obtained for the Py/DMPI single crystal. The microwave frequency and power were 9.13600 GHz and 1.00 mW, respectively.

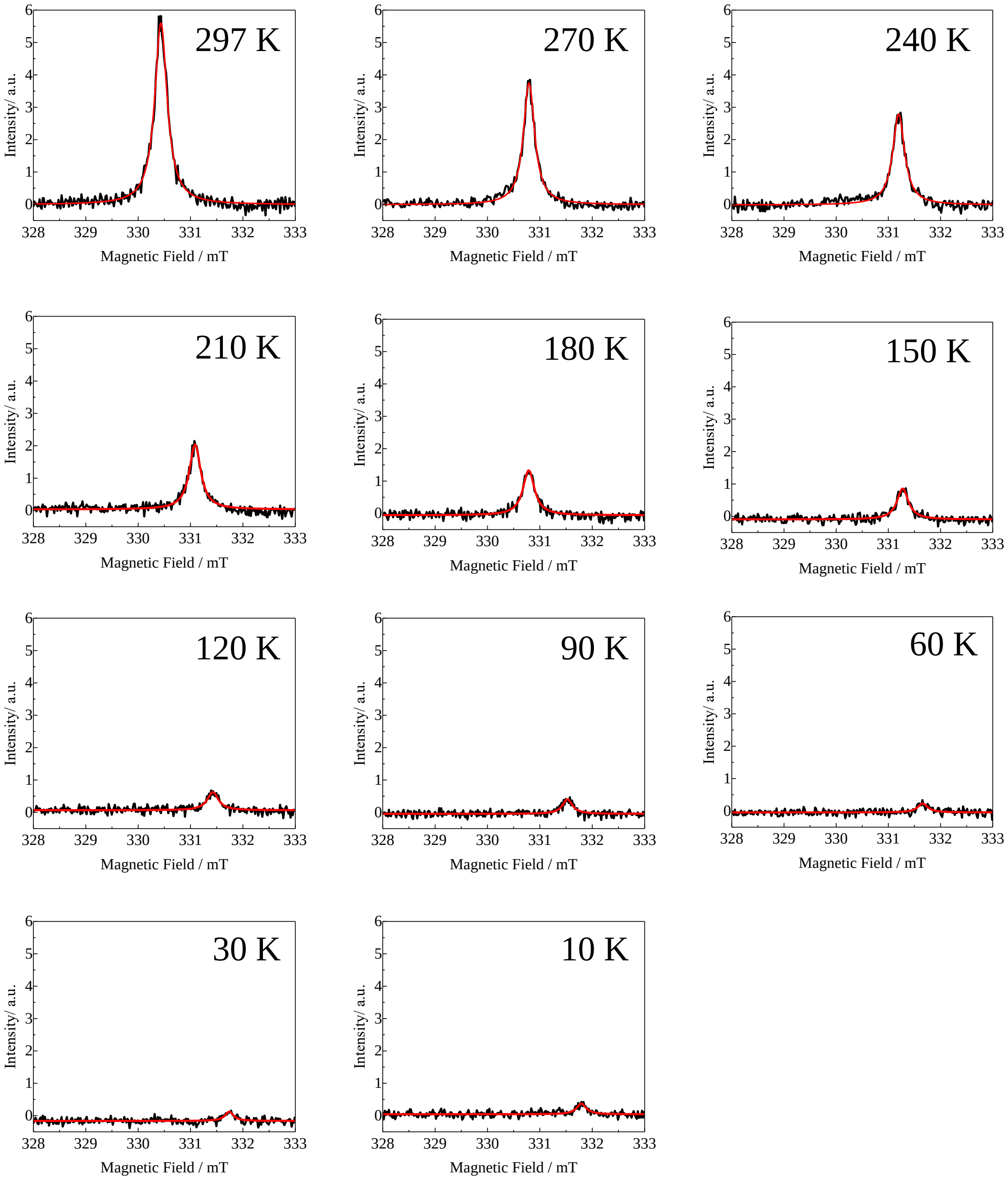

Fig. 4-3. The temperature variation of the TRESR spectra (black) obtained for the Py/DMPI single crystal at each temperature and their Lorentzian fitting (red).

4-3. Temperature Dependence of the Photocurrent of Py/DMPI VVD film

Fig. 4-4a and **4-4c** show the temperature variations of the photocurrent response to light irradiation. These on/off response behaviours at room temperature are similar to those described previously. However, photocurrent intensity was two orders of magnitude smaller than the absolute value. The commercially available interdigitated electrodes used in **Chapter 3** are based on glass substrates. On the other hand, custom-made interdigitated electrodes based on quartz substrates were used in this experiment. The electrical resistivity of the glass substrate was 10^{12}–10^{14} Ω cm and that of the quartz substrate was ~10^{18} Ω cm.[71] The photoconduction measurements using glass substrate electrodes show that the generated carriers conduct through the glass substrate when the mobility of the organic semiconductor is very low. Therefore, the photocurrent behaviour observed in the present experiments was likely to be close to intrinsic to the Py/DMPI film. The MC ratio was expected to be less influenced by the difference in the substrate because the ratio was only determined by the carrier generation process. The magnitude of the photocurrent decreased at lower temperature, but the photocurrent response was independent of the temperature and applied voltage.

Figures 4-4b and **4-4d** show the temperature dependence of the photocurrent intensity. The activation energies were determined using least-squares fit with the **Eqn. 4.3** to be $\Delta E/k_\mathrm{B} = +1692 \pm 41$ K under 10 V applied bias; and +1507 ±126 K under 1.5 V applied bias, respectively. Almost no difference in the activation energy with the applied voltage bias was observed. The magnitude of the activation energy (ΔE) was comparable to that observed in the single crystal measurement of an anthracene/PMDA CT complex (0.14 eV, 1.6×10^3 K).[72] The observation of the MC effect on the photoconductivity of the Py/DMPI VVD film indicates the formation of intermediate pairs of paramagnetic particles (such as the e–h pair and ex–c pair), as described in the previous chapter. Upon photo-excitation, the singlet CT state $^1(\mathrm{D}^+\text{–}\mathrm{A}^-)$ was initially generated. An electron or hole can migrate to a neighbouring (preferably, next-neighbour) donor or acceptor molecule, forming a geminate e–h pair. Charge carriers are generated upon dissociation of the e–h pair, in which singlet and triplet states are generated with the same probability independent of their spin state [^{1}(e–h) or ^{3}(e–h)]. Since the generation of the mobile carrier from the excited CT state (D^+–A^-) is a multi-step process, the effective activation energy obtained by photocurrent measurements is the sum of the activation energies of each process. This temperature dependence may include not only the activation energy due to the generation of the carrier from the excited state, but also the thermal detrapping process of the carrier.

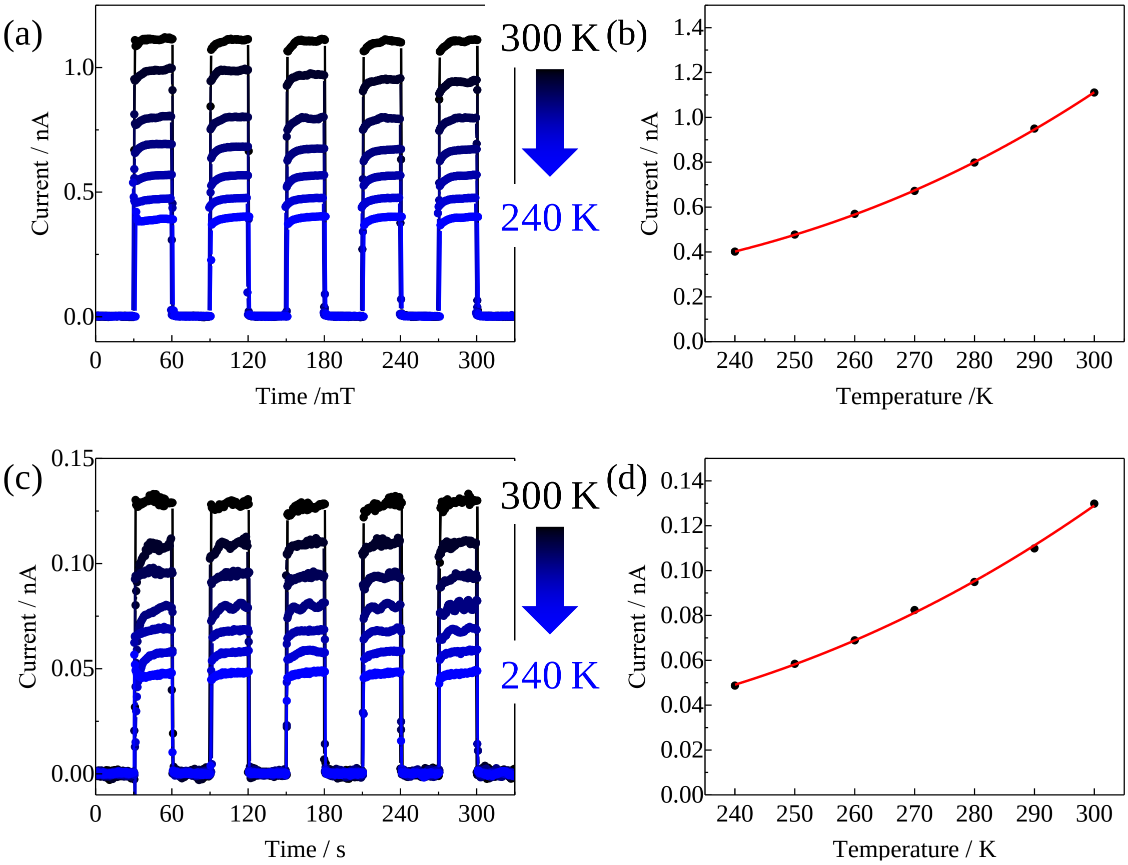

Fig. 4-4. The temperature variation of the photocurrent response under an applied bias of (a) 10 V and (c) 1.5 V. The temperature dependence of the photocurrent intensity (black) and fitting curve using **Eqn. 4.3** (red) under an applied bias of (b) 10 V and (d) 1.5 V.

4-4. Temperature Dependence of the EDMR of Py/DMPI VVD film

Figure 4-5 shows the EDMR spectra obtained at various temperatures upon monitoring the photocurrent of the Py/DMPI VVD film under microwave irradiation at 101 mW. EDMR measures the change in the current induced by the ESR transitions. Although free electrons with an S = 1/2 spin state can cause ESR transitions, the transitions do not induce any change in the carrier density and carrier mobility. Therefore, the current intensity does not change, leading to no EDMR signal. Under a magnetic field (B ~325 mT), S-T_0 mixing occurs in the e–h pair generated via photoexcitation due to the B-dependent ISC between the singlet and triplet states of the e–h pair. When the ESR transition occurs between the spin sub-levels of the ^{3}(e–h) pair, the population of T_0 is transferred to T_+ and T_- or vice versa. When the rate constant for the transition from the ^{3}(e–h) pair to the triplet excited state, ^{3}(D*–A), differs from that for the transition from the ^{1}(e–h) pair to the ground state, $^1(D^{\delta+}–A^{\delta-})$, the ESR transition changes the carrier generation efficiency. The paramagnetic pairs that cause EDMR are not only e–h pairs, but also trions consisting of triplet excitons and carriers (^{3}ex–^{2}c). In fact, there are some reports that the EDMR signal of OLEDs is due to the trion.[73] The EDMR signals from trion splitting were over a wide range of magnetic fields due to the fine structural interaction of triplet excitons and half-field signal of Δm_s = 2 were also observed. In OLEDs using poly[9,9-dioctylfluorenyl-2,7-diyl] (PFO) and poly[2-methox-5-(2-ethyl-hexyloxy)-1,4-phenylenevinylene] (MEH-PPV) as the luminescent layer, the half-field (Δm_s = 2) signal was not observed at room temperature, but observed at low temperature (10 K).[74, 75] However, the EDMR spectrum of the Py/DMPI VVD film can be understood to originate from a weakly interacting e–h pair signal, since it is a single-line signal without any fine structure splitting at the central magnetic field of g = 2.0034. The EDMR spectra were analysed using least-squares fit to the Lorentzian function (**Eqn. 4.2**), which indicates that the e–h pair is one of the mobile species, and the lifetime (τ) was estimated to be $\tau = 4.0 \times 10^{-9}$ s from the linewidth (ΔB = 1.4 mT).

The temperature dependence of the signal intensity was well fitted using the **Eqn. 4.3**. The activation energy was estimated to be $\Delta E/k_B$ = +2688 ± 294 K using least-squares fitting. ΔE corresponds to the energy difference between the e–h pairs and the mobile carrier. However, the magnitude estimated from EDMR may be overestimated because the EDMR signal intensity decreases due to the spin-lattice relaxation effects observed with an increase in temperature. In the present experiment, it was failed to direct time-resolved detection using pulse LASER excitation without using the phase-sensitive detection method. Therefore, the relationship between k_T and k_S could not be determined in this VVD film.

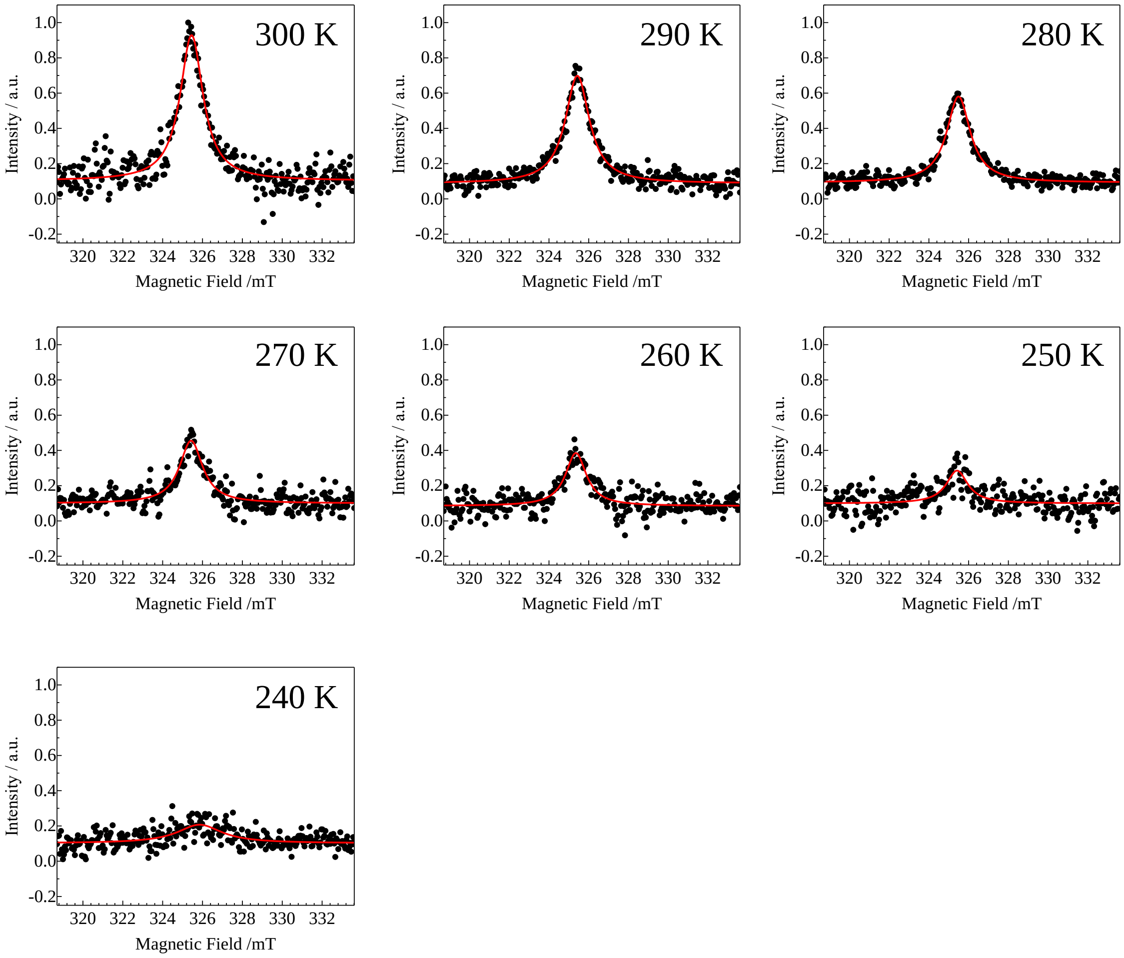

Fig. 4-5. The temperature variation of the TRESR spectra (black) observed for the Py/DMPI film at each temperature and their Lorentzian fitting (red).

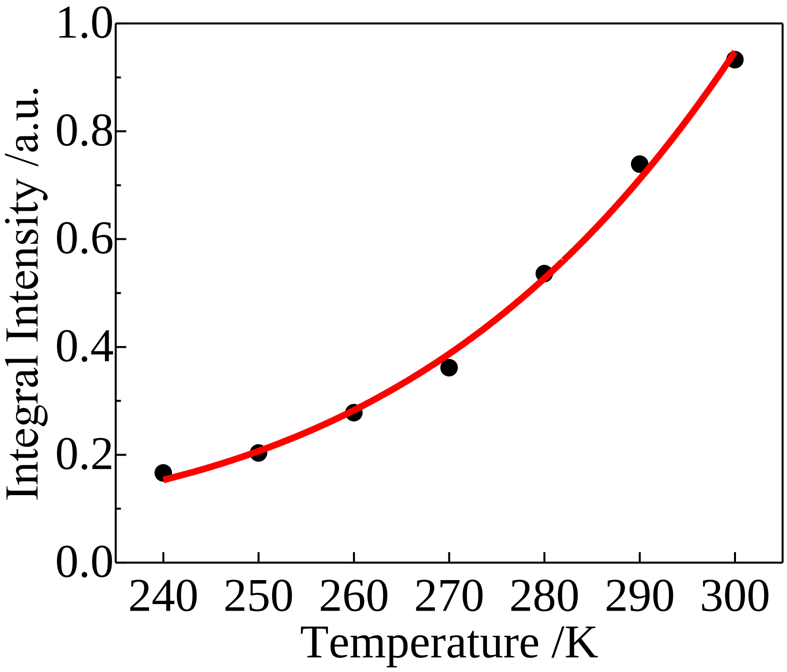

Fig. 4-6. The temperature dependence of the TRESR intensity (black) and fitting curve using **Eqn. 4.3** (red) observed for the Py/DMPI single crystal.

4-5. Summary

The temperature dependence of the TRESR, photocurrent, and photocurrent detected EDMR of Py/DMPI have been studied. The TRESR was measured using a single crystal of Py/DMPI. It was clarified from the line shape analysis that the observed single crystal TRESR signals are due to a mobile triplet exciton. The trap depth of the triplet excitons was determined to be $\Delta E_{\mathrm{trap}}/k_{\mathrm{B}}$ = +921 ±128 K from the temperature dependence of the TRESR signal intensity, indicating that many triplet excitons were trapped in the trap levels even at room temperature.

By measuring the temperature variation of the photocurrent of the VVD film, the activation energies for carrier generation from the excited state was determined to be $\Delta E/k_{\mathrm{B}}$ = +1692 ±41 K at 10 V applied bias and +1507 ±126 K at 1.5 V applied bias. There was no significant temperature dependence in the activation energy.

The e–h pairs were directly detected from the EDMR measurements of the Py/DMPI VVD film and temperature dependences were evaluated. The temperature dependence of EDMR was fitted well by using the formula assuming thermal activitation, and the activation energy was obtained as $\Delta E/k_{\mathrm{B}}$ = +2688 ±294 K. This value is expected with the activation energy of mobile carrier generation from the e-h pair. This magnitude was larger than the value estimated from the temperature dependence of the photocurrent. The difference may be due to the spin relaxation effect, which can lead to an overestimation of the EDMR measurements. In this experiment, the EDMR signal was small, allowing only a narrow temperature range to be measured. However, it is expected to give the understanding of the detailed physics of e–h pair that measuring the temperature dependence over a wider range. In the next chapter, the temperature dependence of EDMR is investigated in detail using TIPS-Pn thin film, which is possible to measure over a wide temperature range. The analysis of temperature dependence of EDMR behavior on Py/DMPI is described in **Appendix** using the model obtained in **Chapter 5**.

Chapter 5.

Photo-Carrier Dynamics of TIPS-Pentacene Film

5-1. Introduction

Organic semiconductors have attracted considerable attention because of their potential to produce large-area flexible substrates at low cost. The mobility is expected to be enhanced by extending π conjugation of polyacene. Actually, extended π-systems such as pentacene are known to have high hole mobility due to their large intermolecular overlap owing to π-π stacking in the solid state. Pentacene is a representative example of an organic semiconductor and its carrier mobility has been reported to exceed 2 cm^2 V^{-1} s^{-1} for thin films[76] and 50 cm^2 V^{-1} s^{-1} for single crystals.[77] Typical values in the mobility of OFET devices using anthracene and tetracene are 0.02 and 0.38 cm^2 V^{-1} s^{-1}, respectively.[78, 79] The mobility of pentacene corresponds to a degree of magnitude to amorphous silicon and a variety of applications is expected from the high mobility. [80, 81] During the research studies on pentacene devices, the OFET performance has been extensively evaluated, including the synthesis of new pentacene derivatives, device development, and measurement of device properties.

In addition to significant hole mobility, pentacene derivatives exhibit high electron donor properties. These materials have also gained increasing interest in singlet fission (SF).[82] The SF generates two triplet-excited states from one photon. Therefore, it is possible to exceed the theoretical Shockley–Queisser limit[83] of their power conversion efficiency. The SF in the pentacene derivative has the potential to lead to the realisation of highly efficient solar cells. The pentacene derivative is expected to be used as a donor layer in organic thin-film solar cells. Therefore, the photogenerated carrier dynamics in pentacene derivatives is an important research topic in materials science and photovoltaic device applications. However, pentacene has some disadvantages, such as being photochemically unstable under atmospheric oxygen and poor solubility in organic solvents. Significant efforts have been made to mitigate these disadvantages by modifying the electronic structure[84] or insertion of bulky substituents.[85] The 6,13-Bis-(triisopropylsilylethynyl)pentacene developed by Anthony *et al.*[48] exhibits high solubility and photo-stability,[86] and has been widely used in organic thin-film devices. Recently, a conceptually different photo-stabilization approach using enhanced intersystem crossing through the insertion of radical substituents was reported in our laboratory.[87, 88] In this method, the photostability of the product was enhanced by the unique excited-state dynamics (enhanced intersystem crossing) induced by radical substituents, which result in the extremely short lifetime observed for the reactive excited state.[89] This method successfully stabilizes the pentacene skeleton without significantly changing the electronic structure of the pentacene moiety.

The ESR spectroscopy has been used for a long time to determine the spin and electronic structure of the molecule (radical cation, radical anion, excited state, etc.). In recent years, spin measurements in condensed matter such as solids and thin films have attracted a great deal of attention for device applications. The ESR spectroscopy is particularly suitable in view of the direct observation of electric-field-induced charge carriers in organic semiconductors. Neutral organic semiconductors differ from classical inorganic semiconductors because the former typically has very few charge carriers (without applying an electrical field) due to negligible natural doping. A conventional ESR method successfully clarified the delocalised or mobile nature of the carriers in the pentacene film induced by an applied gate voltage in FET devices.[5, 90] The EDMR was also conducted to clarify the carrier dynamics of pentacene VVD films in a three-layered diode under a specific operating voltage range. Organic semiconductors are also of interest in the field of spintronics because of their longer spin relaxation times and the ability to transport spin over long distances when compared to inorganic semiconductors.[91] In TIPS-Pn VVD films, pure spin currents were transported in a similar manner to pentacene.[92–94] The spin current injected into pentacene from the ferromagnet is converted into voltage by the inverse spin Hall effect and measured as EDMR. Therefore, pentacene derivatives can be used for potential application in future organic spintronic devices. These studies focused on the ground-state properties in device applications. In the excited state, the quintet state and two separated triplet states generated by SF in the thin films of pentacene derivatives were observed using TRESR. The photocurrent observed on TIPS-Pn thin films is known to exhibit long-lived decay behaviour (persistent photocurrent) after termination of light irradiation.[95, 96] The dynamics of the photogenerated carriers in pentacene derivatives have become an important research subject in materials science and their application in photovoltaic devices, but the spin dynamics have not been clarified in some parts. In this study, the EDMR method was applied to investigate the nature of the intermediate e–h pairs possibly involved in the photogeneration of charge carriers in TIPS-Pn. Photocurrent measurements are important methods to study mechanisms, such as photogenerated carriers, photoemission, and photoconductance. In this chapter, the temperature dependence of the photocurrent and the photocurrent detected EDMR on TIPS-Pn VVD films were discussed. Their temperature dependence is analysed using quantum mechanical simulations along with analytical solutions to the conventional rate equations, assuming the carrier dynamics of the weakly coupled e–h pair.

5-2. Optical Spectra

TIPS-Pn is known to form a variety of crystalline polymorphs and amorphous forms in films and crystals. Aggregated molecules show different properties from those in solution and their electronic; and optical properties vary depending on the structure of the solid. **Figure 5-1** shows the UV–vis optical density spectra obtained for TIPS-Pn. The spectra obtained for the prepared VVD films and TIPS-Pn ground powder are similar to each other. In both spectra, a shoulder at ~700 nm was observed, which was assigned to π-π stacking of the pentacene moiety. Clear vibronic splitting patterns in the region of 500–700 nm due to the fundamental $S_0 \rightarrow S_1$ transition was observed in the organic solution.[86] It has been reported that the shoulder observed at ~700 nm does not appear in the amorphous film.[97, 98] Therefore, according to the literature, this VVD film is polycrystalline and not amorphous.

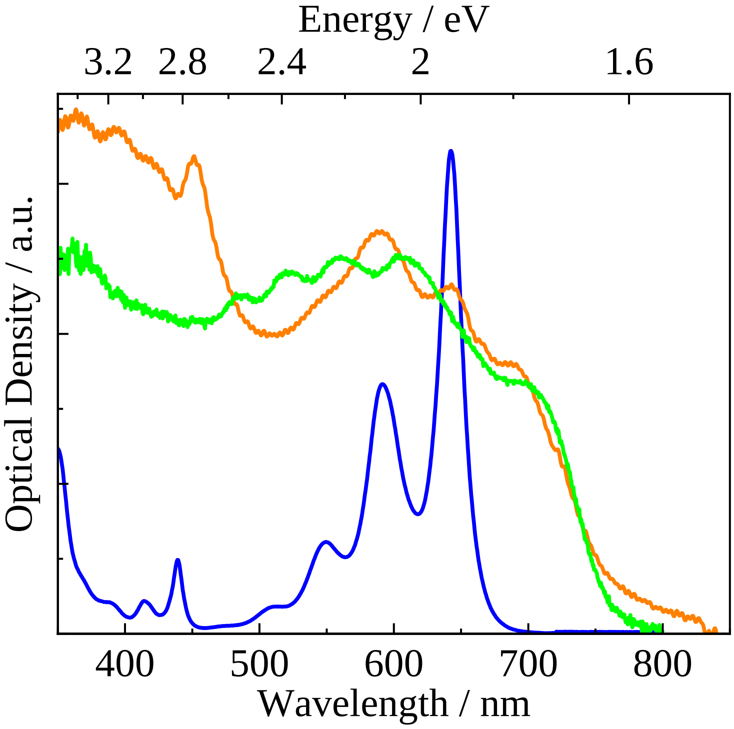

Fig. 5-1. UV–vis optical density spectrum of TIPS-Pn absorption in an CH_2Cl_2 solution (blue curve), transmission spectrum of the TIPS-Pn film (orange curve), and diffuse reflectance spectrum of the ground powder of the TIPS-Pn sample (green curve).

5-3. Model of the Carrier Generation

Two possible carrier generation mechanisms can be considered for the TIPS-Pn film. One is to generate the spin-singlet e–h pair from the singlet excited state immediately after excitation, and the carriers are generated from the spin singlet e–h pair (S-born model). The other model is that the spin triplet e–h pair is born from the T_0 level of the triplet excited state by the SF immediately after excitation, and the carriers are generated from the spin triplet e–h pair (T_0-born model). In these models, it is assumed that there is a thermally active barrier to dissociate mobile carriers of electrons and holes from electron-hole pairs to generate carriers. Therefore, the carrier generation rate (k_{dis}) is given as follows;

$$k_{\mathrm{dis}} = k_0 \exp(-E/k_{\mathrm{B}}T). \qquad (5.1)$$

The rate constant of S-T_0 mixing of e–h pair is defined as k_{ISC}. The rate constant of ESR transition between the sublevels of ^{3}(e–h) pair by microwave irradiation is defined as k_{ESR}. The rate constants of transition from the ^{1}(e–h) pair to the ground state (S_0) and from the ^{3}(e–h) pair to the excited triplet state (T_1) are defined as k_{S} and k_{T}, respectively. The S-born and T_0-born models are illustrated in **Schemes 5-1** and **5-2**, respectively. The free energy of e–h pair generation upon photoexcitation was roughly estimated using the Rehm–Weller equation (**Eqn. 5.2**).[99]

$$\Delta G = E(\mathrm{D/D^+}) - E(\mathrm{A^-/A}) - e^2/\varepsilon r - \Delta E_{00}\,. \qquad (5.2)$$

The first and second terms are the oxidation and reduction potentials of TIPS-Pn. The third term is the electrostatic Coulomb interaction energy of the e–h pair. The fourth term is the singlet excited-state energy. The redox potential of TIPS-Pn was determined to be 0.402 V (oxidation) and −1.45 V (reduction) vs. Fc/Fc$^+$ using cyclic voltammetry in a CH_2Cl_2 solution (**Fig. 5-2**). A rough estimation of the difference in the redox potential, $E(\mathrm{D/D^+}) - E(\mathrm{A^{-}/A})$, was made using these values because the corresponding values in the VVD films are unavailable. The relative dielectric constant of the TIPS-Pn film is reported to be $\varepsilon = 12.5$ at room temperature.[100] The intermolecular face-to-face distance was $r = 7.75$ Å, as determined using X-ray crystallography.[48] The excited singlet and triplet energies for TIPS-Pn in the solid state have been reported as 1.71 and 0.87 eV, respectively,[38] and the excited singlet energy for TIPS-Pn in the film was obtained at 1.79 eV (691 nm) using absorption spectroscopy. Using the obtained value, the free energy for the generation of ^{1}(e–h) from the singlet state were estimated to be negative ($\Delta G = -0.086$ eV). Therefore, their spontaneous generation is expected to occur. In this process, according to the spin selection rule, only ^{1}(e–h) is populated (**Scheme 5-1**). It is known from time-resolved ESR and pump-probe spectroscopy measurements that SF occurs in TIPS-Pn films.[82, 101] Therefore, a rapid spin-allowed generation of the triplet excited state from SF is possible in this system, leading to photocurrent generation from the triplet excited state (T_0-born model; **Scheme 5-2**). However, in contrast to the singlet e–h pair, the free energy for ^{3}(e–h) generation from the triplet state was estimated to be positive ($\Delta G = 0.728$ eV). Thus, triplet e–h pair generation cannot occur spontaneously, even in the thermal activation of the T_1 state of the TIPS-Pn, which is much higher than the room temperature thermal energy Therefore, the initial population in the e–h pair exists only as ^{1}(e–h), as shown in **Scheme 5-1**.

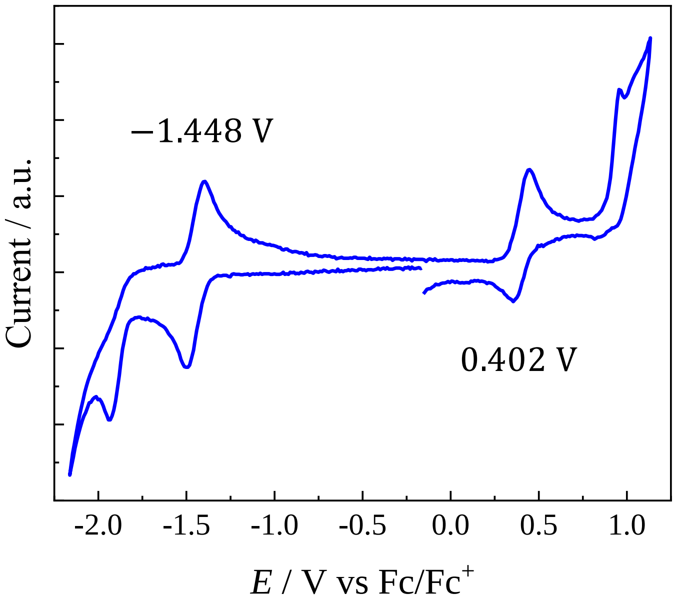

Fig. 5-2. Cyclic voltammogram of 1.0 mM TIPS-Pn in CH_2Cl_2 containing 0.1 M $TBAPF_6$ at room temperature.

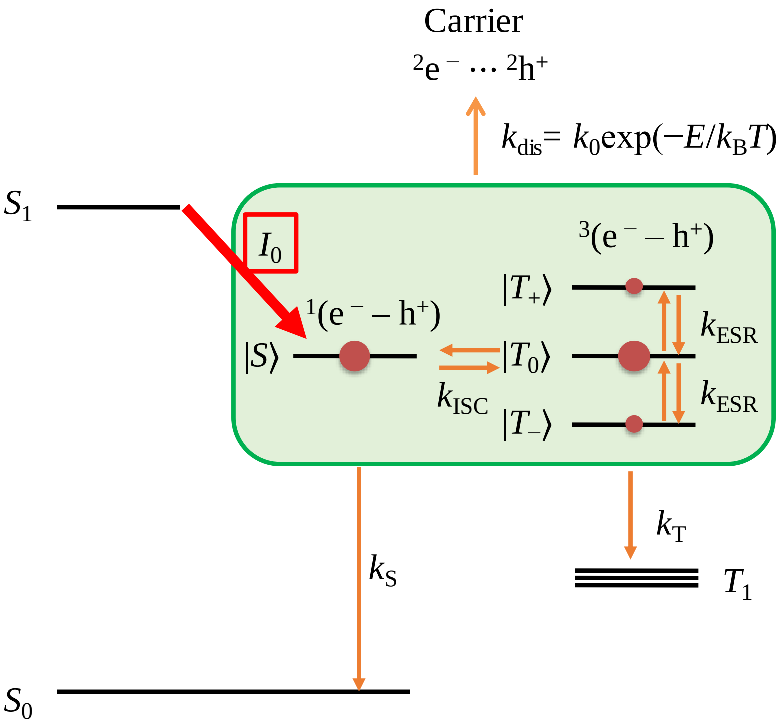

Scheme 5-1. The excited-state dynamics and carrier generation model in the VVD film of TIPS-Pn via singlet born process.

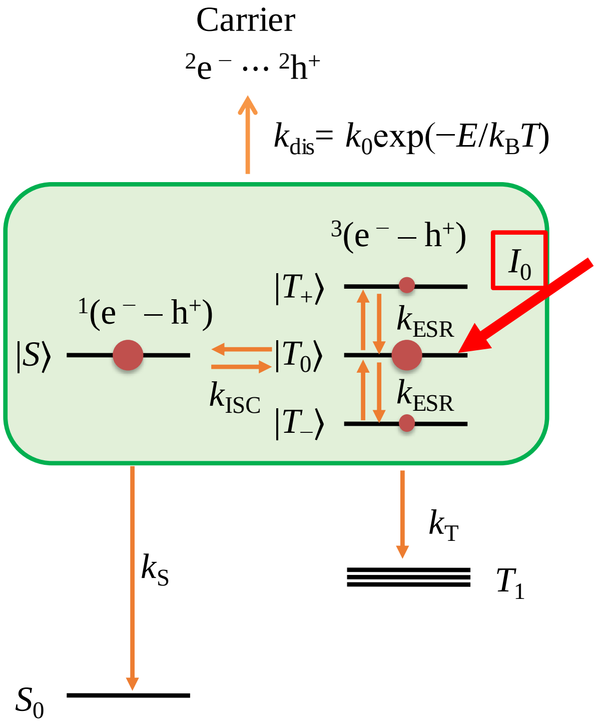

Scheme 5-2. The excited-state dynamics and carrier generation model in the VVD film of TIPS-Pn via triplet born process.

5-4. Photocurrent Behaviour

Defects may introduce trap levels in the band gap, which have a direct influence on the transport phenomena of charge carriers. By measuring the persistent photocurrent, we can confirm the presence of the traps based on their behaviour. Here, the effect of the atmospheric environment on the films was reported at room temperature. We measured the photocurrent and persistent photocurrent in the VVD films of TIPS-Pn. **Figure 5-2** shows the typical photocurrent behaviour of the TIPS-Pn VVD film excited using a white light Xe lamp at room temperature in the air as well as the N_2 atmosphere. Large light-induced conductivity during light illumination was observed both in air and the N_2 atmosphere. In contrast, a persistent photocurrent with long lifetime after termination of the radiation was clearly observed under the air atmosphere and a relatively smaller one was detected under the N_2 atmosphere. Similar persistent photocurrent behaviours are decomposed into two components with different lifetimes, which have been reported for some organic semiconductors.[96] The persistent photocurrent decay shown in the inset of **Fig. 5-2** was also fitted to a biexponential function, as follows:

$$I(t) = A_1 \exp\left(-\frac{t}{\tau_1}\right) + A_2 \exp\left(-\frac{t}{\tau_2}\right) + I_0 \, , \tag{5.3}$$

where τ_1 and τ_2 are the decay time constants and I_0 is offset. The lifetimes are determined to be τ_1 = 12 s (50%) and τ_2 = 132 s (50%) under air, and τ_1 = 6.1 s (68%) and τ_2 = 120 s (32%) in the N_2 atmosphere by least-squares fit using **Eqn. 5.3** for the current values after turning off the photo-irradiation (Light Off in **Fig. 5-3**). The percentage in the brackets of τ_1 and τ_2 were estimated by $A_1/(A_1+A_2)$ and $A_2/(A_1+A_2)$ using the amplitudes of their components, respectively. These results demonstrate the existence of multi-trap states in the present system. To explain the origin of the persistent photocurrent in TIPS-Pn, two mechanisms have been proposed in the literature.[95] [96] One is related to two specific defects that exist at the interface between the dielectric and organic semiconductor phases in the FET device. The other is related to degradation due to the incorporation of the ambient O_2 in air. Significant persistent photocurrents were observed in air, while little persistent photocurrent behaviour was observed in the N_2 atmosphere, as shown in **Fig. 5-2**. This indicates that the origin of the persistent photocurrent is the latter mechanism.

From the band calculations of unsubstituted pentacene crystals, it is known that the oxygen-bridged pentacene skeleton forms a trap level between the conduction and valence bands.[102] In TIPS-Pn, the trapping levels are also likely to be formed via the incorporation of oxygen.

From the measurement of the temperature variation of the photocurrent, it is possible to estimate the activation energy to produce the mobile carriers from the ^{1}(e–h) pairs shown in **Scheme 5-1**. The inset of **Fig. 5-3** shows the photocurrent behaviour at each temperature under the N_2 atmosphere. **Figure 5-4** shows the temperature dependence of the photocurrent intensity. The photocurrent intensity decreases with decreasing temperature. In these photocurrent measurements, the external magnetic field (B) and microwave were not applied. Therefore, field-induced intersystem crossing (S-T_0 mixing) originating from the Δg mechanism can be neglected ($k_{\mathrm{ISC}} = 0\ \mathrm{s}^{-1}$ and $k_{\mathrm{ESR}} = 0\ \mathrm{s}^{-1}$). The temperature dependence was well fitted by the analytical solution based on **Scheme 5-1** and **Eqn. 5.4** for the photocurrent (I_{off} and $k_{\mathrm{ESR}} = k_{\mathrm{ISC}} = 0\ \mathrm{s}^{-1}$), which is given by:

$$I_{off,B=0}(T) = \frac{I_0}{k_{\mathrm{S}} + k_{\mathrm{dis}}} k_{\mathrm{dis}}\ . \qquad (5.4)$$

Here, the activation energy, E/k_{B} in **Eqn. 5.1**, was introduced for carrier generation from the ^{1}(e–h) pair generated via photoexcitation. This process is dissociated the ^{1}(e–h) pairs into electrons and holes. The activation energy, E/k_{B}, was determined to be 1103 ±149 K using least-squares fitting with **Eqn. 5.4**. k_{S} and k_0 could not be determined from this fitting because they are temperature interdependent parameters.

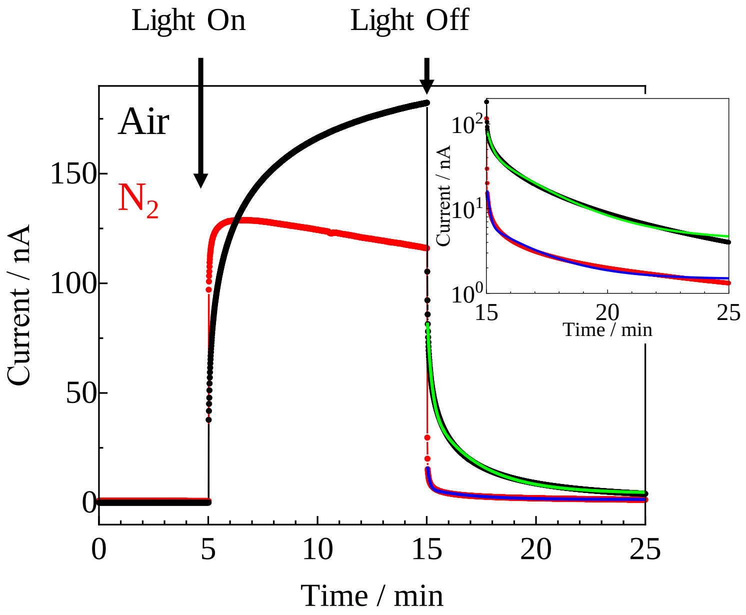

Fig. 5-3. The photocurrent and persistent photocurrent responses of the TIPS-Pn film for light illumination using a Xe lamp in air (black curve) and in the N_2 atmosphere (red curve) at room temperature. The inset is the decay of the persistent photocurrent depicted using a logarithm scale for the vertical axis.

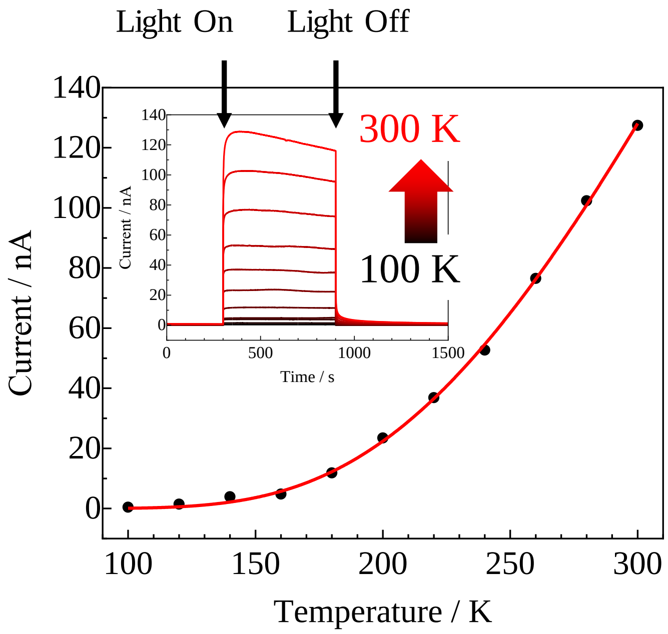

Fig. 5-4. The temperature dependence of the photocurrent intensity in the N_2 atmosphere. The inset is the photocurrent and persistent photocurrent responses of the TIPS-Pn film.

5-5. EDMR Behaviour

5-5-1. Direct Detection of EDMR at 200 K

The absolute sign of the current change in EDMR cannot be determined because the intensity and sign of the signal change with respect to the phase of the reference signal when the lock-in amplifier is used. Therefore, the absolute value and sign of the change in the photocurrent was measured using a picoammeter instead of using a lock-in amplifier. **Figure 5-5** shows the direct detection of the EDMR response for the photocurrent at 200 K using a picoammeter (photocurrent vs. external magnetic field plot). The photocurrent decreased by ~1.3 % under ESR conditions. Thus, the absolute sign of the photocurrent-detected EDMR signal was determined to be negative (decrease) for the photocurrent.

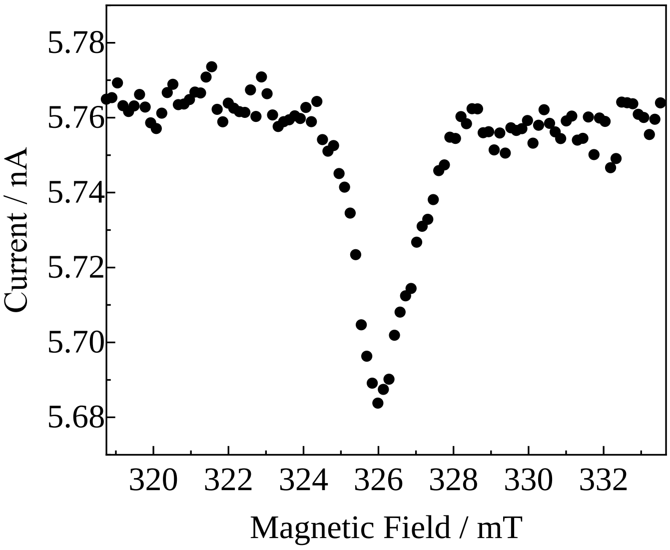

Fig. 5-5. Direct detection of the EDMR response for the photocurrent at 200 K using a picoammeter.

5-5-2. Environmental Dependence of the EDMR Spectra at Room Temperature

From persistent photocurrent measurements, it was shown that atmospheric oxygen reacts with TIPS-Pn to cause a persistent photocurrent. EDMR measurements were carried out for both the photocurrent and persistent photocurrent. **Figure 5-6** shows the EDMR spectra of TIPS-Pn obtained upon monitoring the photocurrent and persistent photocurrent at room temperature in air and the N_2 atmosphere, respectively. The opposite sign of the EDMR signals was detected in the *g* ~2 region for the photocurrent and persistent photocurrent. The EDMR signals of the photocurrent (photocurrent-detected EDMR) correspond to the decrease in the current. Because the same settings of the lock-in amplifier were used in both EDMR signals for the photocurrent and persistent photocurrent, the EDMR signals of the persistent photocurrent (persistent-current-detected EDMR) may correspond to the increase in the current. The photocurrent-detected EDMR signal observed under an N_2 atmosphere was similar to that under an air atmosphere. In contrast, the persistent photocurrent-detected EDMR gave a weak signal corresponding to the decrease in the persistent photocurrent. The observed persistent-photocurrent-detected EDMR spectra in N_2 atmosphere may originate from the persistent photocurrent formed due to the presence of the oxygen. It is known that atmospheric exposure increases EDMR signal in OLEDs on the dark condition.[41, 103] This means that the spin-dependent reactions between trapped electrons and free holes induced by the atmosphere are modulated by ESR, resulting in a change in the carrier density.[41, 103] The atmospheric dependence of EDMR on persistent photocurrent observed in the present experiment is expected to be caused by a similar mechanism.

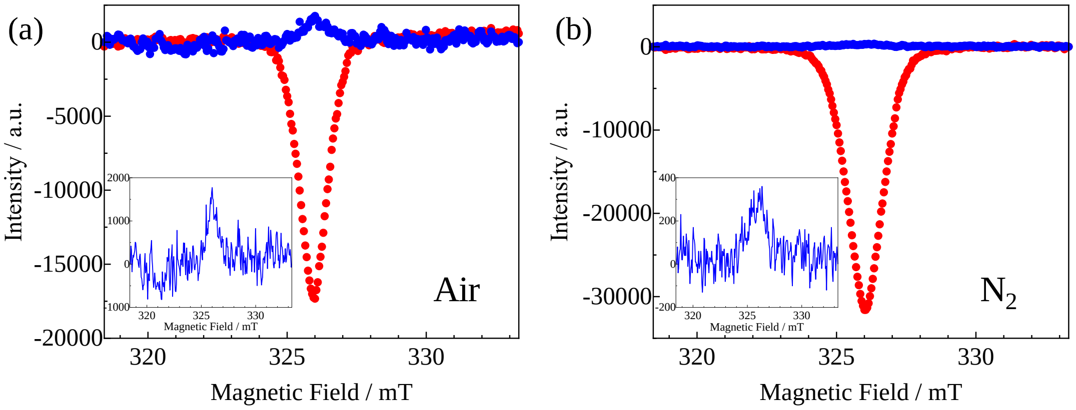

Fig. 5-6. The EDMR spectra of TIPS-Pn obtained upon monitoring the photocurrent (red curve) and persistent photocurrent (blue curve) at room temperature under an (a) air and (b) N_2 atmosphere. The insets are an enlarged view of the persistent-photocurrent-detected EDMR spectra.

5-5-3. Microwave Power Dependence of the EDMR Spectra at 80 K

The signal intensity in a solid is usually saturated at low temperature when strong microwave power is applied because of the slow spin-lattice relaxation time. This may cause the problem that distorts the shape of the spectrum. To obtain information accurate regarding the photocarrier-generation process, the microwave power dependence of the EDMR measurements was investigated. **Fig. 5-7a** shows the observed microwave power dependence of the photocurrent-detected EDMR spectra at 80 K. **Fig 5-7b** shows a plot of the EDMR spectral intensity versus the square root of the applied microwave power.[104, 105] The spectral intensities were calculated by integrating the area of the EDMR spectra. It is known that the spectral intensity is proportional to the square root of the microwave power when the power saturation is negligible. The linear relationship shown in **Fig. 5-7b** shows that saturation does not occur under the present conditions. This indicates the lifetime of the excited species in the TIPS-Pn film is sufficiently short. **Fig. 5-7c** shows the microwave power dependence of the normalized EDMR spectra. The EDMR spectra were analysed using **Eqn. 5.5**, which is the superposition of the Lorentzian and Gaussian functions.

$$\begin{aligned} I(H) = A_L \frac{1}{\pi}\frac{1}{\Delta B^L_{1/2}}\frac{1}{1+\left(1/\Delta B^L_{1/2}\right)^2 (B-B_0)^2} \\ + A_G \frac{1}{\pi}\frac{1}{\Delta B^G_{1/2}} \exp\frac{1}{\pi}\left(\frac{1}{\Delta B^G_{1/2}}\right)^2 (B-B_0)^2 \,. \end{aligned} \tag{5.5}$$

Figure 5-7d depicts the microwave power dependence of the linewidth for the Gaussian and Lorentzian components of the EDMR spectra. Their linewidths do not depend on the microwave power. The lower limit of the lifetime (the upper limit of the rate constant) can be estimated from the linewidth of the spectra when the lifetime is much smaller than the spin-spin and spin-lattice relaxation times, and the signal line shape is Lorentzian (negligible inhomogeneous broadening). From the linewidth (ΔB = 0.5 mT) of the Lorentzian line shape, the lower limit of the lifetime (τ) of the weakly coupled e–h pair was estimated using the following relationship: $\Delta B \sim h/g\beta\tau$. Thus, the upper limit of the rate constant (reciprocal of lifetime) of the ^{3}(e–h) pair is estimated to be $1/\tau = 8.6 \times 10^7\ \mathrm{s}^{-1}$ ($\tau = 1.16 \times 10^{-8}$ s) from the linewidth.

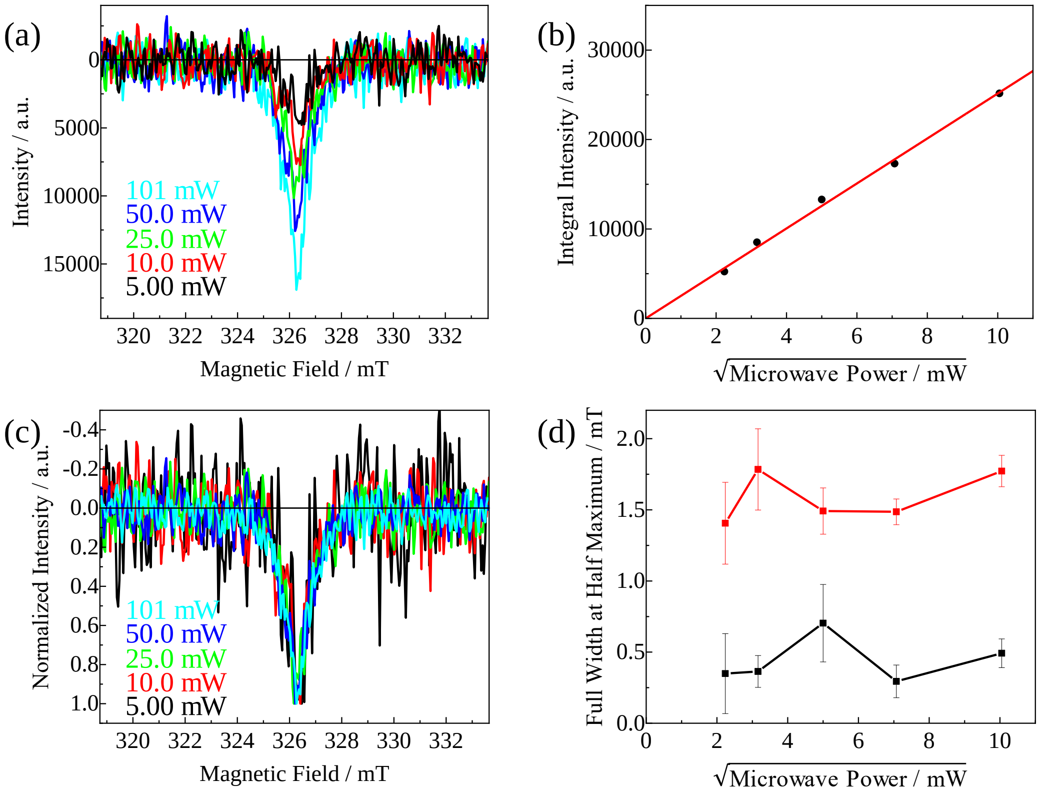

Fig. 5-7. (a) The microwave power dependent photocurrent-detected EDMR spectra obtained for the VVD-prepared TIPS-Pn film at 80 K in the N_2 atmosphere. (b) The microwave power dependent EDMR integral intensity. (c) The normalised EDMR spectra obtained for the TIPS-Pn VVD film at 80 K in the N_2 atmosphere. (d) The microwave power dependence of the Gaussian (red) and Lorentzian (black) linewidths.

5-5-4. Reference Signal Phase Dependence of EDMR at 200 K

Phase-sensitive detection measurements were carried out using a dual phase lock-in amplifier in which the amplitude and phase of the periodic signal are sensitively detected by comparing the phase between the measured and reference signals. When two components with different relaxation times exist in a sample, a slight phase shift between the components occurs with respect to the reference signal. **Figure 5-8** shows a schematic of the in-phase and out-of-phase detections of the two components with a slight phase shift. For the in-phase detection, the relative intensity ratio of the two components was small and both components were simultaneously detected. In contrast, when one of the components was adjusted to be out-of-phase, the other one is slightly shifted from out-of-phase, leading to a large difference in the signal intensity between the two components in the out-of-phase detection.

The phase dependency of the EDMR signal to the reference signal was carefully examined using a dual-phase lock-in amplifier. In this measurement, not only the amplitude of the EDMR signal, but also the phase difference with respect to the reference signal were measured. This small phase shift can be used to separate the EDMR signal components. In this study, the amplitude modulation technique was used to achieve the entire separation of the two signals. **Figures 5-9** and **5-10** show the in-phase (channel x) and out-of-phase (channel y) spectra obtained at 200 K, respectively. There is relatively little difference in the in-phase spectra even when a slight phase shift was induced. In the out-of-phase detection, the slight phase adjustment led to a large difference in the relative intensities. The signal was decomposed into two components, which were observed separately using the phase adjustment to out-of-phase. Component 1 has a Lorentzian line shape with a narrow linewidth ($\Delta B = 0.3$ mT) at $g = 2.0023$. Component 2 has a Gaussian line shape with a broad linewidth ($\Delta B = 1.8$ mT) at $g = 2.0022$. These g-values were slightly smaller than the values obtained for the TIPS-Pn cation radical in THF solution ($g = 2.0025$) and CH_2Cl_2 solution ($g = 2.0026$).[106] It is known that the one-side edges of the pentacene alignment will grow as they take on the SiO_2 substrate and the pentacene planes align nearly perpendicular to the substrate.[107, 108] In pentacene FET films, the g value is anisotropic, and it has been reported that the g value decreases when the substrate of pentacene film is parallel to the magnetic field, as shown in **Fig. 5-11**.[5] It is known that the ESR signals due to the FET device for $\boldsymbol{B}$ parallel ($\boldsymbol{B}_{//}$) and perpendicular ($\boldsymbol{B}_{\perp}$) to the substrate show clear anisotropy. The g values of $\boldsymbol{B}_{//}$ and $\boldsymbol{B}_{\perp}$ are 2.0024 and 2.0033, respectively. These g values show monotonic angular dependence values at intermediate angles between $\boldsymbol{B}_{//}$ and $\boldsymbol{B}_{\perp}$.[5] These g values is averaged values due to all possible in-plane molecular orientations in the arrangement of the molecules in the film. In the TIPS-Pn film made by the vapor deposition method, the pentacene planes is aligned nearly perpendicular to the substrate.[109, 110] In this study, an external magnetic field was applied parallel to the substrate of the TIPS-Pn VVD film. Therefore, obtaining a *g* value smaller than that in solution is reasonable under the experimental conditions use in this study.

In a zinc phthalocyanine single-layer device, the two-component decomposition in the EDMR signal utilising the out-of-phase detection was reported using the field modulation technique.[111] For the pentacene-Schottky diode, overlapped two-component EDMR signals of the Lorentz and Gaussian functions (not separated) have also reported.[112] Therein, the origin of the EDMR spectrum was discussed based on the positive bipolaron formation process, which involves the existence of a mobile polaron and trapped polaron in pentacene. In the present study, two possible mechanisms are considered to explain the origin of the two components in EDMR spectra. One is that their components can be attributed to a mobile polaron and trapped polaron, respectively, as reported in the pentacene-Schottky diode.[112] Another possibility is that there are two types of e–h pairs. The TIPS-Pn is known to have high hole mobility and low electron mobility. Therefore, in the former mechanism, the carriers with Lorentzian and Gaussian line shapes can be expected to be holes and electrons, respectively. In the model where electrons and holes are dissociated from the e–h pairs, equal amounts of electrons and holes are expected to be generated upon photoexcitation, followed by charge separation, as observed in the EDMR of OLEDs.[41] However, in the present system, the intensity of the two components in the EDMR signal differ significantly and the area-integrated intensity of the Lorentzian component expected with higher mobility was much smaller than that of the Gaussian component with relatively low mobility.[113] Therefore, the possibility that the two components are attributed to electrons and holes, respectively, dissociated from the e–h pairs can be ruled out. In the latter possibility, the following mechanism can be considered to be the origin of the two types of e–h pairs. Since the conductivity of the TIPS-Pn crystal is anisotropic, two types of e–h pairs are expected to exist, one consisting of carriers moving in the conductive paths through the stacked pentacene plane and another belonging to the low mobility pathway through the migration among different planes. The EDMR spectrum of the e–h pairs consisting of highly mobile carriers and relatively slow ones are expected to be the Lorentzian line shape due to the motional narrowing and the Gaussian line-shape by inhomogeneous broadening due to different local environments.

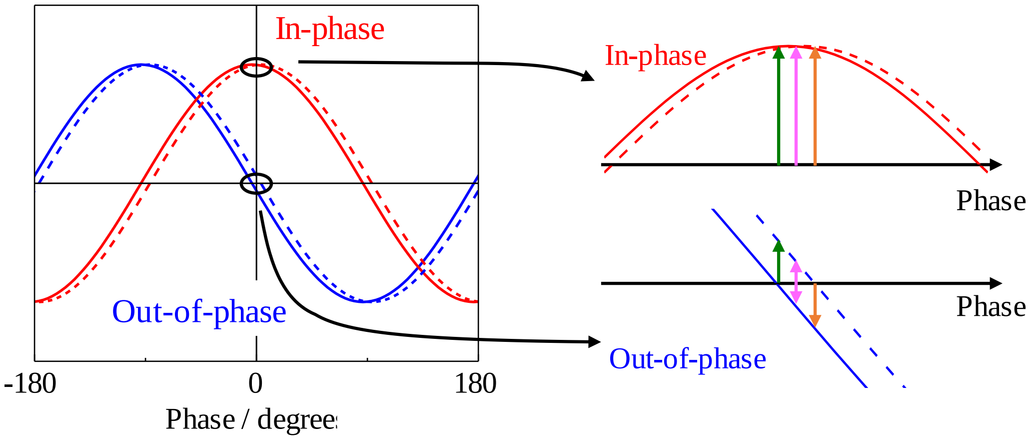

Fig. 5-8. Model of the output function of the reference signal phase for an EDMR signal. The red and blue curves show the in-phase (channel *x*) and out-of-phase (channel *y*) signal, respectively. The solid and dashed lines represent component 1 and 2, respectively.

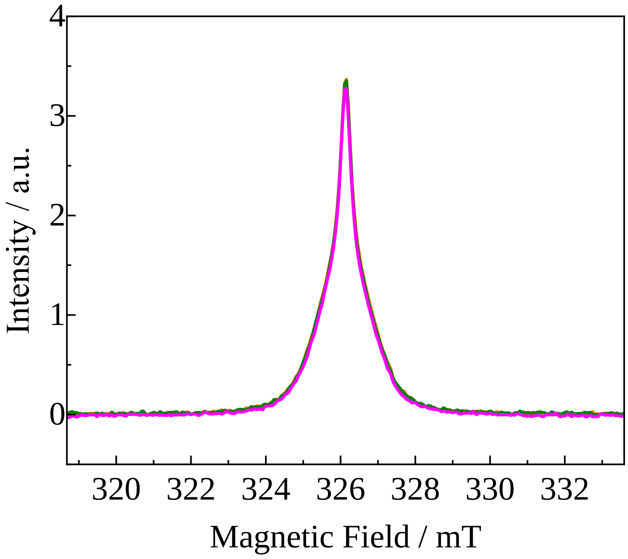

Fig. 5-9. The reference signal phase dependence of the in-phase EDMR spectra obtained in the N_2 atmosphere at 200 K.

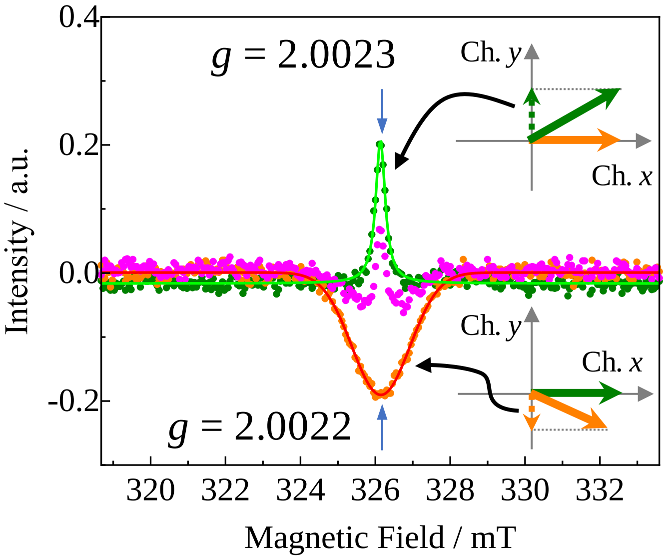

Fig. 5-10. The reference signal phase dependence of the out-of-phase EDMR spectra obtained in the N_2 atmosphere at 200 K.

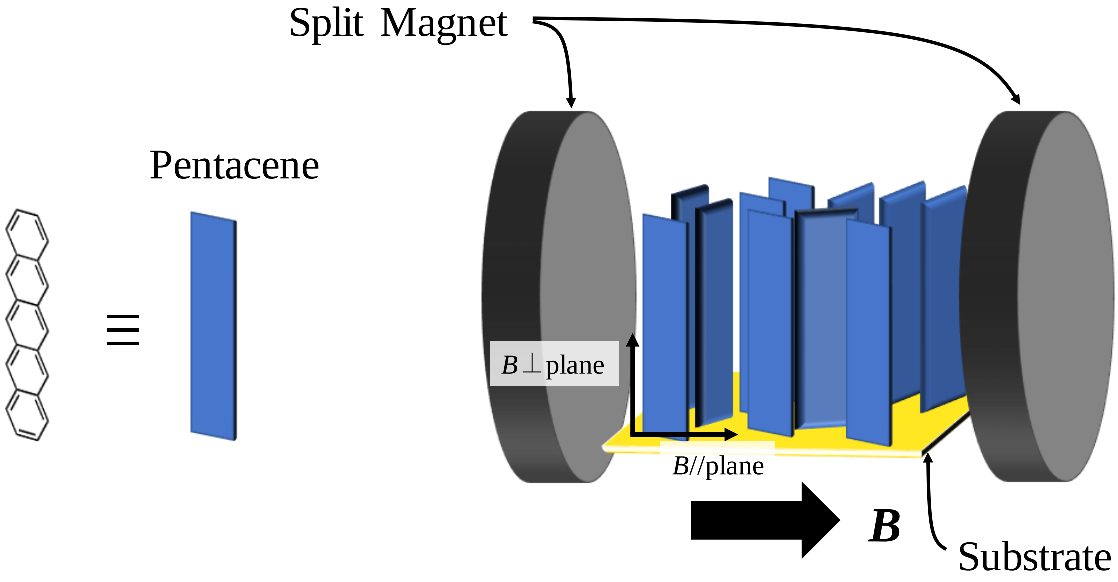

Fig. 5-11. Schematic of the orientation on pentacene.

5-5-5. Temperature Dependence of the EDMR Spectra

Temperature-dependent of the EDMR were carried out to elucidate the carrier generation spin dynamics of the e–h pairs. **Figure 5-12** shows the temperature dependence of the photocurrent-detected EDMR spectra under microwave irradiation at 101 mW. The inset is the relative value of the spectral intensity of the EDMR signal at 200 K, which increases from 80 to 200 K, and then decreases from 200 to 310 K. The spectra are well fit by the superposition of Lorentzian and Gaussian components (**Eqn. 5.5**). A common g-value (centre field, B_0) for the Lorentzian and Gaussian functions was used to reduce the variable parameters. It was confirmed that the EDMR spectra were composed of a narrow Lorentzian and a broader Gaussian line-shape function. **Figure 5-13** shows the temperature dependence of the linewidth for each component from 100 to 300 K. Fitting at temperatures below 100 K is difficult because of the poor signal-to-noise ratio. The linewidth of the Gaussian component was independent of temperature (~1.8 mT). In contrast, the linewidth of the Lorentzian component depends on the temperature, which varied from 0.6 to 1.1 mT. Below 200 K, the linewidth gradually narrowed with increasing temperature. This behaviour can be reasonably interpreted by the motional narrowing due to the thermal activation of the charge carriers. Above 200 K, the Lorentzian linewidth increase with increasing temperature due to the decrease in the spin-lattice relaxation time. Similar temperature-dependent linewidth behaviour was also reported in field-induced ESR studies of several OFETs.[90, 114] **Figure 5-14** shows the ratio of the amplitude of the Gaussian to Lorentzian component. The intensity of the Lorentzian component (A_L) is larger than that of the Gaussian component (A_G). The contribution of the Lorentzian component is larger than that of the Gaussian component below 150 K. However, the contribution of the Lorentzian component decreases as the temperature increases and remained constant at approximately one–half of the Gaussian component above 200 K.

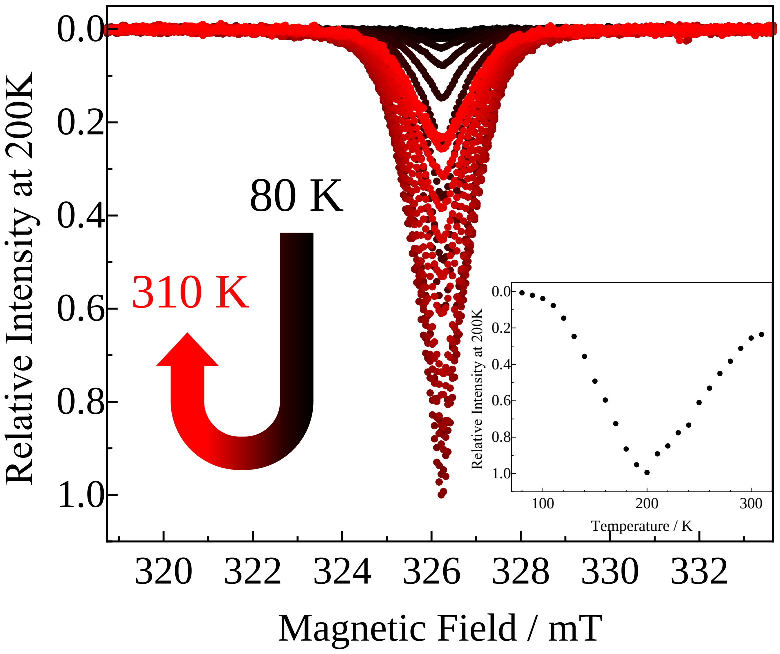

Fig. 5-12. The temperature dependence of the photocurrent-detected EDMR spectra of the TIPS-Pn VVD film in the N_2 atmosphere. The inset is the temperature dependence of the EDMR intensity.

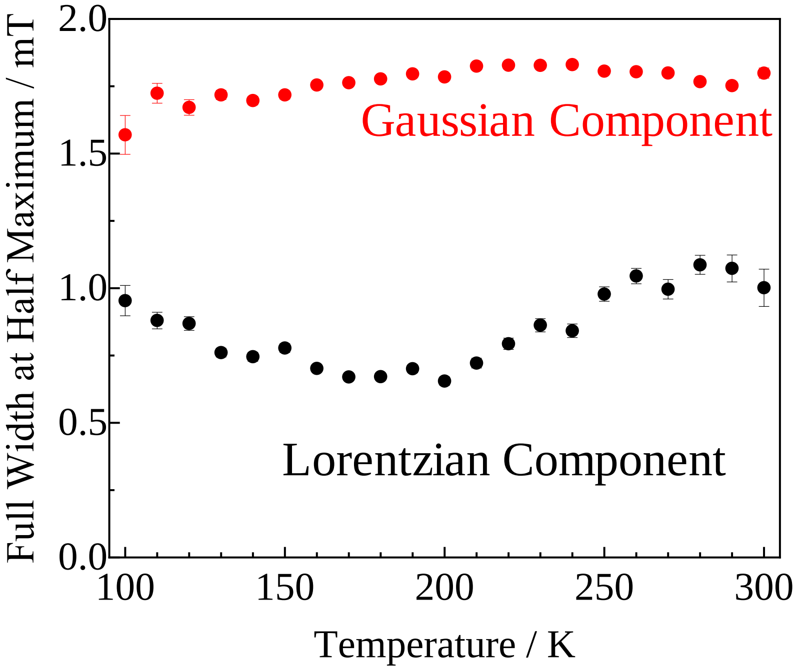

Fig. 5-12. The temperature dependence of the photocurrent-detected EDMR spectra of the TIPS-Pn VVD film in the N_2 atmosphere.

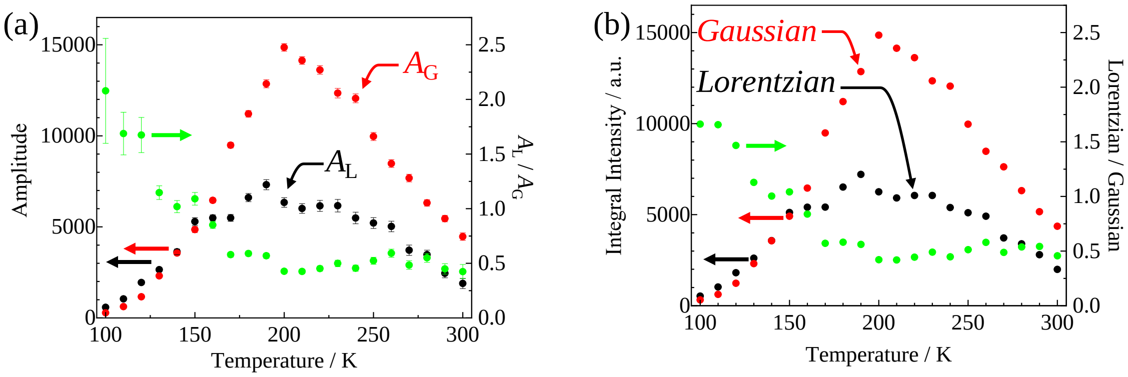

Fig. 5-14. (a) The temperature dependence of the amplitude of the Gaussian and Lorentzian components. (b) The temperature dependence of the integral intensities of the Gaussian and Lorentzian components. The black, red and green circles show the Lorentzian, Gaussian and Lorentzian/Gaussian amplitudes, respectively.

5-5-6. Analytical Solution and Spectra Simulation of the EDMR

The characteristic behaviour of the observed photocurrent-detected EDMR signals were consistent with the S-born model presented in **Scheme 5-1**. The photocurrent is not directly generated from the excited state, but is generated via e–h pairs. If the number of carriers generated from e–h pairs is changed by the ESR transitions, the EDMR signal (I_{EDMR}) can be expressed as a difference in the current intensity between the presence and absence of microwave irradiation as follows:

$$I_{\mathrm{EDMR}} = I_{on} - I_{off}\ . \tag{5.6}$$

where I_{on} and I_{off} denote the photocurrent intensity in the presence and absence of microwave irradiation, respectively. According to the S-born model, the photocurrent (I) is given as the sum of the population density (ρ) of each spin sub-level multiplied by the rate constant of the dissociation of e–h pairs (k_{dis}). In this case, the transition rate, k_{dis}, is equal between the ^{1}(e–h) and ^{3}(e–h) pairs because the process of carrier generation from each spin sub-level in the e–h pair is non-geminate.

$$I = \sum_{i}^{S,T_+,T_0,T_-} k_{\mathrm{dis}}\rho_i\ . \tag{5.7}$$

It should be noted that, in the EDMR experiments, field-induced intersystem crossing (S-

T_0 mixing) occurred ($k_{ISC} \neq 0$ s^{-1}) via the Δg mechanism and $k_{ESR} \neq 0$ s^{-1} at the resonance field. The Kaplan, Solomon, and Mott model (KSM model)[115] has been reported to explain the EDMR of the e–h pairs in charge transport in the ground state. However, the EDMR signal of the persistent photocurrent under non-light irradiation is significantly smaller than the EDMR signal from light irradiation. Hence, this photocurrent-detected EDMR signal is thought to originate from the carrier generation process from the e–h pair. It should be noted that the free electron or hole cannot contribute to the EDMR signal because the transition of the mobile carrier between the α and β spin states does not change the mobility and carrier density. The observed EDMR spectrum of the TIPS-Pn VVD film can be understood to originate from a weakly interacting e–h-pair signal because it is a single-line signal at the central magnetic field in the g ~2 region with negligible exchange and fine structure interactions. The rate constant for carrier generation (k_{dis}) from the e–h pair is given by **Eqn. 5.4** in **Section 5-4**. The ^{1}(e–h) and ^{3}(e–h) recombine to the singlet ground state (S_0) with a rate constant k_S and to the triplet excited state (T_1) with a rate constant k_T, respectively. Under a magnetic field in the g ~2 region, B-dependent ISC due to the Δg mechanism occurs between the $|S\rangle$ and $|T_0\rangle$ spin sub-levels (S-T_0 mixing) in the e–h pair with a transition rate of k_{ISC}. Since the spin conversions between the $|S\rangle$ and $|T_\pm\rangle$ sub-levels are not allowed because the Zeeman energy due to the external magnetic field is much larger than the hyperfine coupling or fine structure terms of the e–h pair, they were neglected in the current model. The transition between the spin sub-levels of T_+, T_0, T_0, and T_- are induced when microwaves with equal energy to the Zeeman splitting energy are irradiated, which has a rate constant of the ESR transition (k_{ESR}). The rate constants k_S, k_T, k_{ISC}, and k_{ESR} are independent of temperature. The population density (ρ) of each spin sub-level under resonance conditions in the S-born model can be obtained by the steady-state approximation using **Eqn. 5.8**.

$$\begin{cases} \dfrac{d\rho_S^{on}}{dt} = I_0 - k_{\mathrm{ISC}}\rho_S^{on} - k_{\mathrm{dis}}\rho_S^{on} - k_{\mathrm{S}}\rho_S^{on} + k_{\mathrm{ISC}}\rho_{T_0}^{on} = 0 \\ \dfrac{d\rho_{T_0}^{on}}{dt} = k_{\mathrm{ISC}}\rho_S^{on} - k_{\mathrm{ISC}}\rho_{T_0}^{on} - 2k_{\mathrm{ESR}}\rho_{T_0}^{on} - k_{\mathrm{dis}}\rho_{T_0}^{on} - k_{\mathrm{T}}\rho_{T_0}^{on} + k_{\mathrm{ESR}}\rho_{T_+}^{on} + k_{\mathrm{ESR}}\rho_{T_-}^{on} = 0 \\ \dfrac{d\rho_{T_+}^{on}}{dt} = k_{\mathrm{ESR}}\rho_{T_0}^{on} - k_{\mathrm{ESR}}\rho_{T_+}^{on} - k_{\mathrm{dis}}\rho_{T_+}^{on} - k_{\mathrm{T}}\rho_{T_+}^{on} = 0 \\ \dfrac{d\rho_{T_-}^{on}}{dt} = k_{\mathrm{ESR}}\rho_{T_0}^{on} - k_{\mathrm{ESR}}\rho_{T_-}^{on} - k_{\mathrm{dis}}\rho_{T_-}^{on} - k_{\mathrm{T}}\rho_{T_-}^{on} = 0 \end{cases} . \quad (5.8)$$

The analytical solutions of the densities (ρ_i^{on}) are given as follows:

$$\rho_S^{on} = I_0 \frac{k_{\mathrm{ISC}}k_{\mathrm{ESR}} + (k_{\mathrm{dis}} + k_{\mathrm{T}})(k_{\mathrm{ISC}} + 3k_{\mathrm{ESR}} + k_{\mathrm{dis}} + k_{\mathrm{T}})}{F + G}, \quad (5.9)$$

$$\rho_{T_0}^{on} = I_0 \frac{k_{\mathrm{ISC}}(k_{\mathrm{ESR}} + k_{\mathrm{dis}} + k_{\mathrm{T}})}{F + G}, \quad (5.10)$$

$$\rho_{T_+}^{on} = \rho_{T_-}^{on} = I_0 \frac{k_{\mathrm{ISC}}k_{\mathrm{ESR}}}{F + G} \ , \quad (5.11)$$

where

$$F = k_{\mathrm{ISC}}(k_{\mathrm{dis}} + k_{\mathrm{S}})(k_{\mathrm{ESR}} + k_{\mathrm{dis}} + k_{\mathrm{T}}) + 2k_{\mathrm{ESR}}(k_{\mathrm{dis}} + k_{\mathrm{T}})(k_{\mathrm{ISC}} + k_{\mathrm{dis}} + k_{\mathrm{S}})\,, \quad (5.12)$$

$$G = (k_{\mathrm{dis}} + k_{\mathrm{T}})(k_{\mathrm{ISC}} + k_{\mathrm{dis}} + k_{\mathrm{S}})(k_{\mathrm{ESR}} + k_{\mathrm{dis}} + k_{\mathrm{T}}). \quad (5.13)$$

By substituting **Eqn. 5.9–5.11** into **Eqn. 5.7**, the photocurrent intensity under resonance conditions can be given by:

$$I_{on} = k_{\mathrm{dis}} I_0 \frac{4k_{ISC}k_{\mathrm{ESR}} + (k_{\mathrm{dis}} + k_{\mathrm{T}})(2k_{ISC} + 3k_{\mathrm{ESR}} + k_{\mathrm{dis}} + k_{\mathrm{T}})}{F + G}. \quad (5.14)$$

The analytical solutions of the photocurrent intensity and population density (ρ_i^{off}) for each spin sub-level under non-resonance conditions can be obtained by solving the following simultaneous equations using the steady-state approximation:

$$\begin{cases} \dfrac{d\rho_S^{off}}{dt} = I_0 - k_{\mathrm{ISC}}\rho_S^{off} - k_{\mathrm{dis}}\rho_S^{off} - k_{\mathrm{S}}\rho_S^{off} + k_{\mathrm{ISC}}\rho_{T_0}^{off} = 0 \\ \dfrac{d\rho_{T_0}^{off}}{dt} = k_{\mathrm{ISC}}\rho_S^{off} - k_{\mathrm{ISC}}\rho_{T_0}^{off} - k_{\mathrm{dis}}\rho_{T_0}^{off} - k_{\mathrm{T}}\rho_{T_0}^{off} = 0 \\ \dfrac{d\rho_{T_+}^{off}}{dt} = 0 \\ \dfrac{d\rho_{T_-}^{off}}{dt} = 0 \end{cases} . \quad (5.15)$$

The analytical solutions of the densities (ρ_i^{off}) are obtained as follows:

$$\rho_S^{off} = I_0 \frac{k_{\mathrm{ISC}} + k_{\mathrm{dis}} + k_{\mathrm{T}}}{k_{\mathrm{ISC}}(k_{\mathrm{dis}} + k_{\mathrm{S}}) + k_{\mathrm{ISC}}(k_{\mathrm{dis}} + k_{\mathrm{T}}) + (k_{\mathrm{dis}} + k_{\mathrm{S}})(k_{\mathrm{dis}} + k_{\mathrm{T}})}, \tag{5.16}$$

$$\rho_{T_0}^{off} = I_0 \frac{k_{\mathrm{ISC}}}{k_{\mathrm{ISC}}(k_{\mathrm{dis}} + k_{\mathrm{S}}) + k_{\mathrm{ISC}}(k_{\mathrm{dis}} + k_{\mathrm{T}}) + (k_{\mathrm{dis}} + k_{\mathrm{S}})(k_{\mathrm{dis}} + k_{\mathrm{T}})}, \tag{5.17}$$

$$\rho_{T_+}^{off} = \rho_{T_-}^{off} = 0\,. \tag{5.18}$$

By substituting **Eqn. 5.16–5.18** into **Eqn. 5.7**, the photocurrent intensity under resonance conditions can be given by:

$$I_{off} = k_{\mathrm{dis}} I_0 \frac{2k_{\mathrm{ISC}} + k_{\mathrm{dis}} + k_{\mathrm{T}}}{k_{\mathrm{ISC}}(k_{\mathrm{dis}} + k_{\mathrm{S}}) + k_{\mathrm{ISC}}(k_{\mathrm{dis}} + k_{\mathrm{T}}) + (k_{\mathrm{dis}} + k_{\mathrm{S}})(k_{\mathrm{dis}} + k_{\mathrm{T}})}\,. \tag{5.19}$$

In addition, substituting **Eqn. 5.14** and **Eqn. 5.19** into **Eqn. 5.6**, the EDMR intensity (I_{EDMR}) can be expressed as follows:

$$\begin{aligned} I_{\mathrm{EDMR}} &= I_{on} - I_{off} \\ &= \frac{2I_0 k_{\mathrm{ESR}} k_{\mathrm{dis}} k_{\mathrm{ISC}}^2 (k_{\mathrm{S}} - k_{\mathrm{T}})}{AC}, \end{aligned} \tag{5.20}$$

where

$$A = (k_{\mathrm{T}} + k_{\mathrm{dis}})(k_{\mathrm{S}} + k_{\mathrm{ISC}} + k_{\mathrm{dis}}) + k_{\mathrm{ISC}}(k_{\mathrm{S}} + k_{\mathrm{dis}})\,, \tag{5.21}$$

$$\begin{aligned} C = {} & k_{\mathrm{ISC}}(k_{\mathrm{S}} + k_{\mathrm{dis}})(k_{\mathrm{ESR}} + k_{\mathrm{T}} + k_{\mathrm{dis}}) \\ & + (k_{\mathrm{S}} + k_{\mathrm{ISC}} + k_{\mathrm{dis}})(k_{\mathrm{T}} + k_{\mathrm{dis}})(3k_{\mathrm{ESR}} + k_{\mathrm{T}} + k_{\mathrm{dis}})\,. \end{aligned} \tag{5.22}$$

The analytical solution demonstrates that the sign of the EDMR signal can be determined by the difference in the transition rate constants k_{S} and k_{T}. The EDMR signal is not observed when $k_{\mathrm{ISC}} = 0$ and/or $k_{\mathrm{S}} = k_{\mathrm{T}}$. In addition, the EDMR intensity decreases when k_{S} and k_{T} are sufficiently larger than the generation rate constant of the carriers (k_{dis}).

As previously mentioned, the population from $|S_1\rangle$ to $|S\rangle$ is an appropriate situation leading on from Rehm's equation. However, the analytical solution with the selective population to $|T_0\rangle$ was also solved. Here, the analytical solution for the EDMR based on the $\mathrm{T_0}$-born model is shown in **Scheme 5-2**. The analytical solution of the EDMR can be derived by solving the simultaneous rate equations for the ^{1}(e–h) and ^{3}(e–h) pairs, as shown in **Scheme 5-2**. The rate constants k_S, k_T, k_ISC, and k_ESR are independent of temperature. The population density (ρ) of each spin sub-level under ESR conditions can be obtained based on the $\mathrm{T_0}$-bone model by solving the following simultaneous equations using the steady-state approximation:

$$\begin{cases} \dfrac{d\rho_S^{on}}{dt} = -k_\mathrm{ISC}\rho_S^{on} - k_\mathrm{dis}\rho_S^{on} - k_\mathrm{S}\rho_S^{on} + k_\mathrm{ISC}\rho_{T_0}^{on} = 0 \\ \dfrac{d\rho_{T_0}^{on}}{dt} = I_0 - k_\mathrm{ISC}\rho_S^{on} - k_\mathrm{ISC}\rho_{T_0}^{on} - 2k_\mathrm{ESR}\rho_{T_0}^{on} - k_\mathrm{dis}\rho_{T_0}^{on} \\ \qquad\qquad -k_\mathrm{T}\rho_{T_0}^{on} + k_\mathrm{ESR}\rho_{T_+}^{on} + k_\mathrm{ESR}\rho_{T_-}^{on} = 0\ . \\ \dfrac{d\rho_{T_+}^{on}}{dt} = k_\mathrm{ESR}\rho_{T_0}^{on} - k_\mathrm{ESR}\rho_{T_+}^{on} - k_\mathrm{dis}\rho_{T_+}^{on} - k_\mathrm{T}\rho_{T_+}^{on} = 0 \\ \dfrac{d\rho_{T_-}^{on}}{dt} = k_\mathrm{ESR}\rho_{T_0}^{on} - k_\mathrm{ESR}\rho_{T_-}^{on} - k_\mathrm{dis}\rho_{T_-}^{on} - k_\mathrm{T}\rho_{T_-}^{on} = 0 \end{cases} \tag{5.23}$$

The analytical solutions of the densities (ρ_i^{on}) are:

$$\rho_S^{on} = I_0\frac{k_\mathrm{ISC}(k_\mathrm{ESR} + k_\mathrm{dis} + k_\mathrm{T})}{H + I}, \tag{5.24}$$

$$\rho_{T_0}^{on} = I_0\frac{(k_\mathrm{ISC} + k_\mathrm{dis} + k_\mathrm{S})(k_\mathrm{ESR} + k_\mathrm{dis} + k_\mathrm{T})}{H + I}, \tag{5.25}$$

$$\rho_{T_+}^{on} = \rho_{T_-}^{on} = I_0\frac{k_\mathrm{ESR}(k_\mathrm{ISC} + k_\mathrm{dis} + k_\mathrm{S})}{H + I}, \tag{5.26}$$

where

$$H = (k_\mathrm{S} + k_\mathrm{ISC} + k_\mathrm{dis})(k_T + k_{dis})(3k_\mathrm{ESR} + k_\mathrm{T} + k_\mathrm{dis}), \tag{5.27}$$

$$I = k_\mathrm{ISC}(k_\mathrm{S} + k_\mathrm{dis})(k_\mathrm{ESR} + k_\mathrm{T} + k_\mathrm{dis})\ . \tag{5.28}$$

By substituting **Eqn. 5.24–5.26** into **Eqn. 5.7**, the photocurrent intensity under resonance conditions can be given by:

$$I_{on} = k_{dis}I_0\frac{\begin{gathered} k_\mathrm{ISC}(k_\mathrm{ESR} + k_\mathrm{dis} + k_\mathrm{T}) + 2k_\mathrm{ESR}(k_\mathrm{ISC} + k_\mathrm{dis} + k_\mathrm{S}) \\ +(k_{ISC} + k_\mathrm{dis} + k_\mathrm{S})(k_\mathrm{ESR} + k_\mathrm{dis} + k_\mathrm{T}) \end{gathered}}{H + I}\ . \tag{5.29}$$

The analytical solutions of the photocurrent intensity and the population density (ρ_i^{off}) for each spin sub-level under non-resonance conditions were obtained using the steady-state approximation by solving the following expression:

$$\begin{cases} \dfrac{d\rho_S^{off}}{dt} = -k_{\mathrm{ISC}}\rho_S^{off} - k_{\mathrm{dis}}\rho_S^{off} - k_S\rho_S^{off} + k_{\mathrm{ISC}}\rho_{T_0}^{off} = 0 \\ \dfrac{d\rho_{T_0}^{off}}{dt} = I_0 + k_{\mathrm{ISC}}\rho_S^{off} - k_{\mathrm{ISC}}\rho_{T_0}^{off} - k_{\mathrm{dis}}\rho_{T_0}^{off} - k_T\rho_{T_0}^{off} = 0 \\ \dfrac{d\rho_{T_+}^{off}}{dt} = 0 \\ \dfrac{d\rho_{T_-}^{off}}{dt} = 0 \end{cases}, \tag{5.30}$$

The analytical solutions of the densities (ρ_i^{off}) are:

$$\rho_S^{off} = I_0 \frac{k_{\mathrm{ISC}}}{(k_{\mathrm{ISC}} + k_{\mathrm{dis}} + k_{\mathrm{S}})(k_{\mathrm{ISC}} + k_{\mathrm{dis}} + k_{\mathrm{T}}) - k_{ISC}^2}, \tag{5.31}$$

$$\rho_{T_0}^{off} = I_0 \frac{k_{\mathrm{ISC}} + k_{\mathrm{dis}} + k_T}{(k_{\mathrm{ISC}} + k_{\mathrm{dis}} + k_{\mathrm{S}})(k_{\mathrm{ISC}} + k_{\mathrm{dis}} + k_{\mathrm{T}}) - k_{ISC}^2}, \tag{5.32}$$

$$\rho_{T_+}^{off} = \rho_{T_-}^{off} = 0\,. \tag{5.33}$$

By substituting **Eqn. 5.31–5.33** into **Eqn. 5.7**, the photocurrent intensity under resonance conditions is given by:

$$I_{off} = k_{\mathrm{dis}} I_0 \frac{2k_{\mathrm{ISC}} + k_{\mathrm{dis}} + k_{\mathrm{T}}}{(k_{\mathrm{ISC}} + k_{\mathrm{dis}} + k_{\mathrm{S}})(k_{\mathrm{ISC}} + k_{\mathrm{dis}} + k_{\mathrm{T}}) - k_{\mathrm{ISC}}^2}\,. \tag{5.34}$$

Substituting **Eqn. 5.29** and **Eqn. 5.32** into **Eqn. 5.6**, the EDMR intensity (I_{EDMR}) can be expressed as follows:

$$\begin{aligned} I_{\mathrm{EDMR}} &= I_{on} - I_{off} \\ &= \frac{2I_0 k_{\mathrm{ESR}} k_{\mathrm{dis}} k_{\mathrm{ISC}} (k_{\mathrm{T}} - k_{\mathrm{S}})(k_{\mathrm{S}} + k_{\mathrm{ISC}} + k_{\mathrm{dis}})}{AC}, \end{aligned} \tag{5.35}$$

where *A* and *C* are **Eqn. 5.21 and Eqn. 5.22**, respectively. Using the same parameters, **Eqn. 5.35** obtained by the T_0-born model has the opposite sign of the signal in **Eqn. 5.20** obtained using the S-born model.

Figure 5-15 shows the temperature dependence of k_{dis}, k_{S}, and k_{T}. The maximum intensity of EDMR was obtained when the k_{dis} value was close to those of k_{S} and k_{T}, which was achieved at 200 K in the TIPS-Pn system studied in this work.

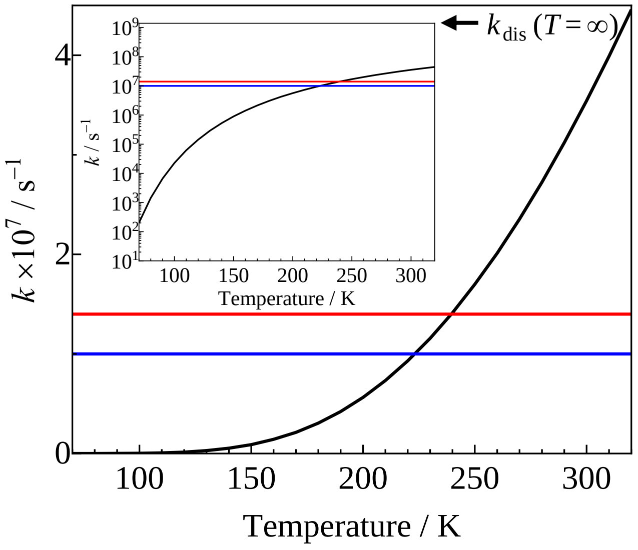

Fig. 5-15. The temperature dependence of k_{dis} (black curve; $k_0 = 1.4 \times 10^9$ s^{-1}, $E/k_{\mathrm{B}} = 1103$ K), k_{S} (blue curve; $k_0 = 1.0 \times 10^9$ s^{-1}), and k_{T} (red curve; $k_0 = 1.4 \times 10^7$ s^{-1}). The inset is a logarithm scale for the vertical axis.

Figure 5-16 shows the temperature dependence of the populations (ρ_i) of each spin sub-level using the S-born model. Under off-resonance conditions, there was no population of $|T_+\rangle$ and $|T_-\rangle$. However, under resonant conditions, non-zero populations of $|T_+\rangle$ and $|T_-\rangle$ are generated with a decrease in the $|S\rangle$ population.

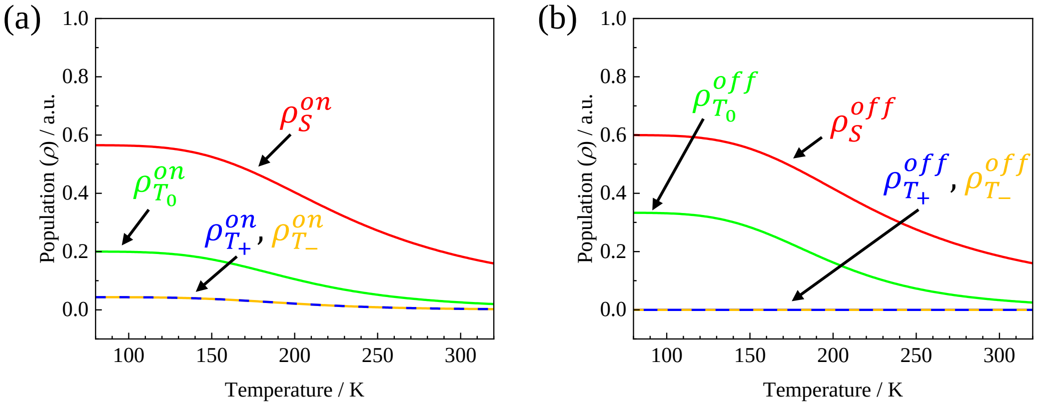

Fig. 5-16. (a) The temperature dependence of the populations (ρ_i) in each spin sub-level. ($k_{\mathrm{S}} = 1.0 \times 10^7$ s^{-1}, $k_{\mathrm{T}} = 2.0 \times 10^7$ s^{-1}, $k_0 = 1.0 \times 10^9$ s^{-1}, $E/k_{\mathrm{B}} = 1000$ K, $k_{\mathrm{ESR}} = 1.0 \times 10^7$ s^{-1}, and $k_{\mathrm{ISC}} = 1.0 \times 10^7$ s^{-1}) under resonance conditions. (b) The same temperature dependence under off-resonance conditions.

Figure 5-17 shows the E/k_B and k_0 dependence of the EDMR peak using the S-born model. Although temperature width depends on the k_{dis}, the maximum intensity was independent of these parameters. The peak temperature according to the k_{dis} parameter shifts to the high temperature side as k_{dis} parameters (k_0 and E) increases and the peak temperature is proportional to E/k_B.

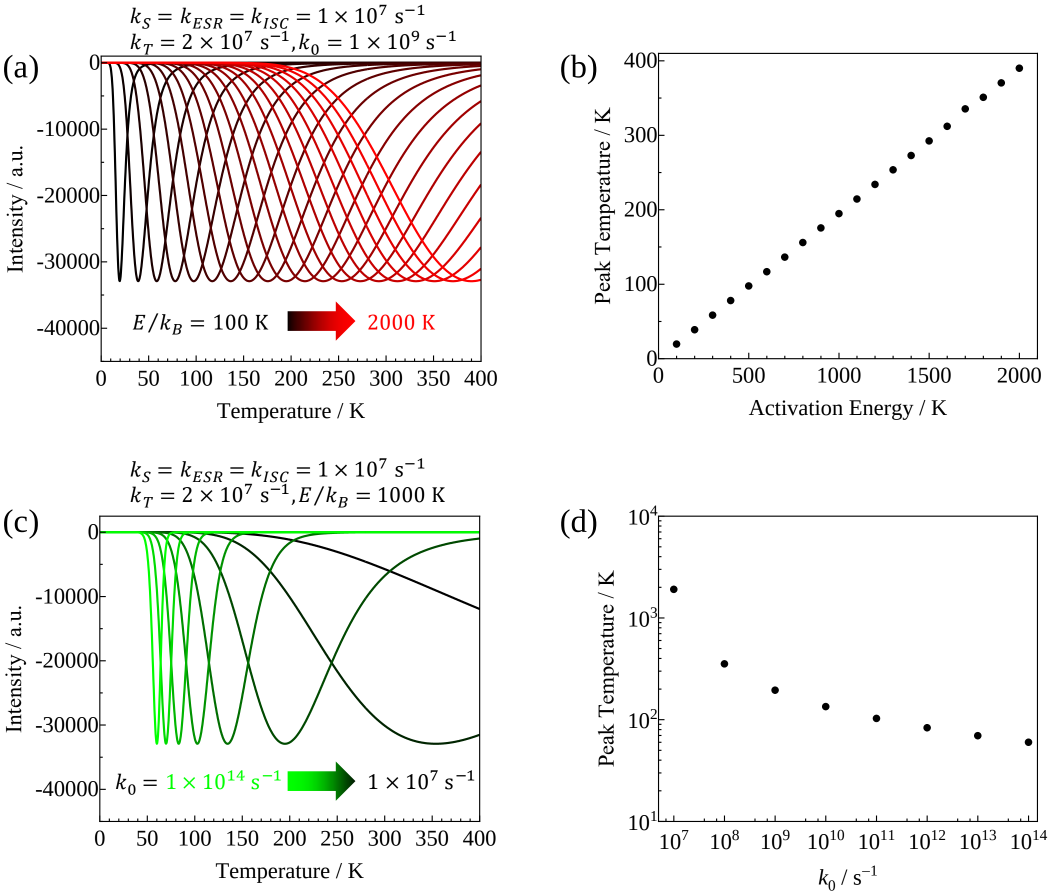

Fig. 5-17. (a) The E/k_B dependence of the EDMR peak and (b) peak temperature vs. activation energy (E/k_B). ($k_S = 1.0 \times 10^7$ s^{-1}, $k_T = 2.0 \times 10^7$ s^{-1}, $k_0 = 1.0 \times 10^9$ s^{-1}, $k_{ESR} = 1.0 \times 10^7$ s^{-1}, and $k_{ISC} = 1.0 \times 10^7$ s^{-1}). (c) The k_0 dependence of the EDMR behaviour and (d) peak temperature vs. k_0. ($k_S = 1.0 \times 10^7$ s^{-1}, $k_T = 1.4 \times 10^7$ s^{-1}, E/k_B = 1000 K, $k_{ESR} = 1.0 \times 10^7$ s^{-1}, and $k_{ISC} = 1.0 \times 10^7$ s^{-1}).

Figure 5-18 shows the simulated EDMR intensity dependence as a function of k_T using the S-born model. The analytical solution shows that the sign of the EDRM signal is determined by the difference in the rate constants, (k_S−k_T). EDMR is not observed when $k_\mathrm{S} = k_\mathrm{T} = 0$. Although the ^{3}(e−h) pair of the $|T_0\rangle$ state is mixing to ^{1}(e−h) pair of the $|S\rangle$ state by the Δg mechanism, the ^{3}(e−h) pair of the $|T_+\rangle$ and $|T_-\rangle$ states are not mixing to ^{1}(e−h) pair state. When ESR transition occurs the population of $|T_0\rangle$ is transferred to $|T_+\rangle$ and $|T_-\rangle$. Thus, population of $|S\rangle$ decreases through the S-T$_0$ mixing. Hence, the signal is positive when $k_\mathrm{S} > k_\mathrm{T}$ and negative when $k_\mathrm{S} < k_\mathrm{T}$. The EDMR intensity significantly decreases when k_T is sufficiently higher than k_dis. The peak position depends on k_T when k_T was close to the other transition rate constants (k_ISC and k_ESR).

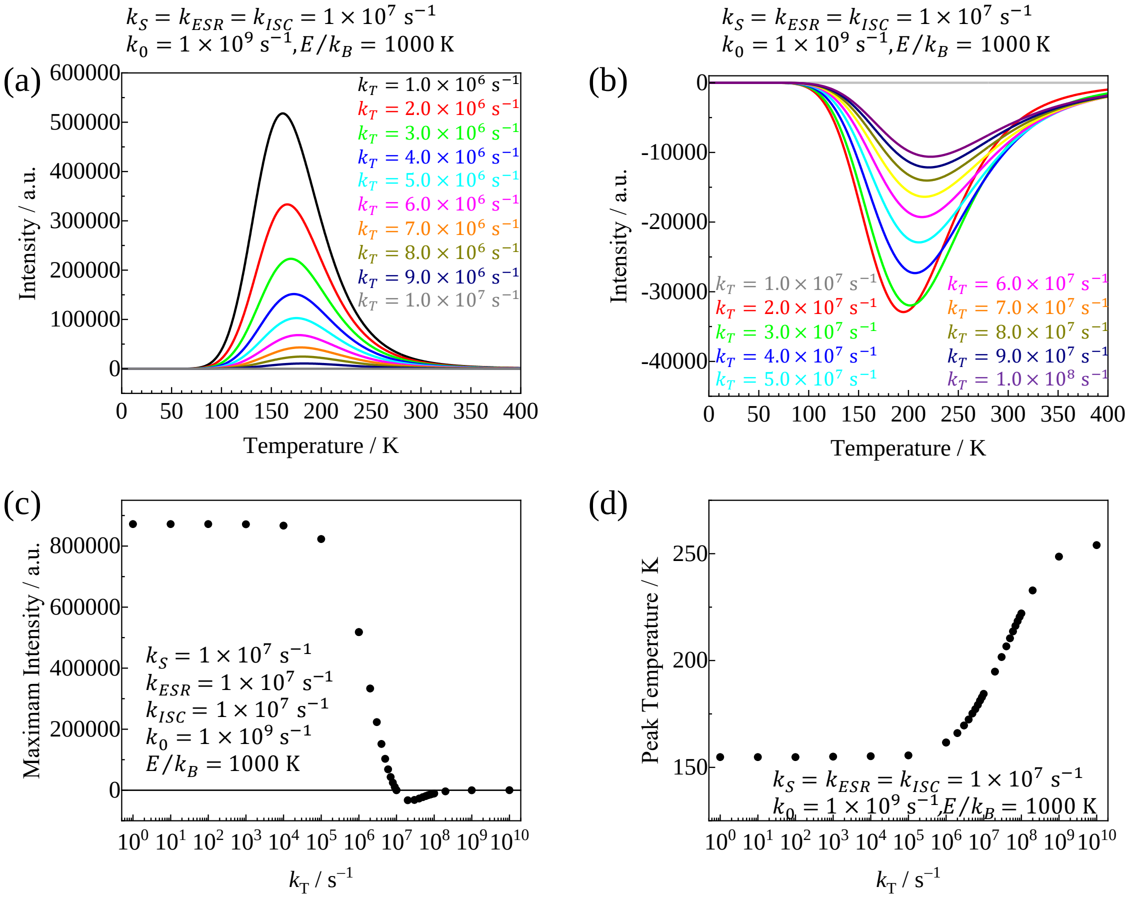

Fig. 5-18. The k_T dependence of the EDMR behaviour: (a) $k_\mathrm{T} = 10^6$ to 10^7 s^{-1} and (b) $k_\mathrm{T} = 10^7$ to 10^8 s^{-1}. (c) Peak temperature vs. k_T. (d) Maximum intensity vs. k_T ($k_\mathrm{S} = 1.0 \times 10^7$ s^{-1}, $k_0 = 1.0 \times 10^9$ s^{-1}, $E/k_\mathrm{B} = 1000$ K, $k_\mathrm{ESR} = 1.0 \times 10^7$ s^{-1}, and $k_\mathrm{ISC} = 1.0 \times 10^7$ s^{-1}).

Figure 5-19 shows the simulated k_{ESR} and k_{ISC} dependence of the EDMR intensity using the S-born model. The temperature dependence of the EDMR peak vs. k_{ESR} is similar to that of k_{ISC}. The peak position depends on k_{ESR} and k_{ISC}, when k_{ESR} and k_{ISC} are close to the other rate constants. The behaviours were quite similar to those presented in **Fig. 5–17d**, but a little change was observed. The EDMR signal was not observed when $k_{\mathrm{ESR}} = 0$ and/or $k_{\mathrm{ISC}} = 0$. The maximum intensity increases monotonically with increasing k_{ESR} and k_{ISC}. When the values of k_{ESR} and/or k_{ISC} are more than two orders of magnitude smaller than the other parameters, the signal is almost unobservable. When the values of k_{ESR} and/or k_{ISC} are also two orders of magnitude greater than the other parameters, the signal intensity approaches a constant value.

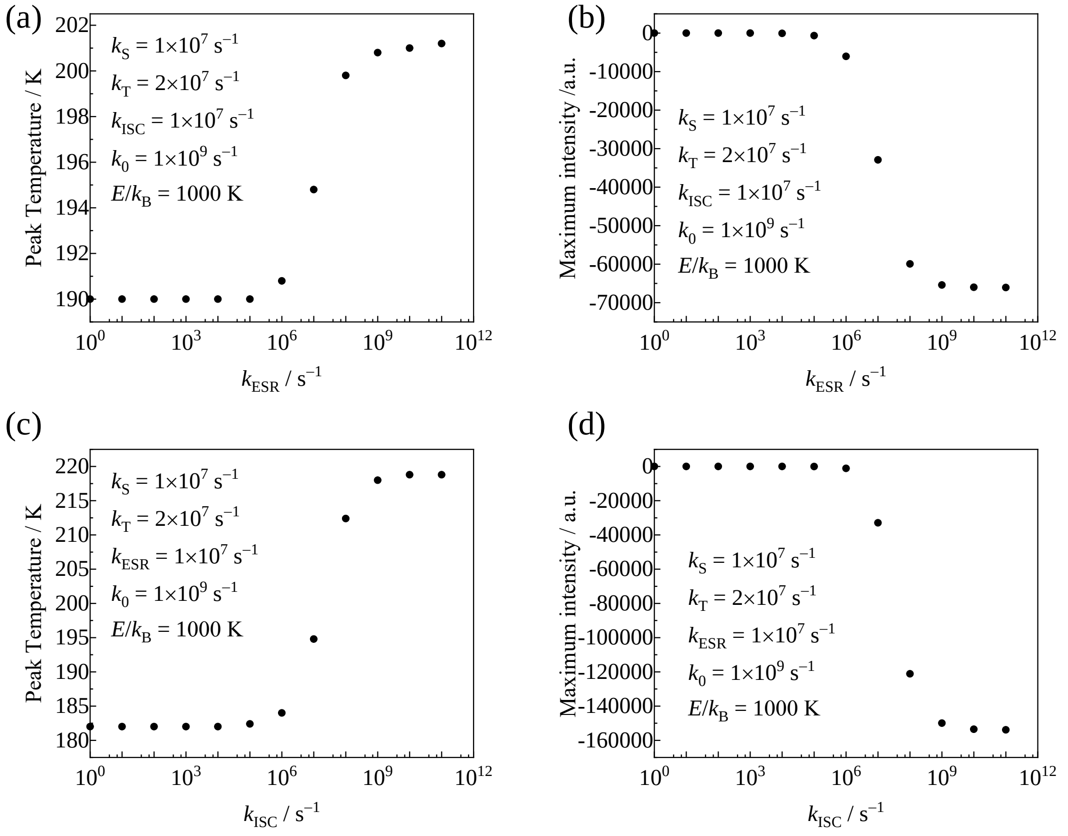

Fig. 5-19. The k_{ESR} dependence of the EDMR behaviour: (a) Peak temperature vs. k_{ESR}, (b) maximum intensity vs. k_{ESR}. ($k_{\mathrm{S}} = 1.0 \times 10^7\ \mathrm{s}^{-1}$, $k_{\mathrm{T}} = 2.0 \times 10^7\ \mathrm{s}^{-1}$, $k_0 = 1.0 \times 10^9\ \mathrm{s}^{-1}$, $E/k_{\mathrm{B}} = 1000$ K, and $k_{\mathrm{ISC}} = 1.0 \times 10^7\ \mathrm{s}^{-1}$) and the k_{ISC} dependence of the EDMR behaviour, (c) peak temperature vs. k_{ISC}, and (d) maximum intensity vs. k_{ISC}. ($k_{\mathrm{S}} = 1.0 \times 10^7\ \mathrm{s}^{-1}$, $k_{\mathrm{T}} = 2.0 \times 10^7\ \mathrm{s}^{-1}$, $k_0 = 1.0 \times 10^9\ \mathrm{s}^{-1}$, $E/k_{\mathrm{B}} = 1000$ K, and $k_{\mathrm{ESR}} = 1.0 \times 10^7\ \mathrm{s}^{-1}$).

5-5-7. Quantum Mechanical Simulations of the EDMR spectra

Quantum mechanical simulations using the stochastic Liouville equation were performed to calculate accurately the effects of the electron spin resonance due to the microwave rotational field and intersystem crossing due to the Δg mechanism. To simulate the observed EDMR behaviour quantitatively and to clarify the excited-state dynamics, the kinetic model of the mechanism shown in **Scheme 5-1** was formulated in the quantum mechanics utilising the stochastic Liouville equation of the density matrices. This is given by:

$$\begin{aligned}\frac{\mathrm{d}\boldsymbol{\rho}_{\mathrm{eh}}}{\mathrm{d}t} = I_0\langle|\boldsymbol{\Lambda}_S|\rangle - \frac{k_{\mathrm{dis}}}{2}(\boldsymbol{\rho}_{\mathrm{eh}}\boldsymbol{\Lambda}_S + \boldsymbol{\Lambda}_S\boldsymbol{\rho}_{\mathrm{eh}}) - \frac{k_{\mathrm{dis}}}{2}(\boldsymbol{\rho}_{\mathrm{eh}}\boldsymbol{\Lambda}_T + \boldsymbol{\Lambda}_T\boldsymbol{\rho}_{\mathrm{eh}}) \\ - \frac{k_{\mathrm{S}}}{2}(\boldsymbol{\rho}_{\mathrm{eh}}\boldsymbol{\Lambda}_S + \boldsymbol{\Lambda}_S\boldsymbol{\rho}_{\mathrm{eh}}) - \frac{k_{\mathrm{T}}}{2}(\boldsymbol{\rho}_{\mathrm{eh}}\boldsymbol{\Lambda}_T + \boldsymbol{\Lambda}_T\boldsymbol{\rho}_{\mathrm{eh}}) \\ - \frac{i}{\hbar}\left[\boldsymbol{H}_{\mathrm{eh}} + \boldsymbol{H}_{\mathrm{eh}}^{M.W.}, \boldsymbol{\rho}_{\mathrm{eh}}\right],\end{aligned} \tag{5.36}$$

$$\boldsymbol{H}_{\mathrm{eh}} = \mu_B\boldsymbol{B}\cdot\boldsymbol{g}_e\cdot\boldsymbol{S}_{\boldsymbol{e}} + \mu_B\boldsymbol{B}\cdot\boldsymbol{g}_h\cdot\boldsymbol{S}_{\boldsymbol{h}}, \tag{5.37}$$

$$\boldsymbol{H}_{\mathrm{eh}}^{M.W.} = 2\mu_B\boldsymbol{B}_{\mathbf{1}}\cdot\boldsymbol{g}_e\cdot\boldsymbol{S}_{\boldsymbol{e}}\cos(\omega t) + 2\mu_B\boldsymbol{B}_{\mathbf{1}}\cdot\boldsymbol{g}_h\cdot\boldsymbol{S}_{\boldsymbol{h}}\cos(\omega t), \tag{5.38}$$

where $\boldsymbol{\rho}_{\mathrm{eh}}$ is the density matrix of the e–h pair. The first term, $I_0\langle|\boldsymbol{\Lambda}_S|\rangle$, on the right-hand side represents the selective population to $|S\rangle$ of the e–h pair, states from the singlet excited state, and $|S_1\rangle$ by continuous photoirradiation. $\boldsymbol{\Lambda}_S$ and $\boldsymbol{\Lambda}_T$ are the projection operators to the doublet and triplet states in the e–h pair, respectively. They are given by:

$$\boldsymbol{\Lambda}_S = |S\rangle\langle S|, \tag{5.39}$$

and

$$\boldsymbol{\Lambda}_T = \sum_i |T_i\rangle\langle T_i|, \tag{5.40}$$

where, $\boldsymbol{H}_{\mathrm{eh}}$ and $\boldsymbol{H}_{\mathrm{eh}}^{M.W.}$ are the spin Hamiltonian of the e–h pair and that of the interaction with the applied microwave, respectively. The $\mu_{\mathrm{B}}\boldsymbol{B}\cdot\boldsymbol{g}_e\cdot\boldsymbol{S}_{\boldsymbol{e}}$ and $\mu_{\mathrm{B}}\boldsymbol{B}\cdot\boldsymbol{g}_h\cdot\boldsymbol{S}_{\boldsymbol{h}}$ are the Zeeman interactions with the external magnetic field ($\boldsymbol{B}$), $2\mu_{\mathrm{B}}\boldsymbol{B}_{\mathbf{1}}\cdot\boldsymbol{g}_e\cdot$

$\boldsymbol{S_e}\cos(\omega t)$ and $2\mu_B\boldsymbol{B_1}\cdot\boldsymbol{g}_h\cdot\boldsymbol{S_h}\cos(\omega t)$ are the interactions between the e–h pair and the oscillating microwave with angular frequency (ω), respectively. The rate constant of the field-induced radical-pair intersystem crossing (k_{ISC}), which induces S-T$_0$ mixing, is assumed to occur via the Δg mechanism.

It should be noted that the density matrix and the Hamiltonians depend on θ, ϕ, φ, B, and B_1. Here, θ, ϕ, and φ are the Eularian angles depicting the rotation of the g tensors from the molecular frame (X, Y, Z) to the laboratory frame (x, y, z) denoted by the external magnetic field (// z-axis) and the microwave field (// x-axis). B and B_1 are the magnetic flux densities of the external static magnetic field and microwave, respectively. In **Eqn. 5.36–5.38**, the weakly coupled basis representation (WC) was chosen, in which the basis k_{et} vectors were written as $|S_e, m_e\rangle\,|S_h, m_h\rangle$.

To calculate the magnetic resonance effect, we moved from the laboratory frame to the rotating frame with the angular frequency (ωt) of the microwave. In the rotating frame, this Liouville equation can be obtained as follows:

$$
\begin{aligned}
\frac{\mathrm{d}\boldsymbol{\rho}_{\mathrm{eh}}^{\boldsymbol{rot}}}{\mathrm{d}t} = I_0\langle|\boldsymbol{\Lambda}_S|\rangle &- \frac{k_{\mathrm{dis}}}{2}(\boldsymbol{\rho}_{\mathrm{eh}}^{\boldsymbol{rot}}\boldsymbol{\Lambda}_S + \boldsymbol{\Lambda}_S\boldsymbol{\rho}_{\mathrm{eh}}^{\boldsymbol{rot}}) - \frac{k_{\mathrm{dis}}}{2}(\boldsymbol{\rho}_{\mathrm{eh}}^{\boldsymbol{rot}}\boldsymbol{\Lambda}_T + \boldsymbol{\Lambda}_T\boldsymbol{\rho}_{\mathrm{eh}}^{\boldsymbol{rot}}) \\
&- \frac{k_{\mathrm{S}}}{2}(\boldsymbol{\rho}_{\mathrm{eh}}^{\boldsymbol{rot}}\boldsymbol{\Lambda}_{\mathbf{S}} + \boldsymbol{\Lambda}_S\boldsymbol{\rho}_{\mathrm{eh}}^{\boldsymbol{rot}}) - \frac{k_{\mathrm{T}}}{2}(\boldsymbol{\rho}_{\mathrm{eh}}^{\boldsymbol{rot}}\boldsymbol{\Lambda}_T + \boldsymbol{\Lambda}_T\boldsymbol{\rho}_{\mathrm{eh}}^{\boldsymbol{rot}}) \\
&- \frac{i}{\hbar}\left[\boldsymbol{H}_{\mathrm{eh}}^{\boldsymbol{rot}} + \boldsymbol{H}_{\mathrm{eh}}^{M.W.,rot}, \boldsymbol{\rho}_{\mathrm{eh}}^{\boldsymbol{rot}}\right] \\
&+ (Spin\ Relaxation\ Effects),
\end{aligned}
\tag{5.41}
$$

and the spin Hamiltonians are expressed as follows:

$$
\boldsymbol{H}_{\mathrm{eh}}^{\boldsymbol{rot}} + \boldsymbol{H}_{\mathrm{eh}}^{M.W.,rot} = \boldsymbol{AA} + \boldsymbol{BB}e^{i\omega t} + \boldsymbol{CC}e^{-i\omega t} + \boldsymbol{DD}e^{2i\omega t} + \boldsymbol{EE}e^{-2i\omega t}\,, \tag{5.42}
$$

where $\boldsymbol{AA}$ – $\boldsymbol{EE}$ are given by:

$$
\begin{aligned}
\boldsymbol{AA} = (g_{zz}^e\mu_B B_0 - \hbar\omega)S_z^e& \\
&+ \frac{\mu_B B_1}{2}\{(g_{xx}^e - ig_{xy}^e)S_+^e + (g_{xx}^e + ig_{xy}^e)S_-^e\} + (g_{zz}^h\mu_B B_0 \\
&- \hbar\omega)S_z^h + \frac{\mu_B B_1}{2}\{(g_{xx}^h - ig_{xy}^h)S_+^h + (g_{xx}^h + ig_{xy}^h)S_-^h\}
\end{aligned}
\tag{5.43}
$$

$$\boldsymbol{BB} = \frac{\mu_B B_1}{2}\left\{\left(g^e_{xz} - i g^e_{yz}\right)S^e_+ + \left(g^h_{xz} - i g^h_{yz}\right)S^h_+\right\} + g^e_{xz}\mu_B B_1 S^e_z + g^h_{xz}\mu_B B_1 S^h_z \tag{5.44}$$

$$\boldsymbol{CC} = \frac{\mu_B B_1}{2}\left\{\left(g^e_{xz} + i g^e_{yz}\right)S^e_- + \left(g^h_{xz} + i g^h_{yz}\right)S^h_-\right\} + g^e_{xz}\mu_B B_1 S^e_z + g^h_{xz}\mu_B B_1 S^h_z \tag{5.45}$$

$$\boldsymbol{DD} = \frac{\mu_B B_1}{2}\left\{\left(g^e_{xx} - i g^e_{xy}\right)S^e_+ + \left(g^h_{xx} - i g^h_{xy}\right)S^h_+\right\} \tag{5.46}$$

$$\boldsymbol{EE} = \frac{\mu_B B_1}{2}\left\{\left(g^e_{xx} + i g^e_{xy}\right)S^e_- + \left(g^h_{xx} + i g^h_{xy}\right)S^h_-\right\}, \tag{5.47}$$

In the e–h pairs, the anisotropy of the $\boldsymbol{g}$ tensors is small. Therefore, only the $\boldsymbol{AA}$ term, which is time-independent, is addressed below because the non-secular terms $\boldsymbol{BB}$, $\boldsymbol{CC}$, $\boldsymbol{DD}$, and $\boldsymbol{EE}$ in **Eqn. 5.42**. can be neglected. The rate equation of **Eqn. 5.41** was rewritten in the Liouville space as follows:

$$\frac{\mathrm{d}}{\mathrm{d}t}\boldsymbol{\rho}^{\boldsymbol{L,rot}}_{\mathrm{eh}} = I_0\langle|\boldsymbol{\Lambda}_{\mathbf{S}}|\rangle - \boldsymbol{L}_{\mathrm{eh}}\boldsymbol{\rho}^{\boldsymbol{L,rot}}_{\mathrm{eh}} + \boldsymbol{\Gamma}\boldsymbol{\rho}^{\boldsymbol{L,rot}}_{\mathrm{eh}}, \tag{5.48}$$

where

$$\boldsymbol{\rho}^{\boldsymbol{L,rot}}_{\mathrm{eh}}(t) = \begin{pmatrix} \rho^{rot}(t)_{11} \\ \rho^{rot}(t)_{12} \\ \vdots \end{pmatrix}, \tag{5.49}$$

and

$$\begin{aligned}\boldsymbol{L}_{\mathrm{eh}} = {} & \frac{k_{\mathrm{dis}}}{2}(\boldsymbol{\Lambda}_{\mathbf{S}}\otimes\boldsymbol{E} + \boldsymbol{E}\otimes\boldsymbol{\Lambda}^*_{\mathbf{S}}) + \frac{k_{\mathrm{dis}}}{2}(\boldsymbol{\Lambda}_{\mathbf{T}}\otimes\boldsymbol{E} + \boldsymbol{E}\otimes\boldsymbol{\Lambda}^*_{\mathbf{T}}) + \frac{k_{\mathrm{S}}}{2}(\boldsymbol{\Lambda}_{\mathbf{S}}\otimes\boldsymbol{E} + \boldsymbol{E}\otimes\boldsymbol{\Lambda}^*_{\mathbf{S}}) \\ & + \frac{k_{\mathrm{T}}}{2}(\boldsymbol{\Lambda}_{\mathbf{T}}\otimes\boldsymbol{E} + \boldsymbol{E}\otimes\boldsymbol{\Lambda}^*_{\mathbf{T}}) - \frac{i}{\hbar}(\boldsymbol{AA}\otimes\boldsymbol{E} - \boldsymbol{E}\otimes\boldsymbol{AA}^*).\end{aligned} \tag{5.50}$$

Here, $\boldsymbol{\Gamma}$ is the spin-relaxation matrix and $\boldsymbol{E}$ is the unit matrix. The spin-relaxation matrix can be expressed using the eigenfunction representation of $\boldsymbol{H}_{\mathrm{eh}}$ as follows:

$$\boldsymbol{\Gamma} = \boldsymbol{\Gamma}^{\boldsymbol{SL}} + \boldsymbol{\Gamma}^{\boldsymbol{PM}} \tag{5.51}$$

$$\boldsymbol{\Gamma}^{\boldsymbol{SL}} = \frac{1}{T_1}\begin{pmatrix} \frac{1}{Z}\exp(-\frac{E_1}{k_\mathrm{B}}T) \\ 0 \\ 0 \\ 0 \\ \frac{1}{Z}\exp(-\frac{E_2}{k_\mathrm{B}}T) \\ 0 \\ \vdots \\ \vdots \\ \frac{1}{Z}\exp(-\frac{E_4}{k_\mathrm{B}}T) \end{pmatrix} \langle E_{\boldsymbol{L}}| - \frac{1}{T_1}\begin{pmatrix} 1 & 0 & 0 & 0 & 0 & 0 & \cdots & \cdots & 0 \\ 0 & 0 & 0 & 0 & 0 & 0 & \cdots & \cdots & 0 \\ 0 & 0 & 0 & 0 & 0 & 0 & \cdots & \cdots & 0 \\ 0 & 0 & 0 & 0 & 0 & 0 & \cdots & \cdots & 0 \\ 0 & 0 & 0 & 0 & 0 & 0 & \cdots & \cdots & 0 \\ 0 & 0 & 0 & 0 & 0 & 1 & \cdots & \cdots & 0 \\ \vdots & \vdots & \vdots & \vdots & \vdots & \vdots & \ddots & & \vdots \\ \vdots & \vdots & \vdots & \vdots & \vdots & \vdots & & \ddots & \vdots \\ 0 & 0 & 0 & 0 & 0 & 0 & \cdots & \cdots & 1 \end{pmatrix} \tag{5.52}$$

and

$$\boldsymbol{\Gamma}^{\boldsymbol{PM}} = -\frac{1}{T_M}\begin{pmatrix} 0 & 0 & 0 & 0 & 0 & 0 & \cdots & \cdots & 0 \\ 0 & 1 & 0 & 0 & 0 & 0 & \cdots & \cdots & 0 \\ 0 & 0 & 1 & 0 & 0 & 0 & \cdots & \cdots & 0 \\ 0 & 0 & 0 & 1 & 0 & 0 & \cdots & \cdots & 0 \\ 0 & 0 & 0 & 0 & 1 & 0 & \cdots & \cdots & 0 \\ 0 & 0 & 0 & 0 & 0 & 0 & \cdots & \cdots & 0 \\ \vdots & \vdots & \vdots & \vdots & \vdots & \vdots & \ddots & & \vdots \\ \vdots & \vdots & \vdots & \vdots & \vdots & \vdots & & \ddots & \vdots \\ 0 & 0 & 0 & 0 & 0 & 0 & \cdots & \cdots & 0 \end{pmatrix}. \tag{5.53}$$

Here, Z is partition function. $\boldsymbol{\Gamma}^{\boldsymbol{SL}}$ and $\boldsymbol{\Gamma}^{\boldsymbol{PM}}$ are the spin-lattice relaxation and phase-relaxation superoperators, respectively, written in the eigenfunction representation. The $\boldsymbol{\Gamma}^{\boldsymbol{SL}}$ acts on the 1, 6, 11, and 16 th elements of $\boldsymbol{\rho}_{\mathrm{eh}}^{\boldsymbol{L,rot}}$ and $\boldsymbol{\Gamma}^{\boldsymbol{PM}}$ acts on the other elements of $\boldsymbol{\rho}_{\mathrm{eh}}^{\boldsymbol{L,rot}}$. $\langle E_{\boldsymbol{L}}|$ is the row vector representation of $\boldsymbol{E}$ expressed in the Liouville space, which led to $\langle E_{\boldsymbol{L}}|\boldsymbol{\rho}_{\mathrm{eh}}^{\boldsymbol{L,rot}} = Tr\{\boldsymbol{\rho}_{\mathrm{eh}}^{\boldsymbol{L,rot}}\}$. All operators and density matrices in **Eqn. 5.49**, which are written in the WC basis representation, are transformed to those in the eigenfunction representation using the unitary transformation matrix, $U_{\mathrm{WC}\rightarrow eigen}$, obtained from the eigenfunctions of $\boldsymbol{H}_{\mathrm{eh}}$ in the WC basis representation. In the steady-state approximation of $d\boldsymbol{\rho}_{\mathrm{eh}}^{\boldsymbol{L,rot}}/dt = 0$, the solution of the density matrix is given by:

$$\boldsymbol{\rho}_{\mathrm{eh}}^{L,rot} = I_0(\boldsymbol{L}_{\mathrm{eh}} - \boldsymbol{\Gamma})^{-\boldsymbol{1}}\langle|\boldsymbol{\Lambda}_S|\rangle. \tag{5.54}$$

The steady-state density matrix of the e–h pairs, $\boldsymbol{\rho}_{\mathrm{eh}}$, can be obtained directly from $\boldsymbol{\rho}_{\mathrm{eh}}^{L,rot}$. The density matrix and Hamiltonians depend on θ, ϕ, φ, B, and B_1, although they have been omitted from the above equations. In the current study, the EDMR is caused by the change in the efficiency of charge carrier generation from the e–h pairs. The efficiency, in which the external magnetic field is applied to the (θ, ϕ) direction in the principal axes (X, Y, Z), can be expressed as follows:

$$\emptyset(\theta, \phi, \varphi, B, B_1) = (k_{\mathrm{dis}}/I_0)Tr\{\boldsymbol{\rho}_{\mathrm{eh}}(\theta, \phi, \varphi, B, B_1)\}. \tag{5.55}$$

Because the molecules are oriented randomly in the sample, the averaged efficiency is given by:

$$\langle\emptyset(B, B_1)\rangle = \frac{1}{V}\int_0^{\pi}\int_0^{2\pi}\int_0^{\pi}\emptyset(\theta, \phi, \varphi, B, B_1)\sin\theta\,\mathrm{d}\theta\mathrm{d}\phi\mathrm{d}\varphi. \tag{5.56}$$

The relative intensity of the EDMR for the photocurrent intensity can be calculated using the averaged efficiency as follows:

$$I_{\mathrm{EDMR}} = \frac{\langle\emptyset(B, B_1)\rangle - \langle\emptyset(B, 0)\rangle}{\langle\emptyset(B, 0)\rangle}, \tag{5.57}$$

which can be used to compare the simulated and observed EDMR intensity (1.3%), as shown in **Fig. 5-6**. The temperature dependence of the EDMR was calculated using **Eqn. 5.56** as follows:

$$I_{\mathrm{EDMR}} \propto I_0\{\langle\emptyset(B, B_1)\rangle - \langle\emptyset(B, 0)\rangle\}. \tag{5.56}$$

Figures 5-20 and **5-21** show the simulated Δg dependence and B_1 dependence of the EDMR intensity using the quantum mechanical simulations, respectively. For the slight differences in the g-values, the EDMR behaviour is almost identical.

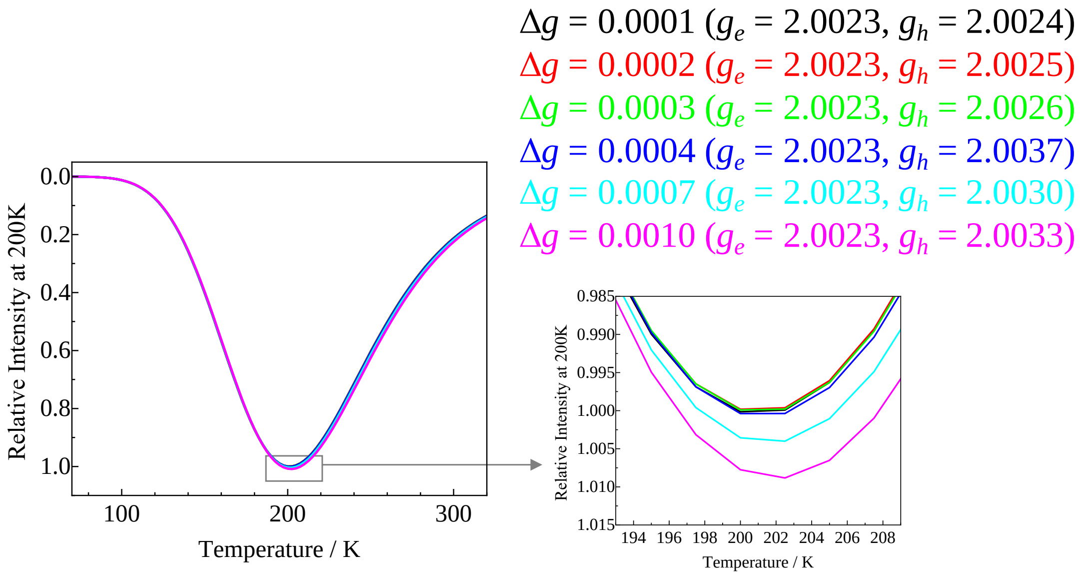

Fig. 5-20. The Δg dependence of the EDMR behaviour. ($k_S = 3.0 \times 10^6$ s^{-1}, $k_T = 1.5 \times 10^7$ s^{-1}, $k_0 = 1.0 \times 10^9$ s^{-1}, $E/k_B = 1103$ K, and $B_1 = 0.050$ mT.)

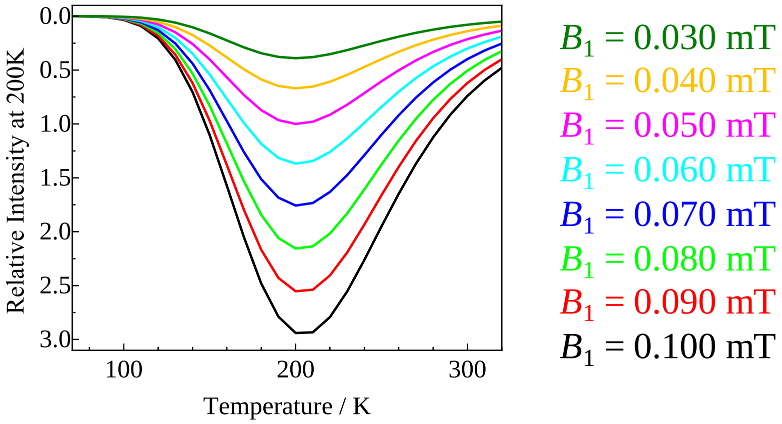

Fig. 5-21. The B_1 dependence of the EDMR behaviour. ($k_S = 3.0 \times 10^6$ s^{-1}, $k_T = 1.5 \times 10^7$ s^{-1}, $k_0 = 1.0 \times 10^9$ s^{-1}, $E/k_B = 1103$ K, $g_e = 2.0023$ and $g_h = 2.0025$)

Using **Eqn. 5.56**, the simulation reproduced the observed EDMR behaviour, as shown in **Fig. 5-22**, when the rate constants and activation energy are $k_S = 3.0 \times 10^6\ \mathrm{s}^{-1}$, $k_T = 1.5 \times 10^7\ \mathrm{s}^{-1}$, $k_0 = 1.0 \times 10^9\ \mathrm{s}^{-1}$, and $E/k_B = 1103$ K, respectively, and the g values and microwave field are $g_e = 2.0023$, $g_h = 2.0025$, and $B_1 = 0.050$ mT, respectively. Thus, the temperature-dependent EDMR behaviour was successfully simulated by solving the stochastic Liouville equation numerically under steady-state conditions ($\mathrm{d}\boldsymbol{\rho}_{eh}/\mathrm{d}t = 0$). Under this condition, the change in intensity of the EDMR was approximately −1.3% at 200 K, which was in agreement with the experimental result obtained via direct measurements. An E/k_B value of 1103 K was used for the simulation, which was determined using least-squares fitting, as shown in **Fig. 5-3**. The *g*-value of the electron was assumed to be the same as that of the free electron ($g_e = 2.0023$) and the *g*-value of the hole used was the literature value of the TIPS-Pn cation ($g_h = 2.0025$).[106] There is little change in the EDMR due to small differences in *g*-values. Although there is ambiguity regarding the choice of kinetic constants k_S, k_T, and k_0 because their experimental values are unknown. The relative ratios of rate constant (k_S, k_T, k_{ISC}, k_{ESR} and k_0) are relevant because the shape of the simulated curves and the sign of the EDMR depend on those ratios. Under the limitation of $k_{S(T)} + k_{dis} = k_{S(T)} + k_0 \exp(-E/k_BT) = 1.5 \times 10^7\ \mathrm{s}^{-1}$ (at $T = 80$ K), $4.3 \times 10^7\ \mathrm{s}^{-1}$ (at $T = 310$ K) $< 8.6 \times 10^7\ \mathrm{s}^{-1}$ (from linewidth), and $k_S < k_T$ (the condition to give a negative sign for the EDMR), an appropriate set of k_S, k_T, and k_0 values were chosen (not a unique solution). These rate constants were comparable to that of the kinetic constants used in the photogenerated radical pairs in the organic solution.[116] Actually, in the EDMR studies of solution systems, the lifetime of radical pairs (e-h pairs) is determined by transient pulse EDMR technique.[116] Furthermore, the combination to the time-resolved EDMR will give the estimation of the life-time of the e-h pair.

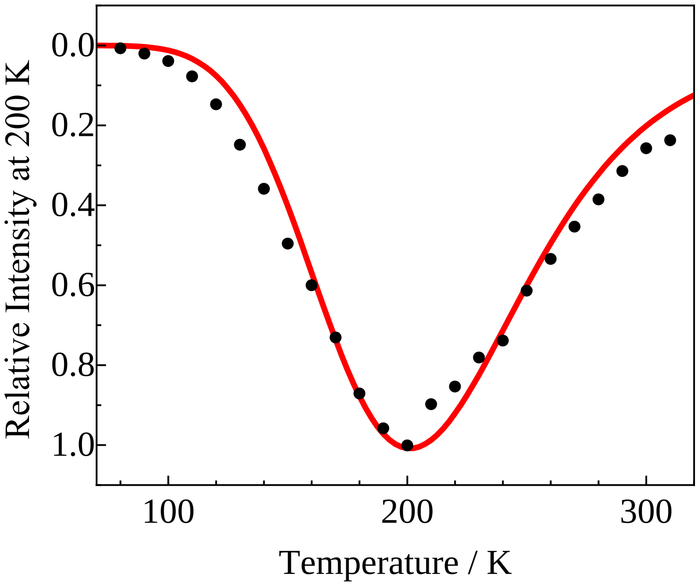

Fig. 5-22. Temperature dependence of the integral signal intensity (black dots) and the simulation curve using **Eqn. 5.56** (red curve; $k_S = 3.0 \times 10^6\ s^{-1}$, $k_T = 1.5 \times 10^7\ s^{-1}$, $k_0 = 1.0 \times 10^9\ s^{-1}$, and $E/k_B = 1103$ K, $g_e = 2.0023$, $g_h = 2.0025$, and $B_1 = 0.050$ mT).

5-6. Summary

In conclusion, TIPS-Pn VVD films have been evaluated by studying the temperature dependence of the photocurrent and EDMR. The prepared TIPS-Pn VVD films were found to be polycrystalline films using absorption spectroscopy. Photocurrent and EDMR measurements in air and in the N_2 atmosphere indicate that atmospheric oxygen is the source of the traps observed in the band gap. The temperature dependence of the photocurrent and EDMR behaviour were well interpreted through the intermediate e–h pair, which was generated from the singlet excited state of TIPS-Pn to the photogenerated carrier. The activation energy from the e–h pair to the charge carrier was determined to be $E/k_B = 1103$ K based on the temperature dependence of the photocurrent. The EDMR spectra can be decomposed into two components (one is due to a high-mobility e–h pair and the other is a low-mobility e–h pair, which may be attributed to the different pathways of conduction) using the out-of-phase signals in the quadrature detection with a lock-in amplifier. The EDMR spectrum obtained via direct detection without a lock-in amplifier shows a reduction in the photocurrent of ~1.3% at 200 K. This corresponds to the maximum intensity. The linewidth and intensity of the EDMR depends on the temperature. The linewidth of the low-mobility e–h pairs is almost independent of temperature, while the linewidths of the high-mobility e–h pairs show broadening due to relaxation at temperatures > 200 K. The spectral intensity of the EDMR signal increased from 80 to 200 K and then decreased from 200 to 310 K. The temperature dependence of the EDMR was calculated using quantum mechanical simulations of the excited state and carrier dynamics of the e–h pair as well as the analytical solution for the kinetic rate equation. Therefore, the mechanism of the photoinduced carrier generation and the spin dynamics in the TIPS-Pn VVD film (a representative photostable pentacene derivative) were elucidated in detail, which will provide useful information for the design of efficient devices utilizing pentacene derivatives or similar organic semiconductor materials.

Chapter 6.

Conclusion

In this dissertation, a protocol used to evaluate the mechanism of photocurrent generation in organic thin films has been established. Weak CT complexes, such as Py/DMPI and Py/PMDA, have been chosen as the target compounds to establish a protocol used to evaluate the mechanism. The excited-state and carrier dynamics related to photocurrent generation were clarified using a combination of several measurements. The carrier generation process via weakly interacting spin pairs was revealed by measuring the MFE of the photocurrent and the temperature dependence of the photocurrent, TRESR, and EDMR. Based on this approach, the protocol was applied to TIPS-Pn VVD film. Thus, the temperature dependence of the photocurrent and EDMR measurements, and quantum mechanical simulations of the excited state dynamics of a weakly interacting radical pair were carried out to clarify the mechanism of the photocurrent generation of the TIPS-Pm. The photocurrent generation mechanism and excited state dynamics in the TIPS-Pn VVD film were clarified in detail. The main results obtained from this thesis work are summarized below.

The photocurrent and MC effect were measured in Py/DMPI and Py/PMDA VVD films. The MC effect increases by ~1.2% at 200 mT in the VVD films. The MC behaviour is reasonably explained by assuming two types of collision mechanisms (DD and TD pair mechanisms), which occur between the geminate e–h pair as well as between the trapped triplet excitons and carrier (^{3}ex$_t$–^{2}c or ^{3}cs$_t$–^{2}c). The unknown parameters necessary for the simulation of the excited stare dynamics related to photocurrent generation were evaluated using X-ray analysis, MO calculations, TRESR of Py/DMPI and Py/PMDA, and EDMR. In the simulation of the DD pair mechanism, the maximum MC effect was calculated to be < 3%, whereas in the simulation of the TD pair mechanism, the maximum MC effect was calculated to be > 500% depending on the specific conditions used. This simulation result for the TD-pair mechanism may shed light on the origin of the giant

MFE. The trapped triplet excitons and weakly interacting e–h pairs assumed in this simulation were observed by TRESR and EDMR. The mobile triplet exciton was observed from TRESR for the Py/DMPI single crystals and temperature variation measurements showed that many triplet excitons were trapped even at room temperature. The weakly interacting e–h pair was detected using the EDMR of the Py/DMPI VVD film. The temperature variation measurements determined the activation energy from the electron-hole pairs to mobile carriers.

The carrier generation process of TIPS-Pn was clarified by studying the temperature dependence of the photocurrent and EDMR. Using the out-of-phase signal measurement in the quadrature detection with a lock-in amplifier, the EDMR spectra can be decomposed into two components in which one is due to a high-mobility e–h pair and the other is a low-mobility e–h pair. Their mobility difference may be attributed to the different pathways of conduction. The EDMR intensity depends on the temperature. The spectral intensity of the EDMR signal increased from 80 to 200 K and then decreased from 200 to 310 K. Direct detection of the EDMR signal using the picoammeter instead of the lock-in amplifier showed that ~1.3% of the photocurrent was decreased at 200 K. The temperature dependence of the EDMR was simulated using quantum mechanical simulations of the excited state and carrier dynamics of the e–h pair as well as the analytical solution of the kinetic rate equation. The simulation reproduced the observed temperature dependence of the EDMR signal intensity. This simulation revealed that the weakly interacting e–h pair is first generated from the photoexcited state in the TIPS-Pn VVD film and mobile carriers are generated from the e–h pairs upon thermal excitation.

The methods used to measure the change in the physical properties due to a magnetic field or ESR transitions are a non-destructive and selective way to observe the photo-carrier generation dynamics. The methodology established in this paper may lead to a useful approach to evaluate the carrier dynamics of organic semiconductor thin-film devices such as OLEDs and OSCs.

Appendix.

Analysis of the Temperature Dependence of EDMR on Py/DMPI using the S-Born Model

In **Chapter 5**, the temperature dependence of EDMR is studied in detail using the TIPS-Pn film. In this **Appendix**, the temperature dependence of EDMR on the Py/DMPI film obtained in **Chapter 4** is analysed using the S-Born model. The activation energy of the carrier generation from the e–h pair was used $E/k_B = 1507$ K which is the value estimated from the temperature dependence of the photocurrent on the Py/DMPI film. Because direct detection has not been measured of the EDMR signal change using the picoammeter instead of the lock-in amplifier, the respective transition rates cannot be determined correctly. However, the rate constants of Py/DMPI are estimated of transition from the ^{1}(e–h) pair to the ground state and from the ^{3}(e–h) pair to the excited triplet state are estimated as $k_S = 1.0 \times 10^8$ s^{-1} and $k_T = 1.7 \times 10^8$ s^{-1} in **Chapter 3**. Although this value is not unique, it was used as is in this simulation. The signal sign was assumed to be negative as well as for TIPS-Pn thin films. When other parameters are assumed $k_0 = k_{ESR} = k_{ISC} = 1.0 \times 10^7$ s^{-1}, the simulation curve is obtained shown in **Fig. A-1**. It should be noted that, these parameters other than activation energy may not be appropriate. The simulation curve is a reproduction of the approximation obtained by the temperature dependent EDMR. Hence, the S-born model discussed in **Chapter 5** may be a general model to describe temperature dependence EDMR behaviour.

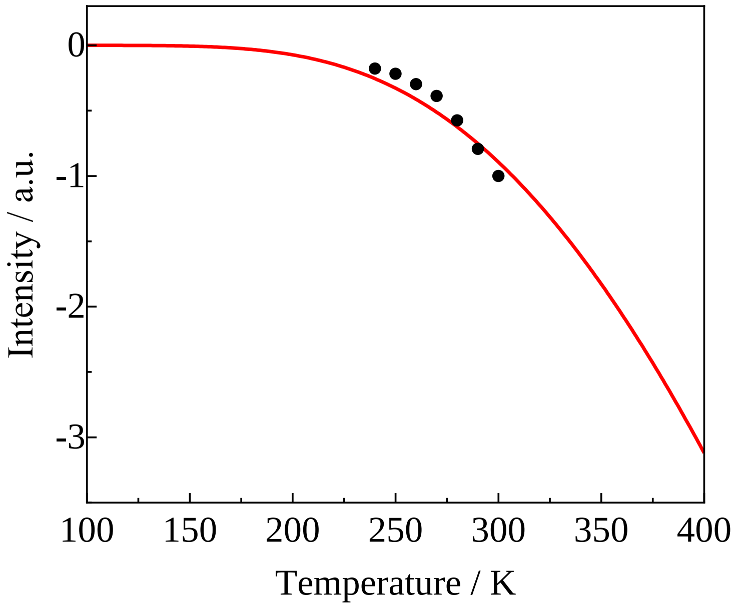

Fig. A-1. Temperature dependence of the integral signal intensity of Py/DMPI (black dots) and the simulation curve using **Eqn. 5.20** (red curve; $E/k_B = 1507$ K, $k_S = 1.0 \times 10^8$ s^{-1}, $k_T = 1.7 \times 10^8$ s^{-1}, $k_0 = 1.0 \times 10^7$ s^{-1}, $k_{ESR} = 1.0 \times 10^7$ s^{-1}, and $k_{ISC} = 1.0 \times 10^7$ s^{-1}).

References

1. N. Stingelin-Stutzmann, E. Smits, H. Wondergem, C. Tanase, P. Blom, P. Smith and D. de Leeuw, *Nat. Mater.*, 2005, **4**, 601.
2. B. Y. Ahn, E. B. Duoss, M. J. Motala, X. Guo, S. I. Park, Y. Xiong, J. Yoon, R. G. Nuzzo, J. A. Rogers and J. A. Lewis, *Science*, 2009, **323**, 1590.
3. H. Klauk, *Organic Electronics: Materials, Manufacturing and Applications*, 2006.
4. H. Klauk, *Organic Electronics II More Materials and Applications*, 2012.
5. K. Marumoto, S. Kuroda, T. Takenobu and Y. Iwasa, *Phys. Rev. Lett.*, 2006, **97**, 256603.
6. J. Tsurumi, H. Matsui, T. Kubo, R. Häusermann, C. Mitsui, T. Okamoto, S. Watanabe and J. Takeya, *Nat. Phys.*, 2017, **13**, 994.
7. S.-J. Wang, D. Venkateshvaran, M. R. Mahani, U. Chopra, E. R. McNellis, R. Di Pietro, S. Schott, A. Wittmann, G. Schweicher, M. Cubukcu, K. Kang, R. Carey, T. J. Wagner, J. N. M. Siebrecht, D. P. G. H. Wong, I. E. Jacobs, R. O. Aboljadayel, A. Ionescu, S. A. Egorov, S. Mueller, O. Zadvorna, P. Skalski, C. Jellett, M. Little, A. Marks, I. McCulloch, J. Wunderlich, J. Sinova and H. Sirringhaus, *Nat. Electron.*, 2019, **2**, 98.
8. J. McGuire, H. N. Miras, E. Richards and S. Sproules, *Chem. Sci.*, 2019, **10**, 1483.
9. K. Marumoto, T. Fujimori, M. Ito and T. Mori, *Adv. Energy Mater.*, 2012, **2**, 591.
10. T. Nagamori and K. Marumoto, *Adv. Mater.*, 2013, **25**, 2362.
11. G. Sato, D. Son, T. Ito, F. Osawa, Y. Cho and K. Marumoto, *Phys. Status Solidi A*, 2018, **215**, 1700731.
12. H. Matsuoka, M. Retegan, L. Schmitt, S. Hoger, F. Neese and O. Schiemann, *J. Am. Chem. Soc.*, 2017, **139**, 12968.
13. T. Miura, M. Aikawa and Y. Kobori, *J. Phys. Chem. Lett.*, 2014, **5**, 30-35.
14. Y. Kobori, T. Ako, S. Oyama, T. Tachikawa and K. Marumoto, *J. Phys. Chem. C*, 2019, **123**, 13472.
15. H. Hayashi, *Introduction To Dynamic Spin Chemistry*, 2004.
16. H. Sakuragi, M. Sakuragi, T. Mishima, S. Watanabe, M. Hasegawa and K.

Tokumaru, *Chem. Lett.*, 1975, **4**, 231.

17. Y. Tanimoto, H. Hayashi, S. Nagakura, H. Sakuragi and K. Tokumaru, *Chem. Phys. Lett.*, 1976, **41**, 267.
18. G. L. Closs, M. D. E. Forbes and J. R. Norris, *J. Phys. Chem.*, 1987, **91**, 3592.
19. R. Kaptein, *J. Am. Chem. Soc.*, 1972, **94**, 6251.
20. K. Itoh, H. Hayashi and S. Nagakura, *Mol. Phys.*, 1969, **17**, 561.
21. N. Hata, *Chem. Lett.*, 1976, **5**, 547.
22. U. E. Steiner and T. Ulrich, *Chem. Rev.*, 1989, **89**, 51.
23. K. Maeda, K. B. Henbest, F. Cintolesi, I. Kuprov, C. T. Rodgers, P. A. Liddell, D. Gust, C. R. Timmel and P. J. Hore, *Nature*, 2008, **453**, 387.
24. Y. Wang, K. Sahin-Tiras, N. J. Harmon, M. Wohlgenannt and M. E. Flatté, *Phys. Rev. X*, 2016, **6**, 011011.
25. T. D. Nguyen, G. Hukic-Markosian, F. Wang, L. Wojcik, X. G. Li, E. Ehrenfreund and Z. V. Vardeny, *Nature Matererials*, 2010, **9**, 345.
26. T. D. Nguyen, E. Ehrenfreund and Z. V. Vardeny, *Org. Electron.*, 2013, **14**, 1852.
27. M. Cox, P. Janssen, F. Zhu and B. Koopmans, *Phys. Rev. B*, 2013, **88**, 035202.
28. T. Omori, Y. Wakikawa, T. Miura, Y. Yamaguchi, K. Nakayama and T. Ikoma, *J. Phys. Chem. C*, 2014, **118**, 28418.
29. M. Sharnoff, *J. Chem. Phys.*, 1967, **46**, 3263.
30. A. L. Kwiram, *Chem. Phys. Lett.*, 1967, **1**, 272.
31. D. J. Lepine, *Phys. Rev. B*, 1972, **6**, 436.
32. E. L. Frankevich, in *Triplet State ODMR Spectroscopy: Techniques and Applications to Biophysical Systems*, wiley, 1982, chapter 5, 134.
33. V. I. Lesin, V. P. Sakun, A. I. Pristupa and E. L. Frankevich, *Phys. Status Solidi B*, 1977, **84**, 513.
34. E. L. Frankevich, A. I. Pristupa and V. I. Lesin, *Chem. Phys. Lett.*, 1978, **54**, 99.
35. E. L. Frankevich, M. M. Tribel, I. A. Sokolik and A. I. Pristupa, *Phys. Status Solidi B*, 1978, **87**, 373.
36. F. Kraffert, R. Steyrleuthner, C. Meier, R. Bittl and J. Behrends, *Appl. Phys. Lett.*, 2015, **107**, 043302.

37. B. Zerai Tedlla, F. Zhu, M. Cox, B. Koopmans and E. Goovaerts, *Phys. Rev. B*, 2015, **91**, 085309.
38. B. D. Folie, J. B. Haber, S. Refaely-Abramson, J. B. Neaton and N. S. Ginsberg, *J. Am. Chem. Soc.*, 2018, **140**, 2326.
39. W. J. Baker, T. L. Keevers, J. M. Lupton, D. R. McCamey and C. Boehme, *Phys. Rev. Lett.*, 2012, **108**, 267601.
40. S. Hatanaka, K. Kimura, T. Suzuki and K. Kanemoto, *Phys. Rev. Mater.*, 2018, **2**, 115201.
41. K. Iwamoto, Y. Hayakawa, S. Hatanaka, T. Suzuki and K. Kanemoto, *J. Phys. Chem. C*, 2019, **123**, 26116.
42. S. A. J. Thomson, S. C. Hogg, I. D. W. Samuel and D. J. Keeble, *J. Mater. Chem. A*, 2017, **5**, 21926.
43. R. E. Merrifield, P. Avakian and R. P. Groff, *Chem. Phys. Lett.*, 1969, **3**, 155.
44. C. A. P. a. C. G. Hatchard, *Proc. R. Soc. London, Ser. A*, 1962, **269**, 574.
45. P. W. Atkins and G. T. Evans, *Mol. Phys.*, 1975, **29**, 921.
46. B. V. K. V. M. Vozzhennikov, V. P. Krasavin, *Russ. J. Phys. Chem.*, 1977, **51**, 1074.
47. Y. Nakayama, Y. Ichikawa and T. Matsuo, *Bull. Chem. Soc. Jpn.*, 1965, **38**, 1674.
48. J. E. Anthony, J. S. Brooks, D. L. Eaton and S. R. Parkin, *J. Am. Chem. Soc.*, 2001, **123**, 9482.
49. S. S. Kim and S. I. Weissman, *J. Magn. Reson.*, 1976, **24**, 167.
50. W. G. T. J. M. Frisch, B. H. Schlegel, E. G. Scuseria, A. M. Robb, R. J. Cheeseman, G. Scalmani, V. Barone, B. Mennucci, A. G. Petersson, H. Nakatsuji,M. Caricato, X. Li, P. H. Hratchian, F. A. Izmaylov, J. Bloino, G. Zheng, L. J. Sonnenberg, M. Hada, M. Ehara, K. Toyota, R. Fukuda, J. Hasegawa, M. Ishida, T. Nakajima, Y. Honda, O. Kitao, H. Nakai, T. Vreven, A. J. Montgomery Jr., E. J. Peralta, F. Ogliaro, M. Bearpark, J. J. Heyd, E. Brothers, N. K. Kudin, N. V. Staroverov, R. Kobayashi, J. Normand, K. Raghavachari, A. Rendell, C. J. Burant, S. S. Iyengar, J. Tomasi, M. Cossi, N. Rega, M. J. Millam, M. Klene, E. J. Knox, B. J. Cross, V. Bakken, C. Adamo, J. Jaramillo, R. Gomperts, E. R. Stratmann, O. Yazyev, J. A. Austin, R. Cammi, C. Pomelli, W. J. Ochterski, L. R. Martin, K. Morokuma, G. V. Zakrzewski,

A. G. Voth, P. Salvador, J. J. Dannenberg, S. Dapprich, D. A. Daniels, O. Farkas, B. J. Foresman, V. J. Ortiz, J. Cioslowski J. D. Fox, *Gaussian 09 User's Reference*, 2009.

51. F. Neese, *WIREs Computational Molecular Science*, 2011, **2**, 73.
52. R. Geng, H. M. Luong, T. T. Daugherty, L. Hornak and T. D. Nguyen, *J. Sci.: Adv. Mate. Devices*, 2016, **1**, 256.
53. D. Nikiforov, B. Khachatryan, J. Tilchin, E. Lifshitz, N. Tessler and E. Ehrenfreund, *Phys. Rev. B*, 2018, **98**, 235204.
54. R. Shoji, T. Omori, Y. Wakikawa, T. Miura and T. Ikoma, *ACS Omega*, 2018, **3**, 9369.
55. R. Shoji, T. Miura and T. Ikoma, *Org. Electron.*, 2019, **75**, 105383.
56. E. Ehrenfreund and Z. V. Vardeny, *Isr. J. Chem.*, 2012, **52**, 552.
57. L. I. N. B. S. Yakovlev, E. L. Frankevich, *Zh. Eksp. Teor. Fiz.* , 1970, **58**, 1574.
58. A. Altomare, M. C. Burla, M. Camalli, G. L. Cascarano, C. Giacovazzo, A. Guagliardi, A. G. G. Moliterni, G. Polidori and R. Spagna, *J. Appl. Crystallogr.*, 1999, **32**, 115.
59. H. Hayashi, S. Iwata and S. Nagakura, *J. Chem. Phys.*, 1969, **50**, 993.
60. H. Möhwald and A. Böhm, *Z. Naturforsch., A: Phys. Sci.*, 1976, **31**, 1324.
61. J. Krzystek and J. U. Von Schütz, in *Adv. Chem. Phys.*, *Triplet Excitons in Weak Organic Charge-Transfer Crystals*, 2007, chapter 2, 167.
62. P. Krebs, E. Sackmann and J. Schwarz, *Chem. Phys. Lett.*, 1971, **8**, 417.
63. R. Z. Sagdeev, Y. N. Molin, K. M. Salikhov, T. V. Leshina, M. A. Kamha and S. M. Shein, *Org. Magn. Reson.*, 1973, **5**, 603.
64. Ö. Mermer, G. Veeraraghavan, T. L. Francis, Y. Sheng, D. T. Nguyen, M. Wohlgenannt, A. Köhler, M. K. Al-Suti and M. S. Khan, *Phys. Rev. B*, 2005, **72**, 205202.
65. F. Ito, T. Ikoma, K. Akiyama, Y. Kobori and S. Tero-Kubota, *J. Am. Chem. Soc.*, 2003, **125**, 4722.
66. M. Wakasa, M. Kaise, T. Yago, R. Katoh, Y. Wakikawa and T. Ikoma, *J. Phys. Chem. C*, 2015, **119**, 25840.

67. W. Siebrand, *J. Chem. Phys.*, 1967, **46**, 440.
68. W. Siebrand, *J. Chem. Phys.*, 1967, **47**, 2411.
69. R. Kubo and K. Tomita, *J. Phys. Soc. Jpn.*, 1954, **9**, 888.
70. P. W. Anderson and P. R. Weiss, *Rev. Mod. Phys.*, 1953, **25**, 269.
71. J. Cohen, *J. Appl. Phys.*, 1957, **28**, 795.
72. N. Karl and J. Ziegler, *Chem. Phys. Lett.*, 1975, **32**, 438.
73. J. Shinar, *Laser & Photonics Reviews*, 2012, **6**, 767.
74. H. Malissa, R. Miller, D. L. Baird, S. Jamali, G. Joshi, M. Bursch, S. Grimme, J. van Tol, J. M. Lupton and C. Boehme, *Phys. Rev. B*, 2018, **97**, 161201.
75. R. Miller, K. J. van Schooten, H. Malissa, G. Joshi, S. Jamali, J. M. Lupton and C. Boehme, *Phys. Rev. B*, 2016, **94**, 214202.
76. S. Biring, Y.-Z. Li, C.-C. Lee, A. Pan, Y.-D. Li, G. Kumar and S.-W. Liu, *Thin Solid Films*, 2017, **636**, 485.
77. O. D. Jurchescu, J. Baas and T. T. M. Palstra, *Appl. Phys. Lett.*, 2004, **84**, 3061.
78. A. N. Aleshin, J. Y. Lee, S. W. Chu, J. S. Kim and Y. W. Park, *Appl. Phys. Lett.*, 2004, **84**, 5383.
79. J. Shi, D.-T. Jiang, J. R. Dutcher and X.-R. Qin, *J. Vac. Sci. Technol. B*, 2015, **33**, 050604.
80. P. M. Fauchet, D. Hulin, R. Vanderhaghen, A. Mourchid and W. L. Nighan, *J. Non-Cryst. Solids*, 1992, **141**, 76.
81. H. Meiling and R. E. I. Schropp, *Appl. Phys. Lett.*, 1997, **70**, 2681.
82. Z. Zhou, L. Ma, D. Guo, X. Zhao, C. Wang, D. Lin, F. Zhang, J. Zhang and Z. Nie, *J. Phys. Chem. C*, 2020, **124**, 14503.
83. W. Shockley and H. J. Queisser, *J. Appl. Phys.*, 1961, **32**, 510.
84. S. Katsuta, D. Miyagi, H. Yamada, T. Okujima, S. Mori, K. Nakayama and H. Uno, *Org. Lett.*, 2011, **13**, 1454.
85. I. Kaur, W. Jia, R. P. Kopreski, S. Selvarasah, M. R. Dokmeci, C. Pramanik, N. E. McGruer and G. P. Miller, *J. Am. Chem. Soc.*, 2008, **130**, 16274.
86. A. Maliakal, K. Raghavachari, H. Katz, E. Chandross and T. Siegrist, *Chem. Mater.*, 2004, **16**, 4980.

87. Y. Kawanaka, A. Shimizu, T. Shinada, R. Tanaka and Y. Teki, *Angew. Chem. Int. Ed.*, 2013, **52**, 6643.
88. A. Shimizu, A. Ito and Y. Teki, *Chem. Commun.*, 2016, **52**, 288.
89. A. Ito, A. Shimizu, N. Kishida, Y. Kawanaka, D. Kosumi, H. Hashimoto and Y. Teki, *Angew. Chem. Int. Ed.*, 2014, **53**, 6715.
90. H. Matsui, A. S. Mishchenko and T. Hasegawa, *Phys. Rev. Lett.*, 2010, **104**, 056602.
91. M. Groesbeck, H. Liu, M. Kavand, E. Lafalce, J. Wang, X. Pan, T. H. Tennahewa, H. Popli, H. Malissa, C. Boehme and Z. V. Vardeny, *Phys. Rev. Lett.*, 2020, **124**, 067702.
92. Y. Tani, Y. Teki and E. Shikoh, *Appl. Phys. Lett.*, 2015, **107**, 242406.
93. Y. Tani, T. Kondo, Y. Teki and E. Shikoh, *Appl. Phys. Lett.*, 2017, **110**, 032403.
94. Y. Tanaka, T. Kono, Y. Teki and E. Shikoh, *IEEE Trans. Magn.*, 2019, **55**, 1.
95. S. Singh and Y. N. Mohapatra, *J. Appl. Phys.*, 2016, **120**, 045501.
96. R. Jia, X. Wu, W. Deng, X. Zhang, L. Huang, K. Niu, L. Chi and J. Jie, *Adv. Funct. Mater.*, 2019, **29**, 1905657.
97. B. J. Walker, A. J. Musser, D. Beljonne and R. H. Friend, *Nat. Chem.*, 2013, **5**, 1019.
98. C. Grieco, G. S. Doucette, R. D. Pensack, M. M. Payne, A. Rimshaw, G. D. Scholes, J. E. Anthony and J. B. Asbury, *J. Am. Chem. Soc.*, 2016, **138**, 16069-.
99. D. Rehm and A. Weller, *Isr. J. Chem.*, 1970, **8**, 259.
100. G. Murtaza, I. Ahmad and J. Wu, *Mater. Sci. Semicond. Process.*, 2015, **34**, 269.
101. S. Matsuda, S. Oyama and Y. Kobori, *Chem. Sci.*, 2020, **11**, 2934.
102. L. Tsetseris and S. T. Pantelides, *Phys. Rev. B*, 2007, **75**, 153202.
103. K. Kanemoto, S. Hatanaka and T. Suzuki, *J. Appl. Phys.*, 2019, **125**.
104. A. M. Portis, *Phys. Rev.*, 1953, **91**, 1071.
105. T. G. Castner, *Phys. Rev.*, 1959, **115**, 1506.
106. S. Schundelmeier, B. Speiser, H. F. Bettinger and R. Einholz, *ChemPhysChem*, 2017, **18**, 2266.
107. T. Minakata, H. Imai, M. Ozaki and K. Saco, *J. Appl. Phys.*, 1992, **72**, 5220.
108. C. D. Dimitrakopoulos and P. R. L. Malenfant, *Adv. Mater.*, 2002, **14**, 99.
109. G. Giri, E. Verploegen, S. C. Mannsfeld, S. Atahan-Evrenk, D. H. Kim, S. Y. Lee,

H. A. Becerril, A. Aspuru-Guzik, M. F. Toney and Z. Bao, *Nature*, 2011, **480**, 504.

110. S. C. Mannsfeld, M. L. Tang and Z. Bao, *Adv. Mater.*, 2011, **23**, 127.
111. S. Schaefer, S. Saremi, J. Behrends, K. Fostiropoulos, K. Lips and W. Harneit, *Phys. Status Solidi B*, 2009, **246**, 2844.
112. K. Fukuda and N. Asakawa, *J. Phys. D: Appl. Phys.*, 2017, **50**, 055102.
113. Y. Nicolas, F. Castet, M. Devynck, P. Tardy, L. Hirsch, C. Labrugère, H. Allouchi and T. Toupance, *Org. Electron.*, 2012, **13**, 1392.
114. K. Seki and K. Marumoto, *Phys. Rev. E*, 2019, **99**, 052115.
115. D. Kaplan, I. Solomon and N. F. Mott, *J. Phys. Lett.*, 1978, **39**, 51.
116. A. Matsuyama, K. Maeda and H. Murai, *J. Phys. Chem. A*, 1999, **103**, 4137.

Acknowledgements

The present study was undertaken at Osaka City University during 2016–2020. This work was carried out under the supervision of Professor Dr. Yoshio Teki. He gave me a chance to study this interesting research topic in his laboratory providing a favourable research environment, valuable instructions, helpful discussions, and suggestions during the course of this work. I would like to express my deep gratitude to Professor Dr. Yoshio Teki for his unfailing guidance and encouragement throughout the course of this work and for his kind advice in preparing this thesis.

I would also like to express my deep gratitude to Professor Dr. Harukazu Yoshino and Dr. Masazumi Fujiwara for their helpful suggestions and discussions. I would like to thank Professor Dr. Eiji Shikoh. He kindly gave me suggestions and discussions when I prepared the VVD films. I would like to thank Dr. Rika Tanaka (the Analytical Centre of Osaka City University) for her X-ray crystallographic analyses and Mr. Toshio Matsuyama (technical staff for system measurements) for making the electro-circuits. I would like to thank Mr. Shogo Hagi and Ms. Masumi Hinoshita for their collaboration in the work on the weak CT complex. In addition, this study and my daily life were supported by all members of the quantum functionality materials laboratory at Osaka City University. Financial support from the JSPS fellowship DC2 is gratefully acknowledged. I would like to thank JSPS for the KAKENHI Grant (Number 20J15238) for a JSPS Research Fellowship.

Finally, I would like to express my heartfelt gratitude to my family for supporting me mentally and financially.

List of Publications

1. Photoconductivity and Magnetoconductance Effect on Vacuum Vapor Deposition Films of Weak Charge-Transfer Complexes
   Ken Kato, Shogo Hagi, Masumi Hinoshita, Eiji Shikoh, Yoshio Teki,
   Physical Chemistry Chemical Physics, **2017**, 19(29), 18845−18853.
   Selected as **Inside Back Cover**

2. Low-Magnetic Field Effect of Photocurrent and EDMR Study on Vacuum Vapor Deposition Films of of Pyrene/Dimethylpyromellitdiimide (Py/DMPI) Weak Charge-Transfer Complexes
   Shogo Hagi, **Ken Kato**, Masumi Hinoshita, Harukazu Yoshino, Eiji Shikoh, Yoshio Teki,
   Journal of Chemical Physics, **2019**, 151, 244704/1−11.

3. Photogenerated Carrier Dynamics of TIPS-Pentacene Film as Studied by Photocurrent and Electrically Detected Magnetic Resonance
   Ken Kato, Yoshio Teki,
   Physical Chemistry Chemical Physics, **2020**, accepted.
   DOI : 10.1039/D0CP05125J